Understanding Microstructure Evolution in Nanoparticle-Reinforced Metal Alloys and Integrated Heat and Mass Transfer for Thermochemical Energy Storage

by

Bryan Kinzer

A dissertation submitted in partial fulfillment
of the requirements for the degree of
Doctor of Philosophy
(Mechanical Engineering)
in the University of Michigan
2024

Doctoral Committee:

Professor Rohini Bala Chandran, Chair
Professor Solomon Adera
Professor Jerard Gordon
Professor Donald Siegel

Bryan Kinzer
brkinzer@umich.edu
ORCID iD: 0000-0003-3780-4910

© Bryan Kinzer 2024

DEDICATION

I dedicate this thesis first to my newborn son, Silas, and my future children. I hope my research career can help leave a cleaner future for you. To my wife, Jill, for your support and love throughout both this PhD and in the years to come.

ACKNOWLEDGEMENTS

First, I would thank my PhD advisor and chair Professor Rohini Bala Chandran. When I joined your lab I was coming off some health issues and navigating the start of the pandemic, so I am ever grateful for you taking me on during such a turbulent time. I have been very grateful to have a mentor who is knowledgeable and willing to explore in so many different areas, which I believe was crucial to being able to navigate two very different research projects. Your mentorship has helped me grow as an independent researcher. As your second full time student to graduate I look forward to continue to see the TREE lab blossom.

I also want to thank my committee members, Professors Solomon Adera, Jerard Gordon, and Don Siegel. I appreciate the time and effort you all have spent to serve on my committee. Your feedback both about the thesis and general support on navigating the PhD journey is appreciated. I would also like to thank Dr. Andre Benard, Dr. Haseung Chung, Dr. Himanshu Sahasrabudhe, Dr. David Montiel, and Dr. Aaron O'Neil for your insightful conversations and collaborations for the additive manufacturing projects. I would also like to thank Dr. Michael Craig, Dr. An Pham, and Dr. Steven Kiyabu for their assistance and collaborations on the salt hydrate projects. I am also grateful for Mark Smith for serving as my mentor during my geothermal internship helping me conduct startup research. I would like to thank all the members of the TREE Lab both past and present. In particular for Durga, Luisa, Bingjia, Zijie, Mike, Rachel, Rebecca, and Brandon I am grateful to have had you all as lab and desk mates. I am grateful for the helpful culture we have where we give each other feedback when prepping for conferences or qualifying exams. You have made coming into work a more enjoyable experience. You all are doing great research, so keep it up.

I would like to thank and acknowledge all my funding sources, which includes a grant by the Advanced Research Projects Agency-Energy (ARPA-E), U.S. Department of Energy, under Award Number DE-AR0001123 under co-operative agreement with Michigan State University and the University of Michigan. I thank startup funding from the College of Engineering and the Department of Mechanical Engineering at the University of Michigan. I thank Department of Mechanical Engineering funding in the form of graduate student instructor positions. I also acknowledge funding provided by the Graham Sustainability

Institute's Carbon Neutrality Acceleration Program (CNAP) at the University of Michigan. I also thank the funding from the Energy Materials Network under award number DE-EE0002792-1530.

I want to finish by acknowledging all the personal relationships that have played a key role in this PhD adventure. For the original Michigan football crew, you all were my original friend group from 2018 that made Michigan not just where I was doing my PhD but my home. It has been amazing to see everyone mature with many engagements, marriages, and defenses to celebrate. In particular, I would like to thank Khoi for serving as a groomsman in my wedding and for all the adventures we have gone on (I should never have agreed to make 1000 paper cranes though). I also want to thank Ryan for all the backpacking trips we went on that provided a much needed break from technology. I also want to thank all my St. Mary's friends, in particular Andrew, for the somewhat fun boondoggles and on a more serious note for helping me grow in my faith. For my blood family, I am particularly grateful to have been able to keep a beehive with my Michigan grandparents. I am thankful for my brothers, Michael and Daniel, for always pushing me to put forth my best effort. I want to acknowledge my parents, Tom and Stacey, for all the lessons you taught me growing up and encouraging me to take risks and explore new areas. The stability and love you provided have allowed me to become the man I am today. I also want to thank the Coghlan family for welcoming in with open arms. For Kathy and Kevin for supporting me like a son, and for Kevin, Lissie, and Katelyn for welcoming me into the chaos of family vacations. For Mark and Sue for serving as my adoptive Uncle and Aunt here in the Midwest. Now, for my wife, Jill, the love of my life. We met at graduate school orientation, so our story really does line up with our time at Michigan. You have been a constant rock supporting me as a I switched labs, and encouraging me to do triathlons and marathons. You have made life that much more enjoyable. We tied the knot in Michigan and began our family here, so Michigan will always have a special place in our hearts no matter where we end up. There are many more people both from my time in Michigan and before that I am grateful for, so even if you do not see your name listed here know you are appreciated.

TABLE OF CONTENTS

DEDICATION ii

ACKNOWLEDGEMENTS iii

LIST OF FIGURES viii

LIST OF TABLES xiii

LIST OF APPENDICES xiv

LIST OF ACRONYMS xv

ABSTRACT xvi

CHAPTER

1 Introduction 1

1.1 Motivation of Thesis 1
1.2 Microstructure Evolution in Nanoparticle-Reinforced Metal Alloys 2
1.2.1 Overview of Additively Manufactured Nanocomposites for Power Generation 2
1.2.2 Knowledge Gaps & Research Objectives 4
1.3 Integrated Heat and Mass Transfer for Thermochemical Energy Storage . . 7
1.3.1 Overview of Salt Hydrate Operation and Principles 7
1.3.2 Knowledge Gaps & Research Objectives 10
1.4 Thesis Outline & Research Contributions 13

2 A Phase-Field Study on the Effects of Nucleation Rate and Nanoparticle Distributions on Solidification and Grain Growth 15

2.1 Introduction 15
2.2 Methods 17
2.2.1 Modeling Domain 18
2.2.2 Nanoparticle Distributions in the Metal Matrix 19
2.2.3 Governing Equations for Phase-field Model 20
2.2.4 Grain Nucleation and Remapping 22
2.2.5 Model Parameters 23
2.2.6 Simulation Procedure 24

2.3 Results and Discussion . . . 26
2.3.1 Impact of Clustering and Nucleation Rate on Solidification . . . 26
2.3.2 Nucleation Rate and Clustering Influence Grain Size . . . 28
2.3.3 Smith-Zener Grain Size Depends on Nucleation Rate . . . 29
2.4 Grain Size Saturation is Explained by Particle Pinning Fraction . . . 32
2.4.1 Interpreting Experimental Data with Model Predictions . . . 33
2.4.2 Scope and Future Extension of Model . . . 35
2.5 Conclusion . . . 35

3 Process Mapping for Kanthal A1 and Kanthal KAPM FeCrAl Alloys using Synchrotron Imaging . . . 37

3.1 Introduction . . . 37
3.2 Material and Methods . . . 39
3.3 Results and Discussion . . . 41
3.4 Conclusion . . . 45

4 Modeling and Experimental Demonstrations Reveal Ragone Framework for Salt Hydrate Thermochemical Energy Storage . . . 47

4.1 Introduction . . . 47
4.2 Methods . . . 50
4.2.1 Theoretical/Computational modeling approach . . . 51
4.2.2 Ragone plots . . . 56
4.2.3 Parasitic power for pumping and humidification . . . 58
4.2.4 Experimental . . . 58
4.2.5 packed bed reactor: Experiment and model comparisons . . . 60
4.3 Results and Discussion . . . 61
4.3.1 Model predictions for reactor-scale thermochemical performance . . . 61
4.3.2 Specific power and energy relationships with the Damkohler number 63
4.3.3 Parasitic loads can be substantial . . . 66
4.3.4 Insights from comparative assessment of reactor-scale measurements and model predictions . . . 68
4.3.5 Benchmarking thermochemical performance of salt hydrates using Ragone framework . . . 73
4.3.6 Perspectives and Outlook . . . 75
4.4 Conclusions . . . 76

5 Spatial Distributions of Hydration Cycling in Salt Hydrates using Neutron Imaging . . . 78

5.1 Introduction . . . 78
5.2 Methods Overview . . . 80
5.3 Results and Discussion . . . 81
5.3.1 Operando diffusion chamber hydration . . . 81
5.3.2 In Situ Through Flow Reactor . . . 83
5.4 Conclusions . . . 85

6 Conclusion . . . 86

6.1 Thesis Summary 86
6.1.1 Microstructure of Nanoparticle-Reinforced Metal Alloys 86
6.1.2 Integrated Heat and Mass Transfer for Thermochemical Energy Storage 87
6.2 Thesis Impact and Contributions 89
6.3 Limitations and Future Work 90
6.3.1 Microstructure of Nanoparticle-Reinforced Metal Alloys 90
6.3.2 Integrated Heat and Mass Transfer for Thermochemical Energy Storage 91

APPENDICES 95

BIBLIOGRAPHY 119

LIST OF FIGURES

FIGURE

1.1 (a) Schematic of laser powder bed fusion, (b) Strength drop-off versus temperature for a representative alloy (Haynes 214) [1] 2

1.2 Microstructures of solidified alloys. (a) particle free, (b) nanoparticle reinforced, and (c) Smith-Zener pinning of a grain boundary by a nanoparticle. Scale is 1 micron. 4

1.3 Processing map of laser power vs speed with Melt pool and vapor depression morphology regimes. 5

1.4 Space heating operation of salt hydrate reactor. Stage 1 is reactor charging (dehydration) and stage 2 is discharging (hydration). Insets show different form factors of salt hydrates, pure ($MgSO_4$) and composite ($SrBr_2$). 9

1.5 A model Clausius Clapeyron Diagram for a typical salt. Arrows represent direction temperature and/or water vapor pressure must go to drive the reaction. . . 10

2.1 Computational domain. (a) Schematic of the computational domain with a mesh size of 39 nm $\times$ 39 nm (not to scale) and with a sample clustered distribution of monodisperse nanoparticles with radius of $r_p = 25$ nm. (b) Aggregations of individual nanoparticles form clusters based on size distribution data with the cluster zone denoted by the dotted red circle with radius, r_c. The shaded region bounded by the dotted black curves within 1 r_p of each nanoparticle and within 2 r_p of the substrate wall represents heterogeneous nucleation zones. 18

2.2 Time evolution of grain microstructure for random and clustered distributions of nanoparticles with an area fraction of $\Phi_{np} = 0.05$ and for the case of no nanoparticles for nucleation site densities of (a–d) $0.1N_0$ and (e–h) $10N_0$. Stars in (a) and (e) represent the instance when solidification is complete. Snapshots of microstructures for the clustered distribution of nanoparticles at the (b,f) start of simulation, (c,g) peak number of grains, and the (d,h) final microstructure. Substrate is present at the bottom of the 2D domain and not shown in the figure. $N_0 = 1$ corresponds to 1.95×10^9 Nuclei/m^2. Scale bars are 1 μm. 27

2.3 Final grain microstructures after 2000 μs for select cases of 0.01 area fraction for random distributions with (a) $0.1N_0$, (d) $10N_0$; for clustered distributions with (b) $0.1N_0$, (e) $10N_0$. Reference cases shown with $10N_0$ for (c) particle free case and (f) with single large cluster of nanoparticles with 0.01 area fraction. Substrate is present at the bottom of the 2D domain and not shown in the figure. $N_0 = 1$ corresponds to 1.95×10^9 Nuclei/m^2. Scale bars are 1 μm. 28

2.4 Steady-state average grain size for random and clustered distributions as a function of nucleation site density, N_0, for various area fractions, Φ_{np}. Points shown are averages of 3 simulations per nucleation site density modeled and the error bars represent standard deviation. $N_0 = 1$ corresponds to 1.95×10^9 Nuclei/m^2. 30
2.5 Modified Smith-Zener Diameters for random and clustered distributions. (a) Grain diameter versus area fraction for nucleation site densities of $10^{-3}N_0$ and 10^3N_0. All other N_0 will fit between these two extremes. Reference fits are from the original Smith-Zener Equation as recorded by Smith [2] and Srolovitz et al. [3]. (b,c) Impact of nucleation site density along with error bars across three trials on m and K, which are fitting constants in the Smith-Zener Equation (Eq. 2.13). $N_0 = 1$ corresponds to 1.95×10^9 Nuclei/m^2. 31
2.6 (a) Impact of nucleation site density, N_0, on fraction of particles pinning grain boundaries, Γ_{tot}, for select area fractions of 0.01, 0.05, 0.10. (b–c) Impact of pinning fraction, separated by on grain boundary, Γ_2, and at triple point fractions, Γ_3, on final grain diameter with best fit curves for the three trial average for all area fractions. (b) All random cases: $d_{\mathrm{z}} = 2 \times 2.11 r_{\mathrm{p}}/(\Gamma_2^{1.534}), R^2 = 0.868$ and $d_{\mathrm{z}} = 2 \times 3.97 r_{\mathrm{p}}/(\Gamma_3^{0.477}), R^2 = 0.943$. (c) all clustered cases: $d_{\mathrm{z}} = 2 \times 2.84 r_{\mathrm{p}}/(\Gamma_2^{1.58}), R^2 = 0.721$ and $d_{\mathrm{z}} = 2 \times 4.07 r_{\mathrm{p}}/(\Gamma_3^{0.568}), R^2 = 0.820$. $N_0 = 1$ corresponds to 1.95×10^9 Nuclei/m^2. 33
2.7 (a) Predicted vs Experimental Grain Sizes reported in the literature for select nanoparticle reinforced alloys. Nucleation rate dependent grain size predictions come from the random distribution case of Table 2.2. (b) Table showing additional pertinent alloy information (Note: reference numbers are from paper, see thesis text for thesis reference numbers). $N_0 = 1$ corresponds to 1.95×10^9 Nuclei/m^2. 34

3.1 Experimental Setup of the *In-situ* Synchrotron Dynamic X-ray Radiography Setup 39
3.2 Laser Power vs Laser Speed Processing Map for Kanthal A1 overlaid with Rosenthal Model. The images bordered in red had observable keyhole porosity. The circled green case at 300 W and 800 mm/s was identified as the optimal condition. The dotted background colors represent melt pool regimes. 42
3.3 Laser Power vs Laser Speed Processing Map for Kanthal APM overlaid with Rosenthal Model. The images bordered in red had observable keyhole porosity. The circled green case at 300 W and 800 mm/s was identified as the optimal condition. The dotted background colors represent melt pool regimes. 44
3.4 Vapor Depression Depth versus Laser Velocity for different laser powers. Comparison of Kanthal A1 and Kanthal APM. 45

4.1 (a) Computational continuum modeling domain for hydration reaction and (b) schematic of the experimental flow loop in a packed bed reactor with salts undergoing thermochemical hydration and dehydration reactions for energy storage. 52

4.2 Model predictions for a packed bed of K_2CO_3 particles with (a-d) mass transport limited, kinetic pre-factor of $K^* = 2.0$, and (e-h) kinetically limited with $K^* = 0.5$ conditions. Profiles are shown at 30, 60, 90, and 120 minutes for (a,e) temperature, (b,f) water vapor concentration, (c,g) fractional hydration rate, and (d,h) fractional hydration extent. Baseline model parameters are modeled with $\varepsilon = 0.6$, $RH_{\text{in}} = 45\%$, $\vec{u} = 0.5$ m/s, $L = 0.125$ m, $T_{\text{in}} = 20°\text{C}$. Equilibrium at Max T line indicates equilibrium vapor concentration corresponding to the maximum temperature predicted. 62
4.3 Ragone plots based on model predictions for packed bed reactor hydration with $\varepsilon = 0.6$, $RH_{\text{in}} = 45\%$, $L = 0.125$ m, $T_{\text{in}} = 20°\text{C}$, $K^* = 1$ with velocities: $\vec{u} = 0.013 - 2\text{m/s}$ for (a) K_2CO_3 and (b) $SrBr_2$ composite ($\Delta H_{\text{rx}} = 3.35$ MJ/kg$_{\text{H2O}}$). Discharge is from left to right and shaded lines indicate 25% and 98% depth of discharge (DoD). (c) Average specific power at 25% and 98% depth of discharge vs Damkohler number, Da, for both salts. Shaded region shows mass transport to kinetic transition between $2 \leq Da \leq 0.5$. Fit shown is for data points when Da > 2. 64
4.4 Influence of inlet air velocity on parasitic pumping power requirements, sP_{pump}, with (a) K_2CO_3 and (b) $SrBr_2$ composite at 500 μm and 3 mm particle sizes, where sP_{chem} is the model predicted average thermochemical power from hydration reactions at 98% depth of discharge for varying velocities and the same as $\overline{sP}_{\text{chem, model}}$ (Eq. 4.10), and sP_{net} is the net specific power which discounts pumping power, sP_{pump}, from the thermochemical power produced, sP_{chem}.(c) Impact of moisture supply fraction, ξ_{humid}, on the net specific power, sP_{chem}, which discounts the humidification power load, sP_{humid} (Eq. 4.15), from the thermochemical power produced, sP_{chem} for varying velocities for both salts. Model cases are for $\varepsilon = 0.6$, $RH_{\text{in}} = 45\%$, $L = 0.125$ m, $T_{\text{in}} = 20°\text{C}$, $K^* = 1$, and $\Delta H_{\text{rx,SrBr2}} = 3.35$ MJ/kg$_{\text{H2O}}$ with air inlet velocities: $\vec{u} = 0.013 - 2\text{m/s}$. . . 66
4.5 Spatial and temporal variation of air temperature in the experimental packed bed reactor with $SrBr_2$ composite with the inlet air at 22°C and a fixed relative humidity of 45% RH_{in} for air flow rates of (a) 2 LPM, (b) 4 LPM, (c) 6 LPM. Inset shows thermocouple T1, T2 and T3 locations inside reactor. Shaded color regions are standard deviations obtained from 3 independent experimental trials. 68
4.6 Comparison of $SrBr_2$ composite experimental reactor (labeled as exp) with model predictions at different flow rates and as a function of kinetic pre-factor, K^* values modeled for the (a-c) outlet temperature and (d-f) outlet water vapor concentration. Shaded color regions are standard deviations across 3 trials. Model assumes $\varepsilon = 0.5$, $RH_{\text{in}} = 45\%$, $L = 0.125$ m, $T_{\text{in}} = 22°\text{C}$, $\rho_{\text{s}} = 620$ kg/m^3. $\Delta H_{\text{rx}} = 1.95$, 2.42, 3.35 MJ/kg$_{\text{H2O}}$ for 2, 4, and 6 LPM cases respectively. 69
4.7 Experimental and model predictions for the Ragone plot at 2, 4, and 6 LPM for the packed bed reactor with $SrBr_2$ composite. Shaded region represents bounds of model results for kinetic pre-factors of $K^* = 1$ and $K^* = 0.05$. Error bars represent experimental uncertainty in specific power and specific energy at select points. Model assumes $\varepsilon = 0.5$, $RH_{\text{in}} = 45\%$, $L = 0.125$ m, $T_{\text{in}} = 22°\text{C}$, $\rho_{\text{s}} = 620$ kg/m^3. $\Delta H_{\text{rx}} = 1.95$, 2.42, 3.35 MJ/kg$_{\text{H2O}}$ for 2, 4, and 6 LPM cases respectively. 72

4.8 Ragone plot comparison of different energy storage devices. $SrBr_2$ composite material-scale is generated from this study and K_2CO_3 material-scale data is sourced from Geaini et al. [4]. 2, 4, and 6 LPM curves are from experiments from this study for $SrBr_2$ composite reactor. The 38.5 LPM (projected) case represents the maximum power output for the $SrBr_2$ composite reactor based on the best fit kinetic pre-factor of $K^* = 0.1$. Li-ion cell reference data is for a voltage cut-off of 3.5 V (triangles), and phase change reference is for n-tetradecane/graphite composite slab with cut-off temperature of 12°C (circles) [5]. Shaded region represents load shifting between 4 and 8 hours. 73

5.1 Neutron imaging setup for (a) diffusion chambers, (b) through flow reactors, and (c) simplified flow loop setup. Neutron imaging area is 86 x 86 mm represented by the dotted red box. 81
5.2 Normalized hydration profiles for both pure (a-d) and composite (e-h) $SrBr_2$ diffusion chambers at different time stamps. Scale bars are 5 mm. 82
5.3 (a) Comparison of hydration depth versus time for pure versus composite $SrBr_2$ during first hydration and tracking of cycling on hydration fraction for (b) 6 mm and (c) 20 mm deep chambers. 82
5.4 Normalized hydration profiles for flow rates of 1.5 LPM (a-d) and 0.5 LPM (e-h) for $SrBr_2$ through flow reactors at different time stamps. Scale bars are 5 mm. . 84

A.1 Cluster size radius distributions used in generating clustered cases. Each cluster is made up of individual 25 nm radius particles. Data is from selective laser melting of nano-Tic reinforced Inconel 718 [6] 95
A.2 Nucleation Probability, P_0, versus Temperature at N_0. T_m is the melting point of Stainless Steel 316L from M. Yang et. al. [7]. $N_0 = 1$ corresponds to 1.95×10^9 nuclei/m^2. Probability calculated for contact angle of $\theta = 4°C$. 96
A.3 Comparison of final grain size distribution to reference case of random with area fraction, $\Phi_{np} = 0.01$, and nucleation site density, $10N_0$. Impact of (a) area fraction: random, $\Phi_{np} = 0.10$ and $10N_0$, (b) nucleation rate: random, $\Phi_{np} = 0.01$ and $0.1N_0$, (c) clustering: clustered, $\Phi_{np} = 0.01$ and $10N_0$. Dotted vertical lines indicate the average grain size for each case with shaded regions indicating standard deviation. $N_0 = 1$ corresponds to 1.95×10^9 nuclei/m^2. 97
A.4 Final Grain Microstructure of 3D Domain after 20,000 μs for random, $\Phi_{np} = 0.017$ and a site density of 5×10^{14} nuclei/m^3. 98

B.1 Measured water uptake for $SrBr_2$ composite weigh boat material-scale experiments (1 g initial) at (a) 45% RH and (b) 30% RH. 100
B.2 Neutron computed tomography scans of dehydrated $SrBr_2$ composite. (a-c) 2D slices of scans. (d) 3D rendering. 101
B.3 Ragone plot with corresponding Da comparisons to Main Text $SrBr_2$ composite model variable velocity ($\vec{u}$) study. (a) variable reactor length, $L = 1.2, 0.6, 0.4, 0.125, 0.0625, 0.03125$ m, (b) variable inlet relative humidity, $RH_{in} =$ 60%, 52.5%, 45%, 37.5%, 30%, 22.5%, 15%. Baseline values are $\varepsilon = 0.6$, $RH_{in} = 45\%$, $\vec{u} = 0.125$ m/s, $L = 0.125$ m, $T_{in} = 20$ °C, $K^* = 1.0$. 102

B.4 Comparison of outlet temperature versus time for model results at equivalent Damkohler number ($Da = 0.38$) with $\vec{u} = 2$ m/s for K_2CO_3 and $\vec{u} = 0.5$ m/s for $SrBr_2$ composite. Cases are for $\varepsilon = 0.6$, 45% RH, $K^* = 1.0$, $L = 0.125$ m, $T_{\text{in}} = 20°C$, and $\Delta H_{\text{rx,SrBr2}} = 3.35$ MJ/kg_{H2O}. 102
B.5 $SrBr_2$ composite vs vermiculite experimental temperature profiles at 2, 4, and 6 LPM at different thermocouple probe locations. 103
B.6 Comparison of water uptake for $SrBr_2$ composite and vermiculite reactors. (a) water uptake at different flow rates, (b) zoomed in view of water uptake at different flow rates, (c) reaction extent with respect to time at 2, 4, and 6 LPM. 103
B.7 $SrBr_2$ composite experimental reactor without insulation with locations of different thermocouple probes labeled. 104
B.8 Heated inlet test heat loss test of insulated dehydrated $SrBr_2$ composite reactor at flow rates of 2, 4, and 6 LPM. (a) inlet and outlet temperature, and (b) the calculated temperature drop from the 35°C inlet. 104

C.1 Images of experimental setup of salt hydrate imaging at Multimodal Advanced Radiography Station (MARS) — CG-1D — HFIR. (a) Diffusion chambers and (b) Through flow reactors. 114
C.2 Through flow $SrBr_2$ composite reactor results. (a) Hydration Fraction vs time and (b) Reaction rate versus time. 114
C.3 Relative humidity versus time for both top (1.5 LPM) and bottom (0.5 LPM) through flow reactors. 115
C.4 Spatial distribution of hydration fraction and rate for reactors. (a) and (c) for 0.5 LPM and (b) and (d) for 1.5 LPM. 115

LIST OF TABLES

TABLE

2.1 Model parameters, their baseline values and ranges explored in the phase-field simulations with relevant references 25

2.2 Nucleation rate dependent grain size predictions for random and clustered distributions fitted for nucleation site densities ($10^{-3}N_0 - 10^3N_0$) and area fractions ($\Phi_{np} = 0.01$–0.10). $N_0 = 1$ corresponds to 1.95×10^9 Nuclei/m^2. 32

3.1 Properties used for both the Kanthal A1 and Kanthal APM Rosenthal Model . 41

4.1 Material properties, kinetic parameters, and packed bed reactor design and morphology categorized based on the materials — K_2CO_3 and $SrBr_2$ composite considered for baseline model predictions and experimental conditions 51

A.1 Grain Size and Pinning Fraction results for 3D simulations of random and $\Phi_{np} = 0.01$ with $r_p = 25$ nm in a 2.5 μm $\times$ 2.5 μm $\times$ 0.3125 μm thin film domain. . 96

B.1 Dry air and water vapor properties used for both model and experimental reactor analysis [8, 9] 105

B.2 Maximum uncertainty for $SrBr_2$ composite experimental reactor parameters . . 111

B.3 Heat loss estimates at different flow rates from heated $T_{in,da} = 35°C$ inlet $SrBr_2$ composite experiments 112

LIST OF APPENDICES

A Appendix for Chapter 2: A Phase-Field Study on the Effects of Nucleation Rate and Nanoparticle Distributions on Solidification and Grain Growth 95

B Appendix for Chapter 4: Modeling and Experimental Demonstrations Reveal Ragone Framework for Salt Hydrate Thermochemical Energy Storage 100

C Appendix for Chapter 5: Spatial Distributions of Hydration Cycling in Salt Hydrates using Neutron Imaging 113

LIST OF ACRONYMS

AM Additive Manufacturing

ODS Oxide Dispersion Strengthened

DXR Dynamic X-ray Radiography

TES Thermal Energy Storage

ABSTRACT

This doctoral dissertation focuses on two independent research topics to understand: (i) microstructure evolution of nanoparticle-reinforced, additively manufactured, metal alloys to enable high strength at elevated temperatures and (ii) combined heat and mass transfer effects, at both small and large length scales, to enable low-cost thermal energy storage using salt hydrates for building heating/cooling applications.

Nanoparticles added to metal alloys can enhance its mechanical strength, enabling new materials for next generation, high-temperature (> 700 °C) and high-efficiency power plants. A parametric, phase-field study was performed to quantify how nucleation rate, in addition to nanoparticle size and concentration, affects grain size and therefore alloy strength. Rapid solidification rates consistent with additive manufacturing processes were modeled. Improving upon the classical Smith-Zener equation, grain size is predicted to be inversely proportional to nucleation rate, with a power exponent of 0.15. 2D results reveal a strong preference of nanoparticles to pin at the intersection of three grains. This pinning fraction is so dominant it largely determines grain size across the wide range of particle area fractions (0.01-0.1) and 7 orders-of-magnitude of nucleation rates modeled. Additionally, in-situ X-ray radiography laser powder fusion experiments were performed for two commercial FeCrAl alloys with (Kanthal APM) and without (Kanthal A1) nanoparticles. Based on melt pools, the nanoparticles had a minimal impact on the processability window.

Simple salts offer the potential to store thermal energy (150-750 Wh/kg) through reversible uptake (hydration) and release (dehydration) of water vapor accompanied with energy release and uptake. This energy density can be 10-fold larger than phase change materials and competitive with lithium-ion batteries, with up to 5-fold cheaper projected costs. Multiphysics models were developed to predict the combined effects of heat and mass transfer and reaction kinetics, to quantify tradeoffs between accessible energy capacity and power density and interpret experimental data. Reactor-scale experiments for thermal discharge during hydration were performed in a packed bed reactor with 100 grams of composite particles with strontium bromide ($SrBr_2$) impregnated in a porous vermiculite host. While power density nearly proportionally increases with air flow rate from 2 to 4 LPM at 6 LPM performance is more dominantly affected by kinetics with a maximum power density of 11

W/kg. A modified Damkohler number based on salt and reactor properties was developed to help speed up design by predicting this transition from mass transport to kinetics limited regimes. Model comparison reveals effective reaction kinetics slow down by nearly an order-of-magnitude from material to reactor scale. To meet daily building load shifting demands (35-100 W/kg), the combined results reveal improved salt hydrates and reactor designs are needed to increase the fraction of accessible stored thermochemical energy. Additionally, direct visualization of water uptake/release was performed using spatially resolved (42 microns) neutron imaging for pure and composite $SrBr_2$ providing a unique, 10-100 times spatial improvement compared to the state-of-the-art (2-15 mm). Results reveal reduction in particle swelling during hydration for the composite versus pure salt; the composite enhances mass transport by opening water vapor diffusion pathways. Consistent with model predictions, reactor scale neutron imaging shows direct evidence of the transition from mass transport to kinetics limited hydration profiles with increasing flow rate.

Overall, this thesis provides a deeper understanding of the mechanisms that enable and limit the use of nanoparticle-reinforced alloys as well as thermochemical salt hydrate reactors for energy storage.

CHAPTER 1

Introduction

1.1 Motivation of Thesis

Driven by the increasingly urgent need to reduce global warming as emissions have continued to rise, new net-zero-carbon technologies are needed to enable a more sustainable society [10, 11]. Two major pursuits toward this goal are to: (1) increase energy efficiency of power plants and (2) improve energy storage for building thermal loads. The large majority, $\sim 70\%$, of electricity generation still originates from steam power cycle generation, which are currently largely fueled by fossil fuels including coal and natural gas [12]. Thus, it is crucial to improve the efficiency of existing plants to reduce emissions and to enable next generation carbon free power, such as advanced nuclear or concentrated solar power plants as coal plants are retired [10, 13]. Since the efficiency of a powerplant is dictated by both the heat source and the sink temperatures, increasing the maximum operating temperatures from the current 550°C for steam power plant to ≥ 700°C using a sCO_2 Brayton cycle can push efficiencies from 40% to over 50% [13]. However, conventional steels and alloys lack strength and corrode at these elevated temperatures [14, 15, 16]. Therefore, the first aim of my research is to use a combination of modeling and experiments to enable alloys for these high temperature applications. The second aim of my research is motivated by the over 10% of global CO_2 emissions stemming from building heating and cooling energy demands [11]. As more intermittent renewables, such as solar and wind, are added to the grid, there is a rapidly growing need to store these thermal loads [17, 18]. Although home lithium-ion (Li-ion) battery systems, which can convert stored electricity into heat, are becoming more popular, their high raw material costs slow their adoption. That is why the second aim of my research focuses on investigation of thermal energy storage alternatives, which project to deliver power at a fraction ($\$75 - \$15$ vs $\$350 - \$100$ per kWh) of the cost of Li-ion battery systems [17].

While the two aims of my thesis, which focus on alloy development for power plants and

salt hydrate thermochemical energy storage for building heating are motivated by a desire to contribute to a greener energy future and even have some overlap in approaches and methodologies, such as *operando/in-situ* imaging and materials characterization, these two aims are very different. It is better to think of the two projects to be distinct efforts, which are only very loosely tied together in the Introduction and Conclusion chapters of this thesis.

1.2 Microstructure Evolution in Nanoparticle-Reinforced Metal Alloys

1.2.1 Overview of Additively Manufactured Nanocomposites for Power Generation

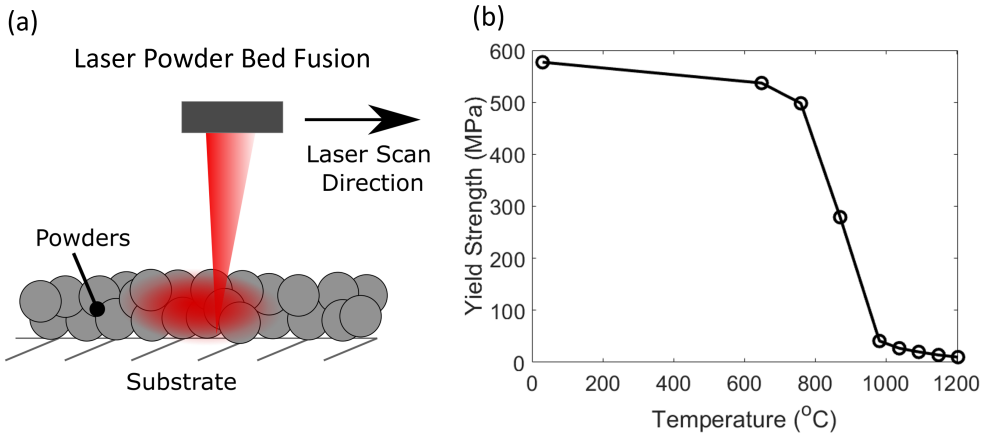


Figure 1.1: (a) Schematic of laser powder bed fusion, (b) Strength drop-off versus temperature for a representative alloy (Haynes 214) [1]

Additive manufacturing (AM) enables creation of complex geometries, such as heat exchangers with fins to increase heat transfer or structural components for automobiles, for both prototyping and final production [19, 20, 21]. Since additive manufacturing produces near net shape parts, this speeds up prototyping since time consuming machining steps can be avoided as compared to conventional subtractive manufacturing [20]. In selective laser melting (a form of laser powder bed fusion), a thin layer of metallic powder is spread onto a build area (Fig. 1.1a) [20]. Then, based on a computer-aided design file, the laser selectively melts the powders fusing them together. The part is then lowered, and another layer of powder is spread. The laser melts this new layer of particles bonding the layers together slowly building the part up layer by layer. With AM processes, rapid solidification rates

of $10^5 - 10^6$ K/s and temperature gradients of $10^5 - 10^7$ K/m are typically observed [22]. Laser powers range from $50 - 500$ W and laser speeds from $50 - 2000$ mm/s depending on laser spot size and machine capabilities [23]. These ranges depend on properties such as alloy thermal conductivity, melting point, wave-length dependent laser absorptivity, hatch spacing (distance between scans), and layer thickness (how much the powder bed is raised for each layer) all of which can vary widely [20, 23].

There is interest in investigating selective laser melting of oxide dispersion strengthened (ODS) alloys, where small concentrations (typically 0.2-5 wt%) of either microparticles ($1 - 10$ μm) or nanoparticles ($10 - 100$ nm), such as TiB_2, Y_2O_3, or ZrO_2 are added to the base alloy to improve its mechanical properties with nanoparticles having a larger impact [15, 24, 25, 26, 27]. ODS alloys can double yield strength from room to elevated (≥ 800°C) temperatures as well have been shown to more than quadruple creep strength at temperatures up to 1000°C [25, 28, 29, 30]. The ODS particles also support the formation of stable oxide passivation layers, which improve corrosion resistance at elevated temperatures [31]. Commercial ODS alloys, produced through conventional powder metallurgy processes, include Ni alloys, such as MA6000 [32], and Fe alloys, such as Kanthal APM and MA956 [31, 24]. There are also a growing number of additively manufactured ODS alloys including GRX-810, a NiCoCr + Y2O3 alloy [28], a TiC reinforced Inconcel 718 Ni alloy [6], and a TiC reinforced Al alloy [33]. Still challenges remain in developing AM versions of ODS alloys. The rapid solidification rates in AM processes can cause the formation of long, columnar grains leading to undesired anisotropic material properties (Fig. 1.2a) [34, 35]. In the right distributions and concentrations nanoparticles can result in a more refined, equiaxed grain structure (Fig. 1.2b) [35]. Nanoparticles can also agglomerate during solidification, which can limit their effectiveness [6, 36]. This is due to compounding effects from van der Waals forces, which result in weak inter-particle attraction forces, and Marangoni flow, where gradients in surface tension driven by the high temperature gradients cause an additional nanoparticle agglomeration driving force [6, 37, 38].

For many alloys, strength and creep properties drop off considerably at elevated temperatures (Fig. 1.1b) (above their homologous temperature ($T_{\text{alloy}} \geq T_{\text{melt}}/2$)) where dislocations become more thermally activated and grain boundary sliding can occur [24, 26]. ODS particles improve high temperature properties first by serving as nucleation sites to reduce grain size [39, 40]. Since grain boundaries serve as barriers to dislocations, as grain size decreases the increased grain boundary density results in a higher number of obstacles to overcome to deform the alloy. This improves alloy strength, which can be predicted by the Hall-Petch relationship, $\sigma_{\text{H-P}} = K\sqrt{D}$, where K is the material specific Hall-Petch constant and D is grain diameter (below grain sizes of about 100 nm this relationship falls apart) [26, 41]. At

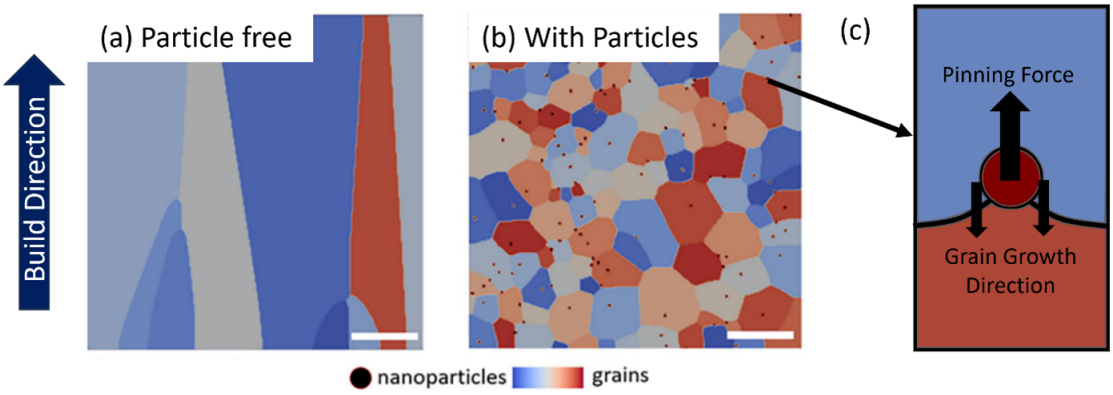


Figure 1.2: Microstructures of solidified alloys. (a) particle free, (b) nanoparticle reinforced, and (c) Smith-Zener pinning of a grain boundary by a nanoparticle. Scale is 1 micron.

these elevated temperatures grain coarsening occurs, with the increasing grain size slowly reducing alloy strength over the lifetime of the part [7, 39]. As grains grow they come in contact with ODS particles. Due to differences in inter-facial energy between the ODS particles and the grain boundary there is an energy penalty for grain boundaries to detach from nanoparticles in what is known as Smith-Zener pinning (Fig. 1.2c) [2, 42]. This pinning force either dramatically slows down or prevents further grain coarsening, even at elevated temperature, so Hall-Petch strengthening is maintained for longer [34]. ODS nanoparticles also directly contribute to improved strength through Orowan bowing, where the nanoparticles themselves serve as obstacles that impede dislocations [24]. Combined these effects improve and maintain strength to extended the lifespan of ODS alloys at elevated temperatures.

1.2.2 Knowledge Gaps & Research Objectives

Understanding and predicting the microstructure evolution of nanoparticle-based ODS alloys during rapid solidification in AM processes can speed up the design process [34]. Through simulations, the influence of different parameters, such as nanoparticle properties or cooling profiles, can be varied to reduce the number of experiments and time to find an alloy that meets specifications, such as achieving a certain grain size. A leading simulation approach is phase-field modeling where partial differential equations are used to describe the transformation of microstructures over time, such as alloy solidification [43, 44]. Phase-field models use continuous functions where different order parameters representing features like grain orientations transition smoothly with time. This allows simulations of complex processes to emerge without having to set artificial rules as may be required in a discrete element technique like cellular automata [45, 46]. While phase-field models have been developed that account for both the heterogeneous nucleation and Smith-Zener pinning of nanopar-

ticles [47, 48, 49], they tend to lack the parametric investigation required to understand trends and develop analytical predictions of grain sizes. Other solidification studies also either ignore the impact of nucleation rate or particle concentrations at all [38, 50, 51, 52]. To this end, this thesis presents a parametric phase-field study that simulates the rapid solidification process of nanoparticle reinforced alloys. Specifically, the impact of nucleation rate, nanoparticle concentration, and nanoparticle spatial distribution (agglomerated vs non-agglomerated) on microstructure starting from an initially molten domain both during and after solidification are investigated. The results indicate that the governing mechanism predicting grain size, across the 70 unique 2D cases studied, is the fraction of nanoparticles at grain boundary triple points (where three grain boundaries intersect) with slightly different prediction curves for each particle distribution. This study adds the importance of grain growth kinetics and particle pinning into grain size and corresponding yield strength predictions.

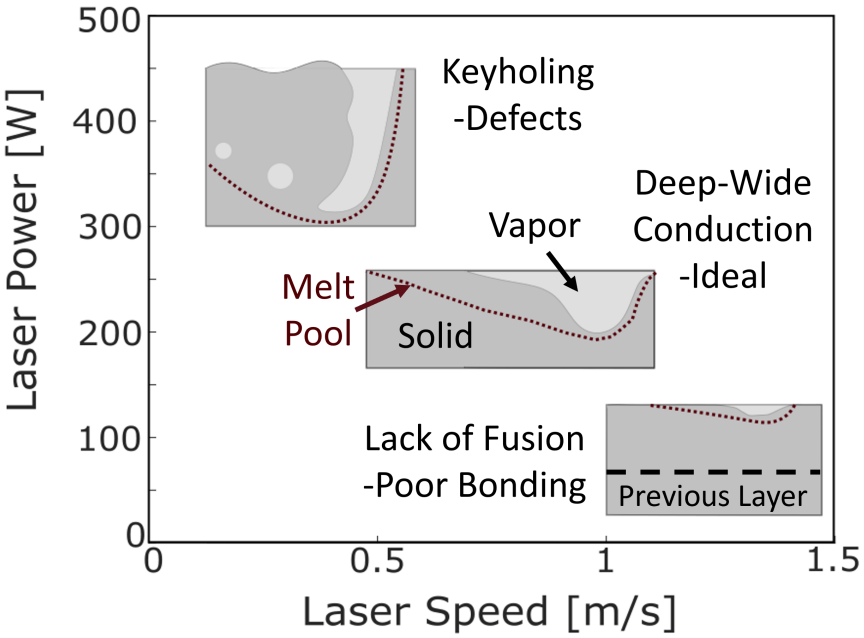


Figure 1.3: Processing map of laser power vs speed with Melt pool and vapor depression morphology regimes.

While the above study focuses on the impacts of nucleation rate in an idealized subdomain that may be seen during the rapid solidification step after a laser has melted the alloy powders, the geometry and dynamics of the melt pool, which is the area of molten metal produced by the laser, plays a crucial role in governing defects and processability of AM alloys [53, 54]. While the low density contrast of the melt pool with the solid phase makes it difficult to identify the melt pool during processing, most laser processing causes vapor

depressions to form that can be more easily identified (Fig. 1.3) [55]. At high laser powers and/or low laser speeds, high levels of metal vaporization occur due to the high laser output, which causes a recoil pressure that forces the melt pool below the surface [55, 56]. This results in keyholing typified by its deep and narrow vapor depression. Excessive keyholing should be avoided as it can increase surface roughness and cause porosity when bubbles separate from the keyhole [55, 57]. At lower laser powers and/or higher laser speeds, melt pools switch to conduction mode. While some vaporization may still occur, conduction dominates melting surrounding powders. Melt pools in this regime are more likely to follow the Rosenthal model, where the laser is approximated as a moving point heat source penetrating a semi-infinite medium of the alloy [58]. This leads to melt pools that are more hemispherical with widths two times or more than the depth. In general, conduction mode is preferred as it is more stable than keyholing. At the far end of the spectrum with very low powers and/or high speeds is the lack of fusion zone. While some metal can still melt or even vaporize in this zone, some fraction of the powder does not melt resulting in incomplete fusion between the spacing layers and/or scans. While post-mortem techniques, such as scanning electron microscopy or micro-computed tomography, can reveal defects they lack the ability to describe evolution of melt pools in real time [55]. *In-situ/operando* synchrotron x-ray imaging, also known as dynamic x-ray radiography (DXR), is a powerful technique to directly image these melt pools and vapor depressions at different laser powers and speeds [55, 59]. By comparing melt pool modes across a variety of conditions, processing maps can be generated which allow researchers to identify starting conditions for best processing [54, 55]. While some DXR studies have begun to directly compare ODS reinforced versus ODS free versions of alloys showing that the ODS particles can significantly impact melt pools [56, 59, 60], these tend to be for higher particle concentrations ($\geq$ 1 wt%). Given the cost addition of nanoparticles it is of interest to understand the impact of nanoparticles at lower concentrations ($<$ 0.5 wt%) where they may be less likely to impact melt pools while still offering strength improvements. To this end, we conducted DXR of two FeCrAl commercially produced alloys, the baseline Kanthal A1 and the oxide dispersion strengthened, Kanthal APM, which has superior creep strength and corrosion properties at elevated temperatures [29, 30, 31]. Kanthal APM only has roughly 0.1 wt% of ZrO_2 nanoparticles added, so it serves as an ideal material to understand how to process these low concentration reinforced alloys. The generated processing maps traverse the keyholing to lack of fusion regimes (Fig. 1.3) serving as an aide for future AM development of these alloys, and furthers the understanding of how dispersed ceramic nanoparticles in a metal matrix impact melt pool geometries. The following hypotheses are investigated for this project.

Hypotheses:

(1) Final grain size is controlled by the fraction of nanoparticles on grain boundaries (at triples points in 2D), which will be influenced by a combination of the solidification process and kinetics, nucleation rate, and particle concentration, size, and distribution. This pinning fraction will be much higher than the classic Smith-Zener equation predicts.

(2) The clustered particle distribution will result in a larger and more varied distribution of solidified grain sizes compared to the random distribution.

(3) The low concentration of ZrO_2 particles (0.1 wt%) will have a minimal impact on the melt pool morphology allowing the same processing maps to be used as a starting point for both particle free and particle reinforced alloys at these low concentrations.

1.3 Integrated Heat and Mass Transfer for Thermochemical Energy Storage

1.3.1 Overview of Salt Hydrate Operation and Principles

Thermal energy storage (TES), which stores heating or cooling potential to be used later, is an efficient and potentially low cost energy storage method used for a variety of applications, such as concentrated solar power, refrigeration, and building heating and cooling [13, 17, 18, 61]. TES can be accomplished with sensible, latent heat/phase change, and thermochemical energy storage [61]. In sensible heating/cooling, energy is stored by simply raising/lowering the temperature of a substance, and the energy storage capacity is directly proportional to the magnitude of the temperature shift. This type of sensible storage is being concertedly built and deployed at commercial scales for concentrated solar power and industrial heating applications where operating temperatures of 700-2000°C enable large temperature shifts with higher storage densities [62, 63]. For building TES applications, temperature swings are limited to $\sim 40-50$°C above ambient, and therefore storage capacities are at most 50 Wh/kg (200 kJ/kg) [64]. To date, the most commonly utilized sensible storage material is water, which owing to its high specific heat (4.184 kJ/kg/K) can reach this upper-bound of 200 kJ/kg. Phase change materials instead store energy as inter-molecular bonds at different physical states of the material, which can get strengthened/weakened upon freezing/melting respectively [61, 65]. These energy capacities are around 40-100 Wh/kg (150-360 kJ/kg) with organic (e.g. paraffins), inorganic (e.g. metallics), and eutectics (e.g. fatty acids) being the three main types [65]. For building applications a common example is embedding paraffin wax or other phase change material into the building envelope to reduce temperature swings across day and night cycles [17, 61]. Since phase change materials freeze/melt at constant temperature care must be taken to select/tune the material to operate at the

target temperature. Thermochemical materials store energy in chemical bonds, and results in relatively larger energy densities (on both a gravimetric and volumetric basis) compared to phase change and sensible energy storage materials [5, 66, 67]. These energy densities have been reported to be as high as 550 Wh/kg (2 MJ/kg) [67, 68, 69, 70]. Heat released in an exothermic reaction with a thermochemical material can be stored with the reversible, endothermic reaction. Since the energy is stored in chemical bonds, thermochemical materials can be stored loss free without insulation which is not the case for sensible and latent heat materials [66].

For building heating applications, 20-60°C, which includes both space heating and hot water applications, two of the most common thermochemical materials are sorption materials such as zeolite and silica gels [71, 72] and salt hydrates such as $MgCl_2$, $CaCl_2$, $SrCl_2$, $SrBr_2$, $MgSO_4$ and K_2CO_3 [64, 66]. At higher temperatures, 500-1500°C, redox reactions of materials like calcium oxide and ceria are used for concentrated solar power, although this dissertation does not explore materials for high temperatures [73, 74]. In sorption materials, a gas, such as water vapor, is adsorbed/desorbed to/from the surface of the material [75]. In contrast, for salt hydrates water vapor reacts with the salt forming a hydrated salt compound, which typically results in higher energy densities [64]. This thesis explores salt hydrates due to their high energy densities, relatively low recharge temperatures, fast kinetics, stability, and ability to be embedded in composite hosts to increase cyclability [66, 76, 77]. Salt hydrates are assessed for their potential to provide warm air for space heating of buildings with application temperatures between 20-40°C.

The basic reversible salt hydration reaction is shown in Eq. 1.1 [66]

$$\mathrm{M \cdot (n-m)H_2O(s) + mH_2O(v)} \longleftrightarrow \mathrm{M \cdot nH_2O(s) + Heat} \tag{1.1}$$

where M is the base salt, n is the number of moles in the hydrated salt and m is the number of moles involved in the hydration/dehydration reaction. The salt hydrate remains solid throughout the reaction. When salt hydrates absorb water vapor from moisture in the air this releases heat (exothermic), which can be used for building space heating. To recharge (endothermic) dry and/or heated air from the heat pump flows through the hydrated salt releasing water vapor until the salt is dehydrated.

Fig. 1.4 shows how a salt hydrate reactor might be integrated into a home for space heating [17]. In default mode, the heat pump bypasses the reactor and operates as normal. In stage 1, the salt is charged using the heat pump (or other heat source such as a solar collector) to warm up the air to release stored water vapor in the salt. This is may be done when there is excess solar or cheap electricity prices [78, 66]. During discharge/heating (step 2), the heat pump is turned off and cold air enters the reactor. Through the hydration

reaction the air is warmed and released into the building. These steps are repeated to cycle the reactor. While salt hydrates can also be used for building cooling, they typically have slow reaction kinetics below 10°C due to their low equilibrium vapor pressures [66].

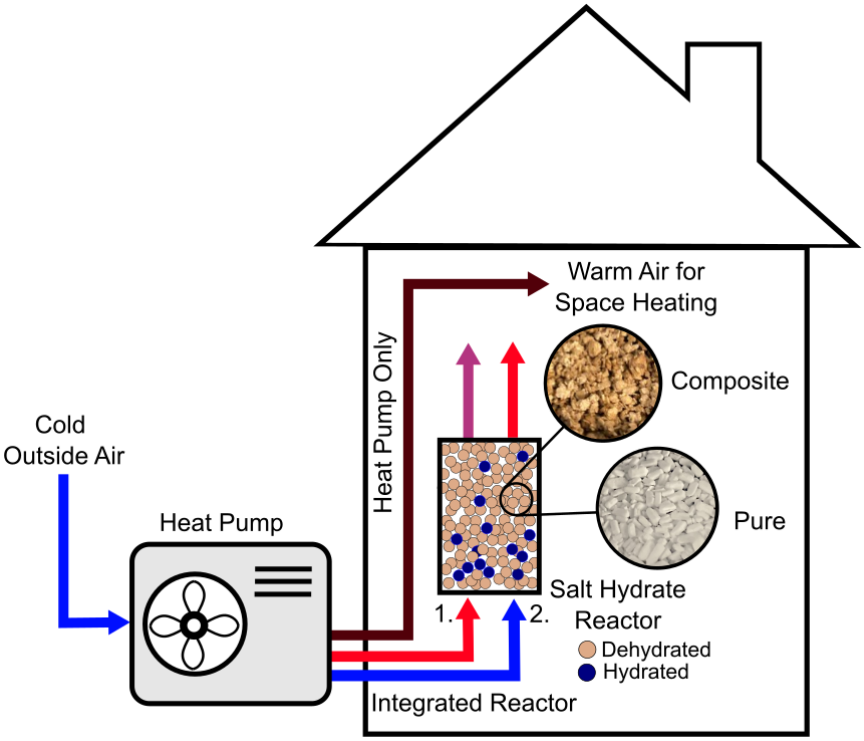


Figure 1.4: Space heating operation of salt hydrate reactor. Stage 1 is reactor charging (dehydration) and stage 2 is discharging (hydration). Insets show different form factors of salt hydrates, pure ($MgSO_4$) and composite ($SrBr_2$).

The operating window for salt hydrates is determined by its Clausius-Clapeyron equation (Eq. 1.2) [79].

$$p_{\text{eq}} = exp\left(\frac{-\Delta H}{RT} + \frac{\Delta S}{R}\right) \tag{1.2}$$

This equation is fit by measuring the onset of hydration of a salt across several temperatures and water vapor pressures [4]. The reaction enthalpy, ΔH, and reaction entropy, ΔS, are assumed constant across the temperature range of interest, and can be determined either experimentally or estimated from first principles thermodynamics calculations [4, 67]. An example Clausius-Clapeyron diagram for a salt hydrate is shown in Fig. 1.5. The farther away from the dotted line the faster the reaction typically occurs. Above the deliquescence line the salt starts forming a solution [80]. Although this can improve energy densities by adding on latent heat storage to the salts, it typically reduces cyclability as salt particles

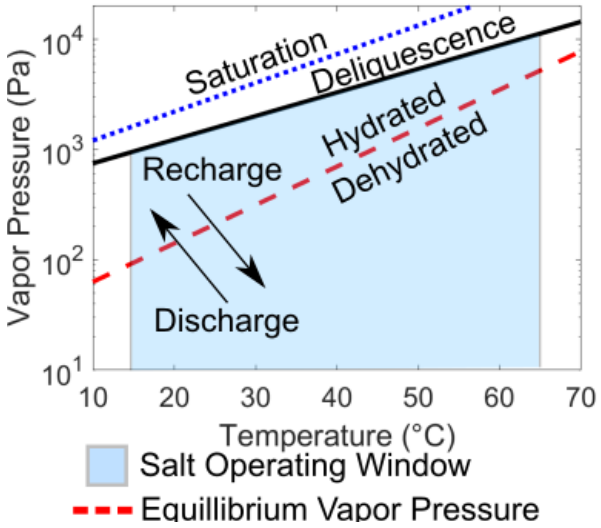


Figure 1.5: A model Clausius Clapeyron Diagram for a typical salt. Arrows represent direction temperature and/or water vapor pressure must go to drive the reaction.

tend to clump together reducing exposed surface area decreasing salt kinetics [76]. Every salt has a different Clausius-Clapeyron relation and deliquescence line, so salts should be selected based on operating window requirements as well as climate since weather dictates the ambient humidity and temperature if sourcing water vapor from the ambient [66, 81].

1.3.2 Knowledge Gaps & Research Objectives

Traditionally, salt hydrates have been targeted for seasonal storage, where heat produced by roof-top solar collectors is used to dehydrate several tons of salt over the entire summer season. Then, during winter the charged salt is slowly hydrated to produce heat for the building [66, 82]. The systems are usually sized to meet entire winter heating loads for a typical European dwelling of 10 GJ or 2778 kWh using several tons of salts [66, 81, 83]. In recent years, salt hydrate reactors are increasingly being developed that can discharge on the daily scale, 4-10 hours, which offer lower initial capital costs due to reduced system size [17, 81, 84]. A typical American home may only need 8 kWh of storage, a few dozen kilograms of salt hydrate, to meet a recent Department of Energy target to shift 4 hours of peak home loads [69, 85]. Many electric utilities now have variable electric rates based on user demand and increasingly available solar/wind resources [78, 86]. By charging the reactor when electricity prices are cheap and discharging when prices are high, this approach for salt hydrates has been shown to reduce annual electricity costs by up to $200 in a representative cold climate city of Detroit, Michigan, USA [78]. Alternatively, salt hydrate reactors can

reduce peak loads by up to 30%, which can reduce blackouts on the grid [78].

At the low discharge rates of seasonal storage (< 1 W/kg) [81, 87, 88, 89, 90, 83], reactors output a constant, low power/temperature profile where power is limited by the transport/supply of water vapor. As the discharge rates increase to that for daily cycling (∼15-100 W/kg), the reaction rate is now limited by the magnitude of the salt hydrate kinetics and is marked by power profiles that initially peak and then slowly decrease as the salt is consumed. In this kinetics regime, only a fraction of the total stored energy may be accessed within the 4-10 hour timeframe of interest for load shifting [72, 91, 92]. However, there remains a lack of studies on determining the onset of this mass transport to kinetics transition. To this end we use a modified Damkohler number, which compares the characteristic salt reaction rate to the rate of water vapor transport [93]. Through multiphysics simulations coupled with experimental reactor demonstration, we used the Damkohler number to analytically predict this transition based on inlet conditions and salt hydrate properties and how changes in reactor design and operation will affect power output in the mass transport regime. To probe tradeoffs in energy and power, it is common to use the Ragone framework, where the time averaged specific power (W/kg) is plotted against the total specific energy (Wh/kg) used up until that point [94]. While this framework has been used for the Li-ion battery as well as the phase change community [5, 72], it has yet been extended to salt hydrate thermochemical reactors. To this end, we use the multiphysics model to explore the impact of reactor design including air velocity, inlet relative humidity, reactor length, and salt kinetics on tradeoffs between reactor power and energy using the Ragone framework. We use our modified Damkohler number to identify key characteristics of Ragone profiles across the mass transport to kinetics limited regimes. We extend this analysis to assess the experimental performance of a $SrBr_2$ vermiculite composite reactor, which is a leading salt hydrate [77, 95, 96], for daily cycling. Given the relative lack of studies on how power and energy tradeoffs transition from material kinetics to reactor operation [91, 97], we fill this gap by directly projecting reactor performance based on experimentally measured material scale kinetics and comparing against reactor results. Results reveal a significant decrease in effective kinetics when scaling the composite from the small (1 g) material scale to larger (100 g) reactor scale suggesting the importance of improved material characterization to achieve high power output.

A second major issue preventing adoption of salt hydrates is their limited cyclability after a few or even one repeated hydration and dehydration cycles [83, 98]. When pure salts hydrate and dehydrate they tend to swell and contract, which can cause salt particles to agglomerate. This can block water vapor diffusion pathways preventing or slowing down further cycling [79, 99, 100]. Agglomeration can largely be avoided by embedding salt hydrates in a porous

host, which keeps open diffusion pathways even as the salt swells during repeated cycles [101]. However, this comes at the expense of reduced energy capacity since the composite hosts are largely inert [101], so there is motivation to study salt hydrates in both their pure and composite forms. Salt hydrates are typically first analyzed using a technique like thermogravimetric analysis where a few milligrams of salt are put into a sample holder a few millimeters tall [4, 79]. As air at a preset moisture content flows over the salt the mass change is tracked over time. Even in this small length scale, certain salts exhibit slow downs in hydration kinetics and rates that are hypothesized to be due to the formation of a water vapor diffusion barrier [79]. However, there remains a lack of direct evidence of this agglomeration happening in real time. *Operando* techniques, such as nuclear magnetic resonance, magnetic resonance imaging, and infrared imaging have been used to directly visualize salt hydration on the reactor scale [91, 102, 103, 104], but due to their coarse resolution of 2-15 mm, they are unable to study systems on the few millimeter scale of thermo-gravimetric analysis. Optical microscopy has improved spatial resolution but lacks the phase contrast to easily distinguish between hydrated and dehydrated samples [100]. 2D neutron radiography imaging offers improved spatial resolution and has been used to study Li-ion cycling [105] as well as reactor scale ammoniated salts, which absorb and release ammonia (NH_3) rather than water [106, 107]. However, neutron imaging has not yet been applied to thermochemical salt hydrates nor to hydration on the material length scale. That is why in this work, neutron imaging, which has excellent sensitivity to water uptake and can have a spatial resolution of 42 μm (ten to one-hundred times better than existing techniques) [108], is used to study salt hydration in a setup representing thermo-gravimetric analysis for both pure and composite salts. Using insight gained from the lab scale reactor study, neutron imaging is also applied to offer improved spatial resolution in understanding how changes in air inlet velocity impact the hydration profiles for a modified $SrBr_2$ vermiculite reactor. The following hypotheses are investigated for this project.

Hypotheses:

(1) Ragone plots for salt hydrate thermochemical energy storage will be influenced by reactor design and operating regimes of mass transport and kinetic limitations.

(2) The transition between mass transport and kinetics regimes can be analytically predicted by a Damkohler number, which factors in inlet air velocity and humidity, salt kinetics, and reactor length. In the mass transport regime the power output can be predicted as a function of Damkohler number for a given salt.

(3) Effective kinetics will decrease when scaling from the small material scale to the larger reactor scale due to difference in salt morphology and temperature between the experiments.

(4) Neutron imaging is a powerful platform enabling improved spatial resolution compared

to prior techniques for studying the (de)hydration of salt hydrates at both the material and reactor scale.

(5) Cycling of pure $SrBr_2$ is limited due to significant swelling of the salt during hydration. Neutron imaging will reveal direct evidence of this water diffusion barrier forming, which slows down hydration rates, and how this barrier is reduced for the $SrBr_2$ vermiculite composite.

1.4 Thesis Outline & Research Contributions

This thesis encompasses four research chapters, covering both experimental and modeling work in the areas of oxide dispersion strengthening alloys and salt hydrates for building space heating. Some of the key contributions of this thesis are *operando/in-situ* imaging techniques that track additive manufacturing of alloys as well as hydration cycling of salt hydrates. These images provide fundamental understanding of these processes to help advance the field. While still frames are shown for some of these videos in the thesis, these results are best viewed as videos. Since the reader is most likely to access this thesis as a PDF and owing to ever changing supported video formats, please find these videos by accessing them in their online publications. These videos are currently hosted on my university legacy Google Drive at this link. When the reader sees references to videos in this dissertation go to the referred Google Drive location. These may be moved to the University of Michigan's Deep Blue dissertation repository depending on future alumni Google Drive permissions although again the best location to find videos is in their online journal publication.

Chapter 2 has been modified from a paper published in JOM [27]. It presents an open-source phase-field model developed to understand the impact of nucleation rate as well as nanoparticle size and concentration have on alloy microstructure during the rapid solidification process typically seen during additive manufacturing. Rohini Bala Chandran and Bryan Kinzer conceptualized the research and developed model formulations. Bala Chandran acquired funding and supervised. Kinzer conducted software development and formal analysis. Kinzer and Bala Chandran wrote the draft and reviewed and edited the manuscript. The PRISMS-PF open source model is available on Kinzer's Github page (link) [109].

Chapter 3 contains results of the dynamic X-ray radiography experiments conducted on the ODS particle free Kanthal A1 and the ODS reinforced Kanthal APM. Kinzer and Jerard Gordon wrote a proposal to conduct experiments at the 32-ID-B beamline at Argonne National laboratory. Samuel Clark led setup of the beamline experiments at Argonne along with assistance from Kamel Fezzaa also of Argonne. Beamline experiments were conducted by Kinzer, Dillon Jobes, Daniel Rubio-Ejchel, and Yaozhong Zhang of the University of

Michigan. Brandon Surhigh assisted with polishing of the alloys for preparation. Gordon, Bala Chandran, Kinzer, Jobes, and Rubio-Ejchel helped with conceptualization of the work. Kinzer and Jobes conducted data analysis. Kinzer and Bala Chandran wrote the section. Bala Chandran and Gordon acquired funding and supervised. Plans are to convert the results into a letter.

Chapter 4 is adapted from a recently submitted manuscript under review. A salt hydrate model is developed that explores the impact of reactor design and operation on power output showing that increases in operating velocity have a diminishing return on output power upon transitioning from the mass transfer to kinetics limited regime. Experimental testing of a salt hydrate reactor provides additional insight on how theoretical predictions translate into real-world performance. Bala Chandran acquired funding and supervised. Bala Chandran and Kinzer conceptualized the research. Kinzer and Bala Chandran developed the multiphysics model. Kinzer and Arijit Jatkar designed and made the humidistat that controls the experiment. Durga Ghosh, Kinzer, and Declan Crowley developed and tested the salt hydrate reactor and optimized material synthesis. Kinzer and Bala Chandran wrote the modeling sections. Ghosh, Kinzer, and Bala Chandran wrote the experimental section. Kinzer wrote the initial drafts of the Introduction and Conclusion. Bala Chandran, Kinzer, and Ghosh revised the manuscript. Yuxuan Zhang of Oak Ridge National Laboratory conducted neutron computed tomography experiments to determine porosity and internal structure of the $SrBr_2$ composite.

Chapter 5 presents results adapted from a manuscript under preparation for *operando* neutron imaging experiments of salt hydrate hydration and dehydration conducted at Oak Ridge National Laboratory (ORNL) at the MARS CG-1D HFIR beamline. The chapter tracks hydration states of salt hydrates for a setup representing material scale thermogravimetric analysis as well as preliminary through flow reactor characterization. Bala Chandran and Kinzer conceived the research. Bala Chandran acquired funding and supervised. Kinzer and Jatkar designed, assembled, and tested the reactor at the University of Michigan. Crowley helped with reactor testing as well. Kinzer and Bala Chandran conducted experiments at ORNL. Zhang and Erik Stringfellow coordinated experiments and led the setup of experiments at ORNL. Jean-Cristophe Bilheux developed Jupyter notebooks to help with data analysis. Kinzer, Bilheux, and Bala Chandran conducted data analysis. Kinzer drafted the initial chapter and Bala Chandran and Kinzer revised the chapter.

Chapter 6 presents the conclusions and suggests future directions based on takeaways from the studies of this thesis. Supplementary Information is included in Appendices A, B, and C.

CHAPTER 2

A Phase-Field Study on the Effects of Nucleation Rate and Nanoparticle Distributions on Solidification and Grain Growth

Adapted with permission from: Kinzer, B., Bala Chandran, R. "*A Phase-Field Study on the Effects of Nucleation Rate and Nanoparticle Distributions on Solidification and Grain Growth*". *JOM* **76**, 496–509 (2024) [27].

2.1 Introduction

Alloys containing a dispersion of nanoparticles offer the potential to enable next generation high temperature, high strength alloys [22, 110, 111, 112, 113]. Embedding ∼10–100 nm ceramic particles, such as TiC, TiB_2, Y_2O_3, and Al_2O_3, has been shown to nearly double yield stress and improve creep performance from room temperature to elevated temperatures ($\geq$ 800 °C) as compared to standard particle-free alloys [24, 25, 26, 114]. Metal matrix nanocomposite alloys, such as Ni-based MA6000 and ferrous Kanthal APM, have been manufactured through conventional powder metallurgy involving mechanical alloying with subsequent hot rolling and extrusion [113, 32, 31]. Recently, laser additive manufacturing processes, such as selective laser melting (SLM), are also increasingly being explored for the fabrication of complex geometries for metal nanocomposites [22, 33, 6, 115, 28].

Addition of nanoparticles improves alloy mechanical properties by reducing average grain size and preventing grain growth [39]. Nanoparticles serving as grain nucleation sites can arrest columnar grain growth resulting in a finer, more equiaxed microstructure capable of achieving grain sizes on the order of a few microns to a few hundred nanometers [24, 116, 117, 118, 35]. In this grain size range, further size decreases improve yield strength

by increasing the density of grain boundaries that serve as obstacles for dislocations [114]. Traditionally, grain size in the presence of pinning particles has been analyzed through the Smith-Zener Equation [42]. This provides an estimation of the average grain size as a function of volume fraction (nanoparticle concentration) and nanoparticle size [42, 119]. However, there is often a discrepancy between the classic Smith-Zener Equation prediction and experimentally measured grain size [42, 120]. The main focus of our study is to use phase-field modeling to create an improved nucleation rate dependent Smith-Zener Equation of rapidly cooled alloys, such as during SLM, both during and after solidification for multiple distributions of nanoparticles.

The original Smith-Zener Equation is derived by balancing the driving pressure for grain growth against the pinning pressure of a uniform distribution of particles but ignores how grain growth actually occurs [42]. Many modifications have been made to the Smith-Zener Equation including accounting for nanoparticles preferentially laying on grain boundaries [121, 122]. Grains grow until they are pinned by particles making the fraction of nanoparticles laying on grain boundaries much higher than Smith-Zener predicted. This increase in pinning pressure results in a smaller, more accurate grain size prediction. However, most of these studies have focused on grain recrystallization and annealing [42, 123]. While recent studies accounting for both heterogeneous nucleation and particle pinning of alloy solidification have been conducted, they fail to establish modified Smith-Zener Equations and lack investigation into nucleation rate [34, 50, 51]. Johnson-Mehl-Avrami-Kolmogorov (JMAK) analysis provides a general solid phase transformation framework, which predicts that crystal/grain size is inversely dependent on the nucleation rate [124, 125]. Therefore, there is a need to connect the classic Smith-Zener model with inferences from JMAK analysis to quantitively capture the influence of nucleation rate on grain size for nanocomposite solidification.

An additional challenge of manufacturing nanocomposites is agglomeration/clustering of nanoparticles, which can occur either during the rapid solidification of the molten metal or due to insufficient mixing of powders during ball milling [6, 52, 37, 36]. Clustering causes inhomogeneities in the microstructure and weakens the alloy. While modeling particle agglomeration is outside the scope of this paper, we also compare simulations of static beds of uniform and clustered particles to explore the impact of particle distribution on the Smith-Zener Equation. Most prior studies preclude the effects of nucleation rate or particle distribution on microstructure evolution. Even if included, these analyses are limited to very small volume/area fractions (<0.001), ignore particle pinning, and/or ignore heterogeneous nucleation [50, 51, 52, 38].

Phase-field modeling is a powerful tool to understand complex microstructure evolution

and has been deployed to study grain growth in the presence of nanoparticles exerting Smith-Zener pinning of grain boundaries [47, 48, 49]. The primary objective of this study is to explore the impact of nucleation rates on microstructure evolution using phase-field simulations and develop a modified Smith-Zener Equation for different particle distributions. Nanoparticles are modeled to serve as nucleation sites during solidification and exert grain boundary pinning forces. Simulations are performed on a two-dimensional modeling domain to explore the effects of (a) nucleation rates, (b) nanoparticle concentration quantified by area fractions (0.01, 0.02, 0.03, 0.05, and 0.10), and (c) particle distributions (random and clustered) on the transient evolution of average grain size and microstructure. A few preliminary 3D cases are also explored. Although model parameters are taken from specific metals/processes, the takeaways for this paper are meant to emphasize general trends expected for rapid solidification of nanocomposite alloys. Notable advancements in our work compared to prior studies are: (1) development of a modified nucleation rate dependent Smith-Zener Equation; and (2) quantification of the impact of particle distribution on alloy solidification and steady-state grain size. Our 2D results illustrate that for a wide variety of area fractions and particle distributions, the nucleation rate, by impacting the fraction of nanoparticles at grain boundary triple points (the intersection of three grains), has a significant impact on grain size and thus alloy strength.

2.2 Methods

Two-dimensional (2D) phase-field simulations are conducted using the open-source software PRISMS-PF (PRedictive Integrated Structural Materials Science Phase Field), which is a parallelized matrix free finite element solver to determine microstructure evolution. For more details of the code the reader is referred to this paper [43]. Parametric studies are performed in 2D as they are much more computationally efficient than 3D simulations (2D is 100 to 1000 times faster). While solidification dynamics, grain boundary pinning forces, and micro-structure evolution will behave differently in 2D and 3D simulations (see Section 2.4.2), we expect that the general trends for the dependence of grain size on nucleation rate and nanoparticle concentration will be comparable [42].

In phase-field models, governing equations are formulated to represent thermodynamic driving forces for grain growth, for interactions between grains, and for kinetic parameters that dictate the rate of microstructure evolution. Compared to other modeling approaches, such as cellular automata where grains and interfaces are represented by cells with discrete states [45], phase-field simulations treat interfaces to be diffuse with the order parameters transitioning smoothly across the width of the interface [43]. This smooth transition allows

for implicit tracking of complex grain morphologies/features, such as triple points, without the need of additional rules.

2.2.1 Modeling Domain

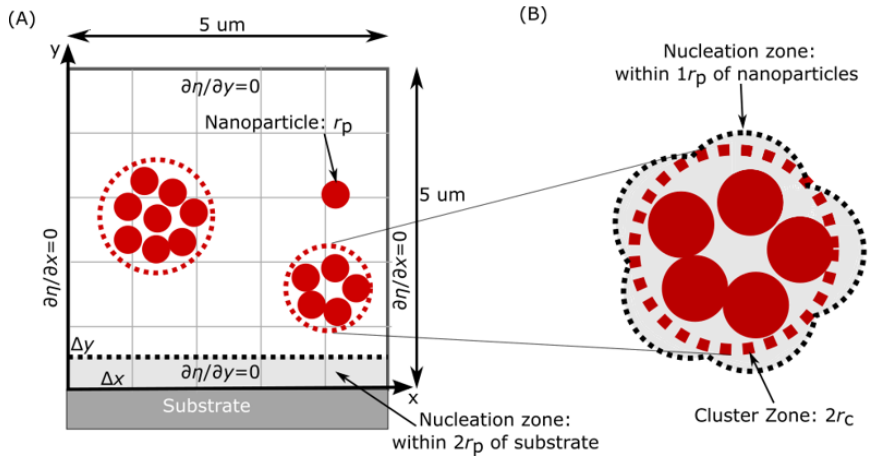


Figure 2.1: Computational domain. (a) Schematic of the computational domain with a mesh size of 39 nm × 39 nm (not to scale) and with a sample clustered distribution of monodisperse nanoparticles with radius of $r_p = 25$ nm. (b) Aggregations of individual nanoparticles form clusters based on size distribution data with the cluster zone denoted by the dotted red circle with radius, r_c. The shaded region bounded by the dotted black curves within 1 r_p of each nanoparticle and within 2 r_p of the substrate wall represents heterogeneous nucleation zones.

Fig. 2.1a shows the 2D, 5 μm × 5 μm, modeling domain and boundary conditions for the phase-field simulations. The simulations represent a simplified, subdomain during rapid solidification, nucleation during solidification, and continued grain growth after solidification of an alloy near the substrate or previously solidified layer, such as that seen in a selective laser melting (SLM) process. This domain size enables tracking several hundred nanoparticles and up to several hundred grains to yield statistically meaningful results while remaining computationally tractable. Typically, reinforcing nanoparticle radii range from 5–50 nm to have a discernable impact on alloy strength. Therefore, we use a baseline particle radius, r_p, of 25 nm for all simulations [6]. Depending on the distribution, nanoparticles are placed into discrete cluster zones (Fig. 2.1a,b). The code is based on the standard Allen-Cahn grain growth module in PRISMS-PF with two added functionalities to account for inclusion of particles [126]. First, we include the capability of nanoparticles and the substrate to serve as heterogeneous nucleation sites during solidification, so that new grains can preferentially solidify around the nanoparticles and the substrate [127, 128]. Nucleation can occur within 1 r_p of a nanoparticle (Fig. 2.1b) or within 2 r_p of the substrate (Fig. 2.1a,1b). Second,

we include Smith-Zener grain boundary pinning, as nanoparticles pin the grain boundaries limiting grain growth/coarsening, which reduces the final, steady state grain size [34, 48]. While micro-segregation of elements is likely to occur, even for the high cooling rates and thermal gradients of this study [25, 129], reasonable agreement for our system of SS316L plus TiB_2 nanoparticles between model and experiment is possible on the micro-scale while ignoring these effects [25, 123]. Therefore, this model also assumes a uniform composition across the grains, which keeps the model computationally tractable.

2.2.2 Nanoparticle Distributions in the Metal Matrix

We model the effects of two distinct spatial distributions for the nanoparticles: (a) random and (b) clustered. A control case is also modeled without any nanoparticles present in the microstructure [7]. We assume nanoparticle clusters are fixed in place at the beginning of solidification. In reality, randomly distributed nanoparticles will dynamically cluster, which will impact grain nucleation. However, static clustering is implemented to isolate the effects of clusters on microstructure evolution. Five area fractions, which is the ratio of the total area occupied by the particles (area per particle is πr_{p}^2) to the domain area (5 μm $\times$ 5 μm), spanning an order-of-magnitude variation, $\Phi_{\mathrm{np}} = 0.01$, 0.02, 0.03, 0.05, and 0.1 are modeled. It can be assumed area and volume fractions are equivalent when the nanoparticle concentration is consistently scaled from 2D to 3D [130]. This range includes typical area fractions used in practical applications of nanoparticle alloys [22, 6, 7]. For the random distribution, a 25 nm radius particle is placed at each randomly sampled site from a uniform distribution of spatial coordinates within the modeling domain. Particle overlap is prohibited, and new particle centers are generated until the area fraction is reached. To model realistic clusters of nanoparticles in a metal matrix, we applied experimentally measured cluster size distributions by Gu and coauthors, where Ni-based Inconel 718 nanocomposite with 25 nm radius TiC particles was manufactured via selective laser melting [6]. To generate the clustered distributions of particles in our modeling domain (Fig. 2.1a), coordinates for the center of the cluster are randomly seeded. Individual 25 nm particles are randomly placed within the cluster zone until no more particles can be placed without causing particle overlap (Fig. 2.1b). After one cluster is placed, this process is repeated until the target area fraction is attained. The cluster size distribution is obtained from the laser processing settings that resulted in an approximately 275 nm average cluster zone radius (Fig. A.1)(see Appendix A material), which still yielded structurally stable coupons [6].

2.2.3 Governing Equations for Phase-field Model

Each grain is assigned an order parameter, η_{i}, representing a grain orientation with i ranging from $N = 1, 2, ..., 16$. Grains are represented by discrete areas where $\eta_{\mathrm{i}} = 1$ within the *ith* grain orientation and smoothly transitions from a value of 1 to 0 across the grain boundary interface. φ is an additional variable that represents the nanoparticles. The following governing equations are largely adapted from Wang et al. unless otherwise noted [7].

Microstructure evolution, including grain size and orientation, is dictated by the configuration that minimizes the free energy of the system, F_{sys} (Eq. 2.1)

$$F_{\mathrm{sys}} = \int_V f_0 \, \mathrm{d}V, \tag{2.1}$$

which is applied in every dV, differential element volume of the domain. For 2D simulations, we assume a depth of one unit to allow the use of 3D material properties. f_0 is the free energy density functional consisting of local and gradient terms in Eq. 2.2,

$$f_0 = f_{\mathrm{local}} + f_{\mathrm{grad}}. \tag{2.2}$$

f_{local} is dictated by the free energies of the grains, whereas f_{grad} penalizes sharp gradients and is formulated to impose ideal pinning of grain boundaries. Both these free energies drive grain coarsening where smaller grains are consumed by larger grains to reduce the total interfacial area. f_{local}, is given by Eq. 2.3,

$$f_{\mathrm{local}} = m_{\mathrm{g}}(\sum_{i=1}^{N}(-\frac{1}{2}\eta_{\mathrm{i}}^2 + \frac{1}{4}\eta_{\mathrm{i}}^4)) + m_{\mathrm{g}}(\gamma \sum_{i=1}^{N}(\sum_{j\neq i}^{N}(\eta_{\mathrm{i}}^2\eta_{\mathrm{j}}^2)), \tag{2.3}$$

The first term is a double-well free energy functional with global minima at $\eta_{\mathrm{i}} = \pm 1$ and a maximum at $\eta_{\mathrm{i}} = 0$ [44]. Since the liquid phase corresponds to $\eta_{\mathrm{i}} = 0$, the driving force for converting the initial liquid phase into solid grain growth is to reduce this local free energy. The second term penalizes the physically unrealistic outcome of two grains coexisting in the same location. γ, the grain interaction coefficient, is set to 1.5, because it ensures that the order parameters transform at a constant, symmetric rate, i.e., $\partial\eta_{\mathrm{j}}/\partial\eta_{\mathrm{j}} = -1$ [47]. Both terms in Eq. 2.3 are scaled by m_{g} (Eq. 2.4), which is an interface coefficient tuned to control the width of the grain boundary for simulation stability,

$$m_{\mathrm{g}} = \frac{3}{4}\frac{\sigma_{\mathrm{g}}}{\Delta f_{\mathrm{g}} l_{\mathrm{g}}} \tag{2.4}$$

where l_{g} is the grain boundary width, and σ_{g} is the grain boundary energy, which is

assumed to be the same as the solid-liquid interfacial energy; Δf_{g} is the maximum energy barrier of the normalized local free energy, $f_{\mathrm{local}}/m_{\mathrm{g}}$ in Eq. 2.3 [7, 48].

Other studies have introduced an additional term into f_{local} to model finite pinning forces, which may lead to grain boundary detachment [27,48]. In contrast, we instead attach φ to f_{grad} in Eq. 2.5. $\varphi = 0$ inside a nanoparticle, and $\varphi = 1$ outside. This formulation introduces a free energy discontinuity making it so it is never favorable for a grain boundary to detach even for high grain boundary curvatures, thus perfect pinning is induced. This simplification allows the focus to remain on impact of nucleation rate and particle clustering rather than the magnitude of the pinning force, which can vary based on choice of nanoparticle.

The second term of Eq. 2.2 is the gradient term given by Eq. 2.5

$$f_{\mathrm{grad}} = \frac{\kappa_{\mathrm{g}}}{2}\varphi \sum_{i=1}^{N} |\nabla \eta_{\mathrm{i}}|^2. \tag{2.5}$$

κ_{g} is a positive gradient coefficient (Eq. 2.6) [44]

$$\kappa_{\mathrm{g}} = a_{\mathrm{k}} \sigma_{\mathrm{g}} l_{\mathrm{g}}, \tag{2.6}$$

where a_{k} is the anisotropic grain boundary energy coefficient. κ_{g} scales the local gradient, $\nabla\eta$, so a larger value of κ_{g} penalizes sharp interfaces, making the grain boundary interface more diffuse [131]. a_{k} scales the ratio of the gradient free energy and grain growth rate. While a_{k} can be set based on physical constants [7, 44], we arbitrarily set a_{k} to 0.15, which we found led to numerically stable simulations. Across a typical grain boundary, the order parameter spatial gradient for any grain orientation is non-zero, i.e., $\nabla \eta_{\mathrm{i}} \neq 0$ [132].

The evolution of the grain microstructure is obtained by computing the spatiotemporal evolution for each order parameter, η_{i}, using the Ginzburg-Landau equation (Eq. 2.7 [131]). Taking the partial derivative of f_0 with respect to η_{i} using the terms of Eq. 2.2, and scaling by L_{g} leads to

$$\frac{\partial \eta_{\mathrm{i}}(\vec{r},t)}{\partial t} = -L_{\mathrm{g}} \frac{\partial f_0}{\partial \eta_{\mathrm{i}}(\vec{r},t)} = -L_{\mathrm{g}}(m_{\mathrm{g}}[-\eta_{\mathrm{i}} + \eta_{\mathrm{i}}^3 + 2\gamma\eta_{\mathrm{i}} \sum_{j\neq i}^{N} \eta_{\mathrm{j}}^2] - \varphi\kappa_{\mathrm{g}}\nabla^2\eta_{\mathrm{i}}), \tag{2.7}$$

where $\vec{r}$ is the spatial coordinate, t is time, and L_{g} is a constant introduced to scale the temperature-dependent rate of grain growth [27]. The nanoparticle positions are fixed in size and position across all time. L_{g} is given by Eq. 2.8,

$$L_{\mathrm{g}} = \frac{1}{a_{\mathrm{k}}} \frac{1}{l_{\mathrm{g}}} D_0 \exp(-\frac{Q_{\mathrm{g}}}{RT}), \tag{2.8}$$

where D_0 is a pre-exponential constant for grain boundary mobility, Q_{g} is the activation

energy for grain boundary mobility, and R is the ideal gas constant.

2.2.4 Grain Nucleation and Remapping

The simulations implement classic nucleation theory, and assume heterogeneous nucleation dominates [133]. Classic nucleation theory is deployed given its use in PRISMS-PF and ability to match experimental microstructures from recent rapid solidification phase-field simulations [34, 7]. Heterogeneous nucleation only occurs at preferential sites of solid surfaces that reduce the free energy to form a nucleus, including the imperfections on the substrate wall and on the nanoparticle surfaces (Fig. 2.1a). When a new nucleus is formed it is randomly assigned an order parameter between $N = 1$–16. While the nucleus radius will vary with the extent of undercooling, we assume all nuclei are generated at a constant radius of 25 nm for simplicity.

The areal nucleation rate equation, J^*, is given by Eq. 2.9 [7, 134]:

$$J^* = N_{\text{sites}} \frac{k_{\text{B}} T}{h} \exp(-\frac{Q_{\text{D}}}{RT}) \exp(-\frac{\Delta G^* \xi_\theta}{k_{\text{B}} T}), \tag{2.9}$$

where N_{sites} is the areal number density for nucleation sites, k_{B} is the Boltzmann constant, and T is the local temperature (Fig. 2.1a), which is dictated by the cooling rate and spatial temperature gradients. Direct measurement of N_{sites} is difficult, and therefore we evaluate grain size as a function of N_{sites} using a baseline value of 1.95×10^9 nuclei/m^2. In the remainder of the text, this baseline value is referred to as $N_0 = 1$. A range of $10^{-3}N_0 - 10^3 N_0$, i.e. $1.95 \times 10^6 - 1.95 \times 10^{12}$ nuclei/m^2 is used allowing us to explore a wide range of microstructures with the number of nucleated grains ranging from a dozen to a few hundred inside the domain (Table 2.1). Assuming a dimensional scaling by a power of 3/2 to transform nucleation sites from a per area to per volume basis, the range of N_{sites} considered in our study becomes equivalent to $10^9 - 10^{18}$ atoms/m^3 [135]. Prior 3D studies have covered ranges from $10^{13} - 10^{15}$ atoms/m^3 [34, 46]. In the first exponential term in Eq. 2.9, Q_{D} is the activation energy for atomic diffusion. The second exponential term signifies the probability that the nucleus formed acquires a critical size. This probability depends on a contact angle function, ξ_θ, based on the wettability of the nucleus with the nanoparticle/substrate surface and the energy barrier, ΔG^*, to form critically sized nuclei. The contact angle function, which governs the heterogeneous nucleation shape factor, is given by Eq. 2.10,

$$\xi_\theta = \frac{1}{4}(2 + cos(\theta))(1 - cos(\theta))^2. \tag{2.10}$$

A constant contact angle of $\theta = 4°$, indicative of low surface tension and extremely good

wettability, is assumed for both nanoparticles and the substrate (Fig. A.2) [7]; this results in $\xi_\theta = 4.4 \times 10^{-6}$. In the liquid melt, $\theta = 180^\circ$ and $\xi_\theta = 1$, which results in a much smaller nucleation rate allowing us to ignore homogeneous nucleation. In classic nucleation theory, the value of ΔG^* depends on the assumptions of the nuclei shape [136, 137, 138]. We assume spherical nuclei that project as circles onto the 2D domain. This hybrid approach allows use of experimentally known parameters to calculate ΔG^* for 3D nucleation while still allowing the model to remain computationally tractable with 2D grain growth kinetics. Following the spherical nuclei assumption, Eq. 2.11 yields,

$$\Delta G^* = \frac{16}{3}\pi \frac{(\sigma_{\mathrm{p}})^3}{(H_{\mathrm{L}}\frac{\Delta T}{T_{\mathrm{m}}})^2}, \tag{2.11}$$

where σ_{p} is the solid-liquid interfacial energy, H_{L} is the latent heat, and T_{m} is the alloy melting point. ΔT is the extent of undercooling, $\Delta T = T_{\mathrm{m}} - T$.

Nucleation events are modeled as a stochastic process to model nuclei development in a random manner governed by the local nucleation rate [137]. The nucleation rate in Eq. 2.9 is used to inform a Poisson distribution probability, P_{nuc}, of a single nucleus attempting to form inside a cell of the phase-field modeling domain over a finite nucleation time step, Δt_{nuc}. Assuming the likelihood of formation of more than one nucleus at any instant of time is small yields,

$$P_{\mathrm{nuc}} = 1.0 - \exp(-J^* \Delta x \Delta y \Delta t_{\mathrm{nuc}}), \tag{2.12}$$

where the exponential term represents the probability of no nucleation occurring in any cell, and Δx and Δy are the mesh sizes [137]. If there is already a grain, nucleus, or particle at the attempted location the nucleus will not form. Fig. A.2 shows the temperature dependent nucleation rate curve assuming $N_0 = 1$ (Eq. 2.9). When the density of nucleation sites, N_{sites}, changes by an order of magnitude the nucleation probability also changes very close to an order of magnitude. To reduce the computational cost, nucleation is only attempted every 50 timesteps of the phase-field (order parameter) model, i.e., $\Delta t_{\mathrm{nuc}} = 50\Delta t$. Because of the stochastic nature of nucleation (Eq. 2.12), and therefore microstructure evolution, every simulation is run 3 times to quantify mean and standard deviation of model outputs (see section 2.2.6 for details of computation time).

2.2.5 Model Parameters

Stainless steel 316L (SS316L) with 25 nm radius TiB_2 nanoparticles, is chosen as a model material due to its widespread use in additive manufacturing processes and available mod-

eling input parameters from prior implementation in phase-field models [34, 7]. Wang et al. [7] studied a similar SS316L system with TiB_2 nanoparticles and therefore we adopted modeling parameters in Eqs. 2.1-2.8 from this study, (Table 2.1). The reference model by Wang et al. is 3D, but the reported model parameters are chosen due to their ability to match experimental results and their stability in our 2D simulations. While these selected parameters are based on experimental data and material-specific, these are tunable to be applicable for other materials of interest. Moreover, the focus of this investigation is to quantify and understand general results/trends rather than probing a specific nanoparticle and metal alloy composite. The unique contribution of our work beyond the reference model, is to explore the impact of nucleation rate, area fraction, and particle clustering on microstructure evolution [7]. The values of D_0 and grain boundary width, l_g, are adjusted to obtain reasonable and stable results [34, 7]. In real systems, l_g is typically on the order of 1 nm, but in prior work l_g is assumed to be multiple orders of magnitude larger to allow the spatial resolution to remain computationally tractable [34, 44]. Different assumptions about D_0 and l_g may change the physical time of the simulations, but the same trends are expected for the simulated microstructures.

2.2.6 Simulation Procedure

All simulations are performed in PRISMS-PF (Fig. 2.1) with a maximum of 16,384 elements and a mesh size of $\Delta x = \Delta y = 39$ nm [43]. The code used in the study is open-source and available for use on Github [109]. To reduce computational intensity while still avoiding artificial grain merging, the grain remapping algorithm in PRISMS-PF is deployed (see Note 3 in Appendix A) [43, 138]. Parallelized simulations are performed on a high-performance computing cluster (Great Lakes, CentOS 7) using 36 cores (2x 3.0 GHz Intel Xeon Gold 6154, 180 GB) with the longest 2D simulations taking a maximum of an hour. A reference case of the random distribution of nanoparticles with an area fraction of 0.05, and with a nucleation site density of N_0 (standard deviation, $s_{dz} = 3.2\%$) is used in discussing impact of parameter selection. Details of grain analysis and pinning fraction analysis are included in Note 2 in Appendix A.

Boundary and Initial Conditions: Neumann boundary conditions are modeled for the order parameters on all the boundaries (Fig. 2.1a). All the order parameters are initialized with values of 0 with nanoparticles loaded into fixed positions in the liquid domain.

Prior heat transfer simulations for SLM processes indicate transient cooling rates of $10^5 - 10^6$ K/s and spatial temperature gradients of $10^5 - 10^7$ K/m [22, 7]. We assume an intermediate cooling rate of 5×10^5 K/s, and a spatial temperature gradient of 10^5 K/m

Table 2.1: Model parameters, their baseline values and ranges explored in the phase-field simulations with relevant references

Category (Equations)	**Model parameter, symbol**	**Value [Units], Reference**
Ginzburg-Landau equation (Eqs. 2.3-2.8)	Grain Interaction Coefficient, γ	1.5, [44]
	Anistropy Coefficient, a_{k}	0.15, [7]
	Grain Boundary Width, l_{g}	110 [nm] (2.82 pixels), tunable, [139]
	Grain Boundary Pre-exponential, D_0	1.3×10^{-5} [m^4/(Js)], tunable, [7]
	Grain Boundary Energy, σ_{g}	0.385 [$\mathrm{J/m}^2$], [7]
	Activation Energy for Grain Boundary Mobility, Q_{g}	140 [kJ/mol], [44]
	Nucleation Free Energy Barrier, Δf_{g}	0.125, [44]
Nucleation (Eqs. 2.9-2.12)	Liquid/Solid Interfacial Energy, σ_{p}	0.385 [$\mathrm{J/m}^2$], [7]
	Activation Energy for Diffusion, Q_{D}	140 [kJ/mol], [7]
	Nuclei Contact Angle, θ	4°, tunable, [7]
	Latent Heat , H_{L}	2.1×10^9 [$\mathrm{J/m}^3$], [7]
	Melting Point of SS316L, T_{m}	1723 [K], [7]
	Nucleation site areal density, N_{sites}	$1.95 \times 10^6 - 1.95 \times 10^{12}$ [Nuclei/m^2], [7]
	Dimensionless nucleation sites, N_0	$N_{\mathrm{sites}}/1.95 \times 10^9$ [Nuclei/m^2]
Step Sizes	Mesh Size, $\Delta x = \Delta y$	39 nm
	Model Time Step, Δt	10 ns
	Nucleation Time Step, Δt_{nuc}	500 ns

across the build-direction (y-direction in Fig. 2.1a), which results in a 0.5 K difference across the domain (i.e., y-direction, in the 2D domain modeled). While varying the thermal gradient from 0 K/m, which is an isothermal domain, ($s_{\mathrm{dz}} = 1.6\%$) to 10^6 K/m ($s_{\mathrm{dz}} = 0.21\%$) has some impact on when different portions of the domain will nucleate on nanoparticles, the final microstructure still remains isotropic across all situations. We assume an isothermal gradient in the x-direction, which makes the domain symmetric. Initially, for the top surface, $y = 5$ μm, the temperature is T_{m} – 0.1 K, which is just below the melting point to induce solidification, and at $y = 0$ μm the initial temperature is T_{m} – 0.6 K (Fig. 2.1a).

Selection of Mesh Size and Time Step: The effects of altering the mesh size – Δx, Δy, and time step values – Δt , Δt_{nuc}, on the average grain size is compared against the reference case. Reducing the nucleation time step from 500 to 250 ns ($s_{\mathrm{dz}} = 0.43\%$), halving the model time step from 10 to 5 ns ($s_{\mathrm{dz}} = 1.3\%$), or reducing the mesh size from 39 to 19.5 nm ($s_{\mathrm{dz}} = 2.7\%$) all result in grain sizes within the reference standard deviation. The model parameter timestep, $\Delta t = 10$ ns, selected is the largest value possible while simulations

remain stable. Simulations are run for 20,000 timesteps (2000 μs) for all cases. While for some cases a few grain boundaries may continue to evolve after the end of the simulation, this additional evolution is minor enough to call 20,000 timesteps the steady-state grain size. While grid resolution may become an issue for high enough particle fractions, as the results will show the 10% area fraction runs fall in line with trends from lower area fractions indicating that our mesh size is sufficient to avoid detrimental effects from small grid spacings between particles.

2.3 Results and Discussion

Since this study considers 70 unique 2D cases, select combinations are shown to illustrate takeaways more clearly. Trends for other cases are also discussed with videos of select cases shown in the Chapter 2: Phase-Field Google Drive Folder. Videos are shown for the random, $\Phi_{np} = 0.01$ and $10^{-1}N_0$ case (Video S-1) and clustered, $\Phi_{np} = 0.01$ and $10^{3}N_0$ case (Video S-2).

2.3.1 Impact of Clustering and Nucleation Rate on Solidification

Fig. 2.2 shows effects of nanoparticle clustering and nucleation site density on the transient evolution of the number of grains and their microstructures from an initially molten domain with the substrate at the bottom edge of the domain. A representative nanoparticle area fraction of $\Phi_{np} = 0.05$ is compared against the particle-free case, i.e., $\Phi_{np} = 0$. Initially, only nanoparticles in the liquid melt are present (Fig. 2.2b,f). Then, grains heterogeneously nucleate off the nanoparticles and substrate. As the grains grow, they collide and interact with other grains and nanoparticles. Grain number versus time is shown for nucleation site densities of $0.1N_0$ (Fig. 2.2a) and $10N_0$ (Fig. 2.2e). 2D maps of the grain microstructures are shown for the clustered distribution of particles — $0.1N_0$ (Fig. 2.2b–d) and $10N_0$ (Fig. 2.2f–h). Similar trends are obtained for other area fractions.

For all cases modeled, there is an initial increase in the number of grains up to a maximum value beyond which it decreases (Fig. 2.2a,e). Through a competitive process, smaller grains tend to be consumed by larger grains resulting in grain coarsening [7]. After solidification is complete, grain coarsening continues to further reduce the grain number until a steady-state grain density, and equivalently, a grain size is attained, which occurs at about 2000 μs. Since the nanoparticles make up a larger nucleation surface area as compared the substrate wall, the grain density for the nanoparticle free cases is much lower (Fig. 2.2a). For a fixed nucleation rate, a larger peak and steady-state number of grains is obtained for the random

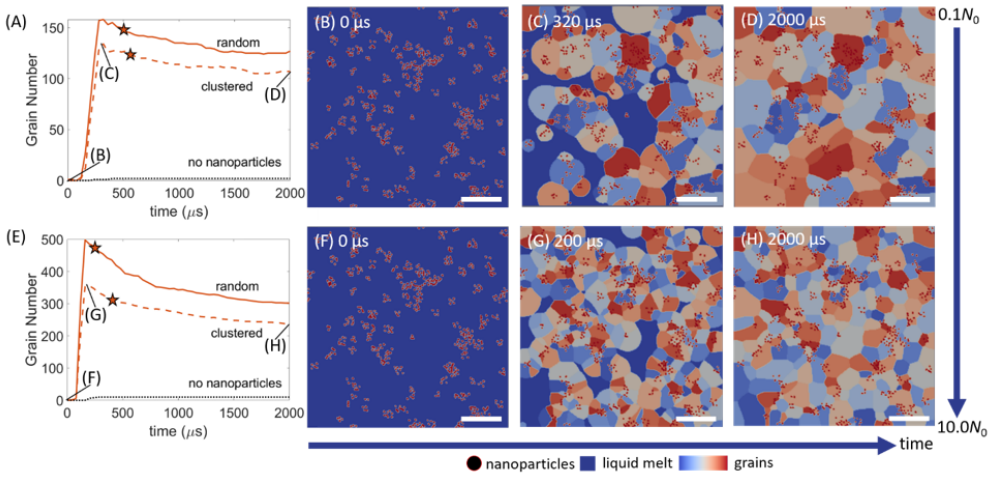


Figure 2.2: Time evolution of grain microstructure for random and clustered distributions of nanoparticles with an area fraction of $\Phi_{np} = 0.05$ and for the case of no nanoparticles for nucleation site densities of (a–d) $0.1N_0$ and (e–h) $10N_0$. Stars in (a) and (e) represent the instance when solidification is complete. Snapshots of microstructures for the clustered distribution of nanoparticles at the (b,f) start of simulation, (c,g) peak number of grains, and the (d,h) final microstructure. Substrate is present at the bottom of the 2D domain and not shown in the figure. $N_0 = 1$ corresponds to 1.95×10^9 Nuclei/m^2. Scale bars are 1 μm.

as compared to the clustered distribution of particles. As grains nucleate within a cluster zone, they quickly cover up nearby nanoparticles and therefore reduce the effective number of nucleation sites available, resulting in a lower number of grains. Nucleation ends with site saturation once all available nucleation surface areas are covered in nuclei/grains. The final number of grains increases at a slower rate with site density as compared to the peak value due to grain coarsening.

Fig. 2.3 provides further insight into the effects of nanoparticle distributions and nucleation site density on the final grain microstructures for an area fraction of 0.01 and for nucleation site densities of $0.1N_0$ and $10N_0$. When comparing the impact of increasing site density on microstructure for both the random (Fig. 2.3a,d) and clustered (Fig. 2.3b,e) cases, a larger site density results in a more refined microstructure as expected. However, while the random distribution case has a spatially homogeneous distribution of grains, the clustered case is marked by regions of small grains and regions of large grains. Smaller grains tend to appear near regions with high cluster concentrations, and larger grains grow away from clusters into particle free regions. Fig. A.3 provides a more quantitative analysis of the impact of area fraction, nucleation site density, and clustering on grain size distribution.

For comparison, final microstructures are shown for the extreme cases with no nanoparticles (Fig. 2.3c) and one single large cluster with an area fraction of 0.01 and $10N_0$ (Fig. 2.3f).

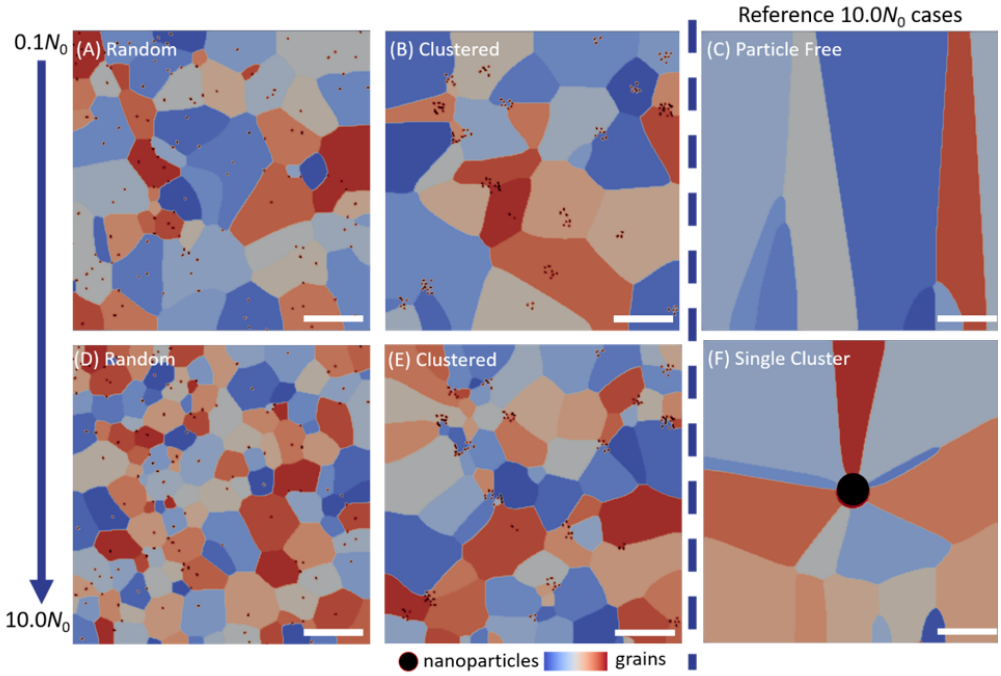


Figure 2.3: Final grain microstructures after 2000 μs for select cases of 0.01 area fraction for random distributions with (a) $0.1N_0$, (d) $10N_0$; for clustered distributions with (b) $0.1N_0$, (e) $10N_0$. Reference cases shown with $10N_0$ for (c) particle free case and (f) with single large cluster of nanoparticles with 0.01 area fraction. Substrate is present at the bottom of the 2D domain and not shown in the figure. $N_0 = 1$ corresponds to 1.95×10^9 Nuclei/m^2. Scale bars are 1 μm.

For the particle free case (Fig. 2.3c), since all grains must nucleate from the substrate, long, columnar grains grow with smaller, shorter grains slowly being consumed by longer grains. In contrast, Fig. 2.3a,b,d,e demonstrate that even 0.01 area fraction of particles are effective in supporting the columnar-to-equiaxed grain transition [34]. The single cluster case, representing the most severe degree of clustering possible, shows grains grow in a sunburst style shape away from the cluster in the center of the domain (Fig. 2.3f).

2.3.2 Nucleation Rate and Clustering Influence Grain Size

Fig. 2.4 shows the steady-state average grain size for modeled combinations of the nanoparticle concentrations ($\Phi_{\text{np}} = 0.01, 0.05, 0.10$), spatial distributions (random and clustered), and nucleation site densities ($10^{-3}N_0 - 10^3N_0$). There is a relatively larger stochastic uncertainty in the average grain size for the low nucleation site densities. This is attributed to fewer, one or two dozen, grains that are nucleated as compared to hundreds of grains for larger nucleation site densities. Due to the large standard deviation for the 1% area frac-

tion cases, two additional simulations were run for both these random and clustered cases. The trend in standard deviation fluctuates with the number of trials decreasing slightly for the random trials and being erratic for the clustered case. However, the mean grain size varied by less than the standard deviation for all nucleation rates giving confidence in our reported three trial results, while indicating the deviations stem from the stochastic nature of modeling nucleation. For all spatial distributions and site densities, when area fraction increases, more particles nucleate new grains and pin grain boundaries resulting in smaller final grain sizes. Clustering has a larger impact on increasing the final grain size relative to an ideal, random distribution when the area fraction is small. For example, for $\Phi_{\mathrm{np}} = 0.01$ and $10^{-1}N_0$, clustering results in a 40% larger grain size than for the random distribution case. However, for a larger nanoparticle concentration of $\Phi_{\mathrm{np}} = 0.1$, the clustered and random distributions converge and lead to nearly the same average grain size. At larger area fractions, many distinct clusters are present and nearly approximate a random distribution, resulting in similar grain sizes for both scenarios. This indicates that controlling processing/manufacturing parameters to limit clustering of nanoparticles is more important when nanoparticle concentration is small ($< 5\%$ by area).

At low nucleation site densities ($10^{-3}N_0 - 10N_0$), increases in site density (and corresponding nucleation rate) result in a significant decrease in final grain size for both random and clustered distributions. While grain size still decreases, increases in site density beyond $10N_0$ have diminishing impact on reducing the final grain size. This site saturation phenomenon is multifaceted and is discussed in more detail subsequently.

2.3.3 Smith-Zener Grain Size Depends on Nucleation Rate

The results of Fig. 2.4 can be analyzed through the Smith-Zener Equation. Traditionally, the limiting average grain diameter, d_{z}, of nanoparticle reinforced alloys is given by the generic Smith-Zener diameter (Eq. 2.13),

$$d_{\mathrm{z}} = 2r_{\mathrm{p}}\frac{K}{(\Phi_{\mathrm{np}})^m} \tag{2.13}$$

where d_{z} represents an estimate for grain size, and r_{p} is the nanoparticle radius [123]. Eq. 2.13 can be applied to both 2D and 3D simulations/experiments [42]. For the classic Smith-Zener equation, $K = 4/3$ and $m = 1$, but these values typically overestimate grain size [42]. Physically, the constant K is influenced by the particle-grain pinning force [42, 140], and m describes how changes in area fraction influence grain size [3]. Fig. 2.5a shows the predicted grain size versus area fraction for bounding cases of $10^{-3}N_0$ and $10^{3}N_0$ for random and clustered cases. Two reference cases are shown in Fig. 2.5a, including the classic Smith-

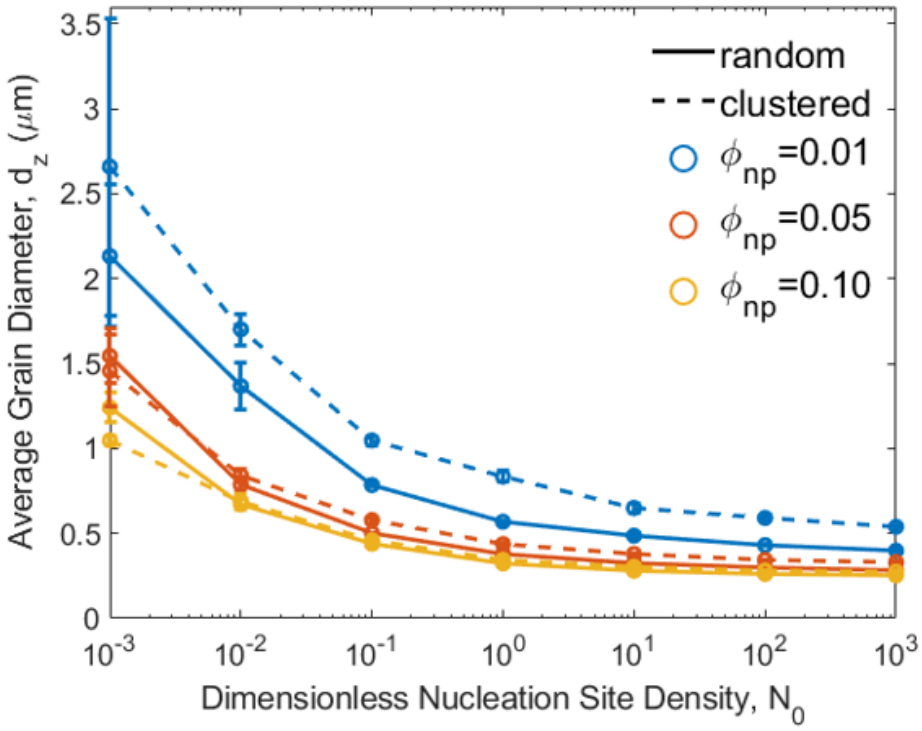


Figure 2.4: Steady-state average grain size for random and clustered distributions as a function of nucleation site density, N_0, for various area fractions, Φ_{np}. Points shown are averages of 3 simulations per nucleation site density modeled and the error bars represent standard deviation. $N_0 = 1$ corresponds to 1.95×10^9 Nuclei/m^2.

Zener Equation ($K = 4/3$ and $m = 1$) [2], and Srolovitz et al. curve, which is from 2D Monte Carlo simulations of grain growth with a random distribution of pinning nanoparticles ($K = 1.7$ and $m = 1/2$) [61]. These results highlight the wide range in predicted grain sizes from literature. While our predicted grain size can approach the classic Smith-Zener Equation or Srolovitz et al. curve depending on nucleation rate, the slopes of the grain size curves vary indicating different pinning dynamics than for these reference cases. This again reinforces the outsized role nucleation during solidification has on controlling grain size. Therefore, care must be taken when drawing conclusions between models that may not include effects of nucleation rate.

Fig. 2.5b,c shows the best-fit values with corresponding error bars for K and m as a function of spatial distributions and nucleation site densities using the data from Fig. 2.4. Consistent with the clustered grain size being more sensitive to area fraction (Fig. 2.5a), for each N_0 modeled, the m values of the clustered (0.295–0.443) are higher than for the random distribution (0.188–0.288). For both distributions the uncertainty in fit decreases with increasing nucleation site density, most likely due to less uncertainty in average grain

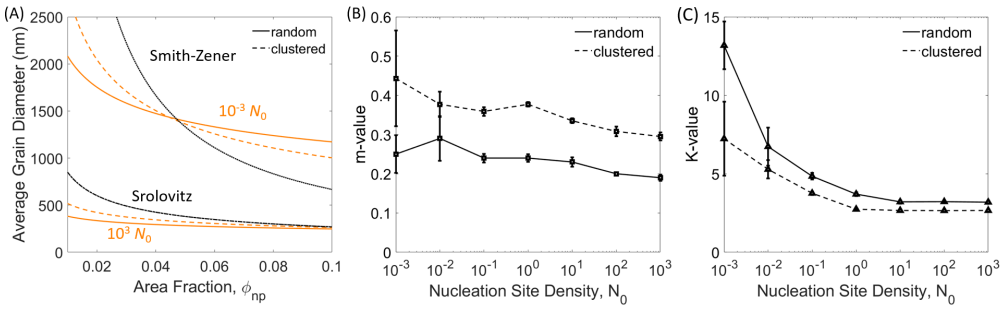


Figure 2.5: Modified Smith-Zener Diameters for random and clustered distributions. (a) Grain diameter versus area fraction for nucleation site densities of $10^{-3}N_0$ and $10^{3}N_0$. All other N_0 will fit between these two extremes. Reference fits are from the original Smith-Zener Equation as recorded by Smith [2] and Srolovitz et al. [3]. (b,c) Impact of nucleation site density along with error bars across three trials on m and K, which are fitting constants in the Smith-Zener Equation (Eq. 2.13). $N_0 = 1$ corresponds to 1.95×10^9 Nuclei/m^2.

size. The m values are relatively constant with a slight decrease as nucleation site density increases. In contrast, the K value decreases, 4.7 times for the random and 3.0 times for the clustered cases, when site density increases from $10^{-3}N_0$ to $10N_0$. Beyond $10N_0$, K values level off. Table 2.2 presents modified Smith-Zener Equations that account for nucleation site density dependency of K while assuming a constant, average m value for each distribution. Most previous 2D simulations, which ignore heterogeneous nucleation during solidification, have m values around 0.5, whereas our study has lower m values between 0.195–0.407 [42]. This suggests nanoparticles serving as nucleation sites may lower the m value with a reduced effect for clustered cases.

Although we varied the nucleation site density, N_0, to impact the nucleation rate, J^*, any combination of interfacial energy, contact angle, thermal history, undercooling, etc. could have been varied to impact J^*. Therefore, more generally, our results predict that grain size is inversely proportional with nucleation rate as $d_z \sim 1/(J^{*0.15})$. This suggests that an effective strategy to reduce grain size enhancing strength, in addition to reducing nanoparticle size and increasing volume fraction, is to use nanoparticles with low contact angles and/or generate thermal profiles during manufacturing that maximize the nucleation rate according to Eq. 2.9.

Table 2.2: Nucleation rate dependent grain size predictions for random and clustered distributions fitted for nucleation site densities ($10^{-3}N_0 - 10^3N_0$) and area fractions (Φ_{np} = 0.01–0.10). $N_0 = 1$ corresponds to 1.95×10^9 Nuclei/m^2.

Nanoparticle Distribution	**Best Fit Equations**	**General Relationship**	R^2
Random	$d_z = 2r_p \frac{K}{\Phi_{np}^{0.25}}$, $K = \frac{5.0}{N_0^{0.15}} = \frac{124.0 \text{ nuclei/m}^2}{(N_{sites})^{0.15}}$	$d_z \sim 1/(J^*)^{0.15}$	0.972
Clustered	$d_z = 2r_p \frac{K}{\Phi_{np}^{0.33}}$, $K = \frac{4.0}{N_0^{0.15}} = \frac{99.0 \text{ nuclei/m}^2}{(N_{sites})^{0.15}}$		0.977

2.4 Grain Size Saturation is Explained by Particle Pinning Fraction

Since nanoparticles can only effectively prevent grain growth when they are on grain boundaries, the saturation in grain size for $> 10N_0$ (Fig. 2.5a) is explained by quantifying the fraction of nanoparticles on grain boundaries, Γ_{tot}.

Based on the classic Smith-Zener equation (Eq. 2.13), which assumes no correlation between nanoparticle and grain boundary locations, the total fraction of nanoparticles pinned on grain boundaries can be predicted using Eq. 2.14 [121, 141]

$$\Gamma_{tot} = (9/4)\Phi_{np}. \tag{2.14}$$

For area fractions of 0.01, 0.05, and 0.10, Eq. 2.14 predicts 2.25%, 11.3%, and 22.5%, respectively for the fraction of nanoparticles on grains. However, as Fig. 2.6 shows, even for the smallest nucleation site density modeled ($10^{-3}N_0$), the actual fraction pinned is much larger, 8–40%, than predicted from Smith-Zener's equation indicating a strong preference of nanoparticles on grain boundaries. For all particle distributions and area fractions, as the nucleation site density increases ($10^{-3}N_0 - 10N_0$), the pinning fraction increases rapidly initially and asymptotes ($10^2 - 10^3N_0$) towards pinned fractions in the range of 0.85–0.90. Published phase-field and Monte Carlo studies of homogeneous nucleation also found similar trends. For these studies, when the initial grain number increases, analogous in our study to increasing the nucleation rate, the pinning fraction increases before reaching a saturation value of 0.8-0.85 for 2D cases [44, 141]. Experimental studies of a Ni-based superalloy also found a preference of nanoparticles at the grain boundaries again reaching a saturation value between 0.8–0.9 and yielded the smallest grain sizes [142].

While the total pinning fraction is a useful metric, Γ_{tot} can be further divided into particles that only pin two grains, Γ_2, such as along a plain section of grain boundary, and

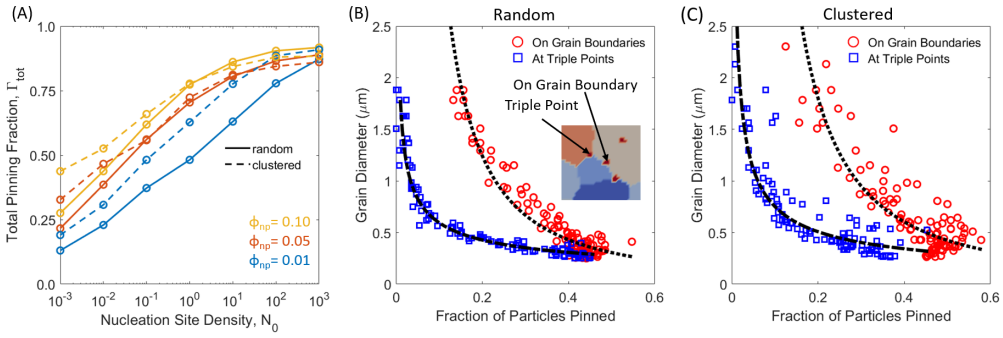


Figure 2.6: (a) Impact of nucleation site density, N_0, on fraction of particles pinning grain boundaries, Γ_{tot}, for select area fractions of 0.01, 0.05, 0.10. (b–c) Impact of pinning fraction, separated by on grain boundary, Γ_2, and at triple point fractions, Γ_3, on final grain diameter with best fit curves for the three trial average for all area fractions. (b) All random cases: $d_z = 2\times 2.11 r_p/(\Gamma_2^{1.534})$, $R^2 = 0.868$ and $d_z = 2\times 3.97 r_p/(\Gamma_3^{0.477})$, $R^2 = 0.943$. (c) all clustered cases: $d_z = 2 \times 2.84 r_p/(\Gamma_2^{1.58})$, $R^2 = 0.721$ and $d_z = 2 \times 4.07 r_p/(\Gamma_3^{0.568})$, $R^2 = 0.820$. $N_0 = 1$ corresponds to 1.95×10^9 Nuclei/m^2.

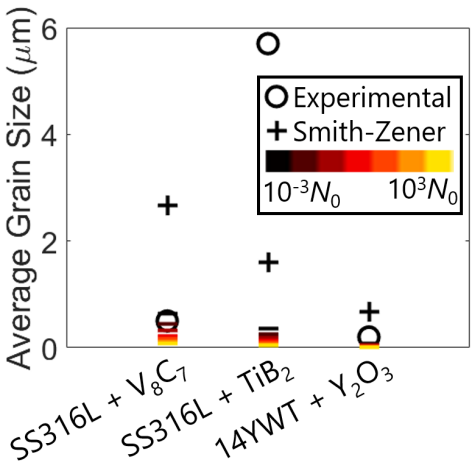
particles that pin three grains at a triple point, Γ_3 (Fig. 2.6b). Compared to previous 2D Monte Carlo studies of grain growth, which developed grain size functions dependent on both pinning and area fraction, we found that for our range of area fractions we were able to adequately predict grain size even without considering area fraction [48, 143]. Fig. 2.6c extends this analysis to a clustered distribution of particles. While the clustered case again shows better agreement for the triple point ($R^2 = 0.820$) versus on grain boundary fit ($R^2 = 0.721$), these fits are not as good as the random cases, particularly at higher fractions pinned. The pinning fraction required to achieve a fixed grain size is larger for the clustered compared to the random distributions of the nanoparticles, which is likely due to clustering allowing free grain growth away from cluster centers (Fig. 2.3e). The spatial distribution of the nanoparticles is an additional factor that can influence grain size even with the pinning fraction being a dominant factor. Overall, the strong correlation predicted between pinning fraction, especially triple point fraction in 2D, and grain size calls for researchers to report/extract pinning fraction data from microstructural characterization, in addition to grain size distributions, to determine if the nanoparticles are effective in reducing grain size, which can strengthen alloys.

2.4.1 Interpreting Experimental Data with Model Predictions

While comprehensive 3D simulations are needed to quantitatively compare with experimental data, the importance of including nucleation rate in grain size predictions revealed from our 2D simulations can still help interpret 3D experiments. Fig. 2.7(a) shows comparisons of

experimentally reported grain sizes and nanoparticle volume fractions for select alloys with the classic Smith-Zener model (Eq. 2.13) and the predicted sizes (Table 2.2) corresponding to the nucleation rates considered in this study. We assumed a random distribution of nanoparticles for the sake of generality across alloys. The table in Fig. 2.7b lists the experimental nanoparticle radius and volume fraction.

(A)



(B)

Ferrous Alloy, Reference	*Nanoparticle Radius (nm)*	*Volume Fraction, Φ_{np}*
SLM SS316L with V_8C_7 [66]	~50	~0.04
SLM SS316L with TiB_2 [7]	30	0.05
MA 14YWT with Y_2O_3[8]	2	~0.004

Figure 2.7: (a) Predicted vs Experimental Grain Sizes reported in the literature for select nanoparticle reinforced alloys. Nucleation rate dependent grain size predictions come from the random distribution case of Table 2.2. (b) Table showing additional pertinent alloy information (Note: reference numbers are from paper, see thesis text for thesis reference numbers). $N_0 = 1$ corresponds to 1.95×10^9 Nuclei/m^2.

The classic Smith-Zener Equation is inconsistent at predicting the experimental results overpredicting grain size for the V_8C_7 and Y_2O_3 reinforced alloys and underpredicting for the TiB_2 reinforced alloy [25, 26, 144]. For the SLM SS316L alloy reinforced with V_8C_7 nanoparticles, our predictions match the results for a nucleation density of $10^{-2}N_0$ (1.95×10^7 nuclei/m^2). Although the model was developed for rapid solidification processes, the grain size of mechanically alloyed (MA) ferrous 14YWT reinforced with Y_2O_3 particles approaches the $10^{-3}N_0$ (1.95×10^6 nuclei/m^2) value showing that accounting for nucleation rate can improve Smith-Zener grain size predictions. For the TiB_2 reinforced SS316L, both the classic Smith-Zener Equation and nucleation rates considered predict a much smaller grain size than is observed in ref. [25]. This may be due to the limited ability of the TiB_2 nanoparticles to pin grain boundaries, which depends on the nanoparticle spatial distribution and lattice mismatch and coherency between SS316L and TiB_2 [145]. Therefore, the assumption of ideal particle pinning in our model may not be reasonable for cases where the measured grain size exceeds the classic Smith-Zener limit.

2.4.2 Scope and Future Extension of Model

While the scope of our study is largely limited to 2D, previous studies have shown that for a given area/volume fraction, 3D simulations generally tend to have a lower pinning force and lower pinning fraction than for similar 2D simulations [122, 49, 144, 146]. This factor additionally affects the comparisons made in Section 2.4.1 between model predictions and measured data. The difference in predictions for grain size between 2D and 3D simulations varies based on the particle concentration and initial conditions [42, 141]. Preliminary 3D simulations were performed in a 2.5 μm $\times$ 2.5 μm $\times$ 0.3125 μm domain and with a random distribution of nanoparticles and $\Phi_{\mathrm{np}} = 0.017$ by applying the following 3 nucleation site densities: 5×10^{12}, 5×10^{13}, and 5×10^{14} nuclei/m^3 (Fig. A.4 and Table A.1). Only 1 run of each case was conducted. These 3D results predict $d_{\mathrm{z}} \sim 1/(J^{*0.16})$, with the nucleation rate exponent agreeing reasonably well with results from 2D simulations. While this trend is intact, the absolute magnitudes of the grain size and the pinning fraction vary between 2D and 3D. Compared to 2D, these 3D simulations had a larger fraction of particles on grain boundaries and a reduced triple point fraction showing the difference in pinning dynamics from 2D to 3D [147]. This may also in part stem from the difficulty of exactly matching the number of nucleation events between the 2D and the 3D simulations, and additionally due to the thin film nature of the 3D domain [68]. More comprehensive 3D simulations are needed to further explore the causal factors for these differences, but this is outside the scope of the current work. A secondary aim of this study revealed that particle clustering can play a large role in final microstructure for a static bed of particles. A future extension would be to incorporate dynamic motion of nanoparticles during solidification into the model [117, 50, 51, 148].

2.5 Conclusion

In this study, we develop and apply a phase-field model to simulate alloy solidification and grain growth with a dispersion of nanoparticles, motivated by their potential to improve yield strength. A direct advancement of this model is an explicit investigation of the effects of nucleation rate/site density ($1.95\times10^6-1.95\times10^{12}$ nuclei/m^2), area fraction (0.01–0.10), and nanoparticle distribution – random and clustered spatial distributions, and on grain growth dynamics. The model incorporates effects of nanoparticles on heterogeneous nucleation and grain boundary pinning. While the classic Smith-Zener Equation ignores the impact of nucleation rate, we developed a modified Smith-Zener Equation to predict grain size as a function of nucleation rate. Specifically, our results demonstrate that grain size is inversely

related to nucleation rate as $d_z \sim 1/(J^{*0.15})$ for both random and clustered 2D distributions. This general trend should extend into 3D although additional simulations are needed to determine the impact on the value of the exponent. Grain size reduces 3–5 times across the nucleation rates considered. This suggests choosing alloy-nanoparticle pairings that can increase nucleation rate, such as by decreasing interfacial energy/contact angle, can play a large role in improving alloy strength. Our predictions also underscore that grain size, across various area fractions and nucleation rates, is primarily a function of the fraction of particles located/pinned on grain boundary triple points for 2D. We also show for low area fractions, $\sim$0.01, clustering of nanoparticles results in 15-45% larger grain diameters than the random case. As the area fraction increases, the random and clustered grain sizes converge showing that clustering's impact is more pronounced at lower area/volume fractions of nanoparticles. Overall, this study provides a new alloy solidification model, and reveals the impact of particle clustering and nucleation rate on grain size. Model results offer valuable insight to guide the development of next generation, stronger nanoparticle reinforced alloys.

CHAPTER 3

Process Mapping for Kanthal A1 and Kanthal KAPM FeCrAl Alloys using Synchrotron Imaging

Adapted in part from a manuscript under preparation: Kinzer, B., Jobes, D., Rubio-Ejchel, D., Clark, S., Fezzaa, K., Gordon, V., Bala Chandran, R., "*Process Mapping for Kanthal A1 and Kanthal KAPM FeCrAl Alloys using Synchrotron Imaging.*"

3.1 Introduction

FeCrAl alloys are a promising material class offering excellent corrosion and oxidation resistance at elevated temperatures up to 1400°C [149, 31, 14, 40]. By leveraging the protective Al_2O_3 oxidation layer that forms during operation, they are used in a variety of industries such as heat exchangers for power plants and furnace heating elements [31, 40, 29]. Refactory and oxide particles can be added to FeCrAl alloys in a process known as oxide dispersion strengthening (ODS) to reduce the growth rate of oxidation as well as improve high temperature yield and creep strength by slowing down grain growth [149, 27]. As with many alloys, there is a growing interest to use additive manufacturing (AM) to produce FeCrAl parts including ODS reinforced versions with complex, near-net-shape geometries [20, 40, 149]. One of the most popular AM processes is laser powder bed fusion (LPBF), where a laser selectively melts a layer of metallic powders [20]. The part is lowered and a new layer of powders is deposited and selectively melted building up the part layer by layer. While promising, the development of a new LPBF alloy can be time consuming as factors including laser spot size, hatch spacing, layer thickness, laser power, and laser speed must be optimized [20, 23]. This optimization process comes down to choosing processing parameters that will result in stable melt pool geometries [55, 54]. At too high of laser powers and/or low of laser speeds the powder absorbs sufficient energy to not only vaporize the metal but have it drill into

the metal due to recoil pressure. This results in deep and narrow vapor pockets known as keyholes that can worsen surface finish and result in keyhole porosity defects that lower the strength of the alloys [55, 56]. At the other end, too low of laser powers and/or too high of laser speeds results in melt pools that are not sufficiently large to overlap resulting in a lack of fusion regime where gaps between scan tracks may result in unmelted powders and porosity leading to weak spots [55]. While post-mortem cross-section analysis can offer some guidance on melt pool operating regime [55], the lack of real time tracking makes this tedious and difficult to ascribe dynamic mechanisms too.

In-situ synchrotron dynamic X-ray radiographpy (DXR) is a powerful technique that can track melt pool and vapor depression morphologies during LPBF processes offering high spatial resolution (2 μm) and excellent temporal resolution (50-400 kHz) [150]. Synchrotron imaging has been used to compare melt pool processing maps between base alloys and their ODS counterparts revealing that when large enough volume fractions ($\geq$ 1 wt%) of nano-sized ODS particles ($<$ 100 nm) are added to the alloy, they can significantly increase the melt pool viscosity leading to more stable keyholes and a deeper penetration depth by altering the inclination angle, which changes the effective absorptivity of the alloy [60, 59, 56]. However, high concentrations of nanoparticles can increase material cost and potentially impact manufacture-ability, so there remains a need to use DXR to understand the impact of ODS particles at lower concentrations ($<$ 0.5 wt%). To address this gap, we conducted DXR studies for two of the most commercially popular FeCrAl alloys, Kanthal A1 (particle free) and Kanthal APM (ODS reinforced). While exact details for the Kanthal APM ODS particles are not published by Kanthal, a prior study suggests roughly 0.1 wt% of ZrO_2 particles on the order of 100-500 nm are present [151]. Even at this low concentration the particles can increase creep strength over four times at high temperatures (1000°C) [29, 30], and offer improved corrosion resistance [31]. The main purposes of this study are to 1) establish melt pool processing maps (laser power versus speed) for Kanthal A1 and the reinforced Kanthal APM FeCrAl alloys to offer an optimal starting LPBF parameters to aid in alloy development, 2) understand what/if any impact the low ODS particle concentration has on melt pool morphologies to aid in development of additively manufactured reinforced FeCrAl alloys, and 3) compare the observed keyhole and lack-of-fusion regimes to understand where the well established Rosenthal conduction model can be applied for similar FeCrAl alloys [57].

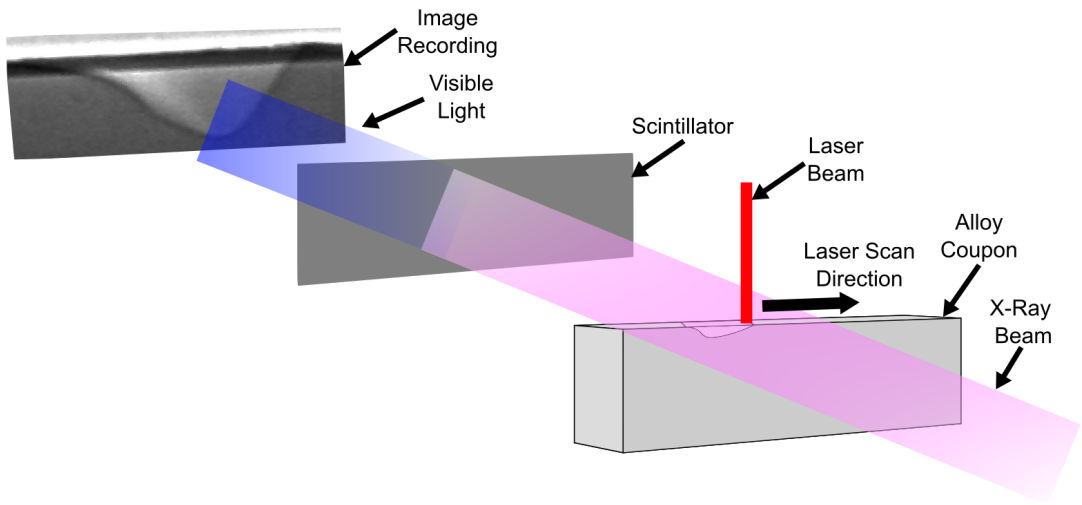


Figure 3.1: Experimental Setup of the *In-situ* Synchrotron Dynamic X-ray Radiography Setup

3.2 Material and Methods

Samples of commercially manufactured Kanthal A1 and Kanthal APM were sourced form Hi-Temp Products (CT, USA). Both alloys have a composition of Fe-5.8wt%Al-22wt%Cr with trace amounts of C, Si, and Mn. The Kanthal APM also contains roughly 0.1 wt% of nanoparticles, likely ZrO_2 [151]. No powder layers were used as prior work suggests the absence of a powder layer during LPBF only has has a second order impact on melt pool geometries [152, 55]. Due to the easier DXR setup, solid metal coupons were used instead of powders. Wire EDM was used to create specimens of 40 mm long, 3 mm tall, and 0.4 mm thick. An auto-polisher was used to polish the specimen down, initially using increasingly fine grades of SiC grinding paper finishing with 1200 grit. A 3 μm diamond solution was using for the final polish to ensure more than adequate surface finish for DXR imaging [55]. *In-situ* DXR experiments were conducted at the 32-ID-B beamline at the Advanced Photon Source at Argonne National Laboratory. High energy X-ray was used to illuminate a cross-sectional area for each alloy under conditions representing LPBF (Fig. 3.1). The density differences between the solid, liquid, and vapor phases allowed for sufficient contrast to track the vapor depressions. Incoming X-rays transmitting through the sample thickness were collected on a scintillator and transformed to visible light images that were captured using a high-speed camera placed behind at a frame rate of 50 kHz and spatial resolution of 2 μm. A ytterbium fiber scanning laser with wavelength of 1070 nm, laser spot size diameter of 80 μm, and Gaussian beam profile was used to provide laser power (P) between $0 < P < 450$ W. A galvo scanner enabled the laser to scan across the sample surface at speeds between

$0 < V < 1.4$ m/s. All experiments were performed under 1 atm Ar protective gas and with no powder layer on top. Melt pool and vapor depression depth and width measurements was undertaken in imageJ. An imageJ script was written to divide the difference in pixels between subsequent frames. This enhances the contrast and increases visibility of the vapor depression and melt pool to allow melt pool width to also be measured. Although vapor depression depths are measured, since these are within about 10% of melt pool depth, we refer to vapor depression and melt pool depth interchangeably in this chapter.

Rosenthal Model: The Rosenthal Model, which is a conduction heat transfer model that assumes the laser moves as a point heat source into a semi-infinite medium was used as a first approximation to predict melt pool morphology [58]. We assume a spherical coordinate system of $R^2 = z^2 + r^2$, where z is along the laser scan direction and r is into the depth of the alloy. Assuming the alloy is at room temperature, T_0, sufficiently far away from the laser source ($R = \infty$) and that the laser power, P, at the alloy surface is given by Eq. 3.1 [58]

$$P = \left[\left(2\pi R^2\right) \left(-k \frac{\partial T}{\partial R}\right) \right]_{\mathrm{R} \to 0} \tag{3.1}$$

where k is alloy thermal conductivity. By applying these boundary conditions and assuming a large Peclet Number $Pe > 5$ (see Poirier et al. for more details [58]) we arrive at Eq. 3.2

$$P \simeq \frac{\pi \rho e C_{\mathrm{p}}}{2} (T - T_0) V r^2 \tag{3.2}$$

where ρ is the alloy density, e is the base of natural log, and C_{p} is the alloy specific heat. By substituting in the alloy melting point, T_{m}, as the temperature of interest, we find that at melt pool width, W, ($r = W$) is approximated by eq. 3.3.

$$W = \sqrt{\frac{2P}{\pi \rho e C_{\mathrm{p}} V (T_{\mathrm{m}} - T_0)}} \tag{3.3}$$

Since the Rosenthal model only accounts for conduction, it assumes that melt pool depth, D, is half the melt pool width, $W = 2D$. Lack of fusion occurs when there is not sufficient overlap between melt pool scans, and can be predicted when the following relationship is satisfied (Eq. 3.4)

$$(\frac{H}{W})^2 + (\frac{L}{D})^2 \leq 1 \tag{3.4}$$

where H is the hatch spacing and L is the layer thickness. To predict the onset of keyholing the following normalized enthalpy relationship can be used (Eq. 3.5) [57]

$$\frac{\Delta H}{h_{(\mathrm{s})}} = \frac{AP}{\pi h_{\mathrm{s}} \sqrt{\alpha V a^3}} > \frac{\pi T_{\mathrm{vap}}}{T_{\mathrm{m}}} \tag{3.5}$$

where ΔH is the specific enthalpy and $h_{\mathrm{s}} = \rho C_{\mathrm{p}} T_{\mathrm{m}}$ is the enthalpy at melting. A is the laser absorptivity by the alloy, α is the thermal diffusivity, a is the laser spot size, and T_{vap} is the vaporization point. To generate the processing maps of this study, a hatch spacing of $H = 50$ μm and layer thickness of $L = 30$ μm was assumed although these can be varied for different LPBF setups. While Eq. 3.5 is used to predict keyholing, the onset of heyhole porosity can be predicted when melt pool depth is more than half the width, $D/W \geq 0.5$, which is measured from DXR images. Both the keyhole instability (Eq. 3.5) and the lack of fusion instability (Eq. 3.4) are checked. If neither condition is met, this indicates the processing window although slight operation into keyholing is also acceptable as long as no keyhole porosity occurs. The Rosenthal model assumes constant properties. We took the average reported properties at room temperature, with values and sources listed for the Kanthal alloys in Table 3.1. Since Kanthal A1 and Kanthal APM have the same base composition the same properties are used for each model. Kanthal does not publish an vaporization temperature, so this was estimated using the TCFE11 Steels/Fe-alloys package in Thermo-Calc 2023 [153]. The absorptivity of alloys during AM processing is complex, so for the sake of simplicity a constant absorptivity of 0.2 was assumed.

Table 3.1: Properties used for both the Kanthal A1 and Kanthal APM Rosenthal Model

Property	Value, Source
Melting Point, T_{melt}	1723 K ([29])
Ambient Temperature, T_0	293 K
Vaporization Point, T_{vap}	2963 K (Thermo-Calc)
Density, ρ	7100 kg/m^3 ([29])
Specific Heat, C_{p}	460 (J/(kg K)) ([29])
Thermal Conductivity, k	11 (W/(m K)) ([29])
Absorptivity, A	0.2 (assumed)
Thermal Diffusivity, α	3.380e-6 m^2/s ([29])

3.3 Results and Discussion

Figure 3.2 shows the processing map for the particle free Kanthal A1 across the wide range of laser powers and speeds tested. At low laser powers (100 W), Kanthal A1 operates in the lack of fusion regime marked by very small or non-exist vapor depressions. As laser power increases the melt pools deepen. With sufficiently low laser speeds and high laser

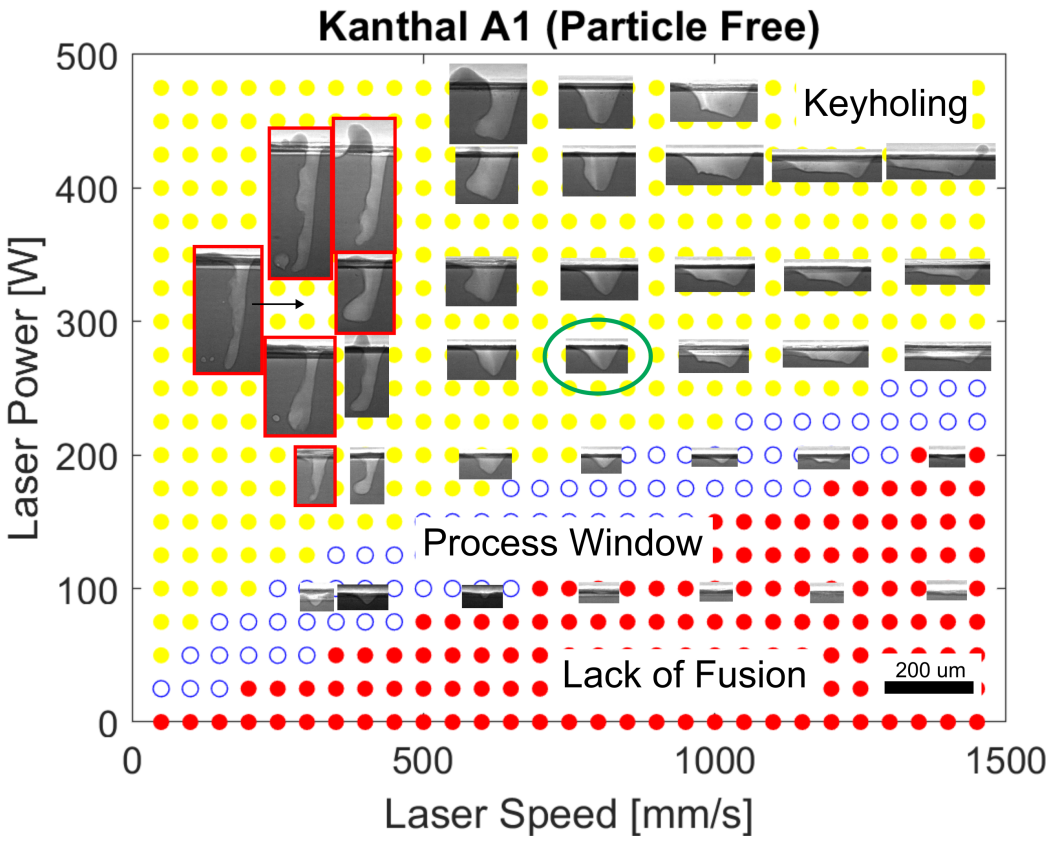


Figure 3.2: Laser Power vs Laser Speed Processing Map for Kanthal A1 overlaid with Rosenthal Model. The images bordered in red had observable keyhole porosity. The circled green case at 300 W and 800 mm/s was identified as the optimal condition. The dotted background colors represent melt pool regimes.

powers, deep keyholing leading to keyhole porosity is observed (red bordered images). Large amounts of splatter, which increases surface roughness, was also observed for these cases [59]. In general, the keyhole porosity cases were much more likely to meet the Rosenthal keyhole porosity criteria with melt pool depths more than half the melt pool width ($D/W \geq 0.5$). However, several cases had keyhole porosity but D/W ratios below 0.5 including 200 W, 350 mm/s ($D/W = 0.41$) and 350 W, 400 mm/s ($D/W \sim 0.23$). This suggests that while a good general guide, this keyhole porosity threshold is not a strict rule. In part, this is due to large melt pool widths fluctuation using the ImageJ contrast adding uncertainty to measurements. At the higher power and higher laser speed portion of the plot, the vapor depression morphologies were more likely to be a stable deep-wide conduction melt pool. Based on operating sufficiently far away from the unstable keyhole porosity regime while still having an adequately deep vapor depression, the ideal starting processing condition was identified (circled on map) as the 300 W, 800 mm/s case for the laser conditions considered.

This P-V setting has an ideal deep-wide melt pool morphology with a 62 micron deep and 440 micron wide melt pool (Ideal 300 W, 800 mm/s Laser Scan Video). The narrow blue band shows the processing window indicating the optimal path for alloy processing.

When the Rosenthal melt pool morphology map is compared to the experimentally observed Kanthal A1 data, we see regimes of agreement and divergence. While the Rosenthal model has a more gradual laser power versus laser speed slope for onset of keyholing, the observed data is more biased to low laser speeds. For example, the 300 W, 350 mm/s (857 J/m) has a very similar, even slightly lower, laser linear energy density than the 350 W, 400 mm/s (875 J/m), which according to the Rosenthal model should result in a similar melt pool depth and width (Eq. 3.3). However, the melt pool depth of the lower laser speed case exhibits keyhole porosity and has a vapor depression depth 49% deeper than that of the higher speed case. For the lower laser speed, the recoil pressure caused by the vaporization of the melt creates a vapor cavity [55]. This can result in a deeper melt pool where convection and radiation have an increasingly important role in heat transfer. Since the Rosenthal Model assumes conduction dominates, ignoring the impact of vapor formation at high powers and low speeds is the likely reason for this divergence [152]. This suggests the Rosenthal conduction model can be used as a general starting point close to the optimal processing condition of 300 W, 800 mm/s for FeCrAl alloy compositions similar to that of the Kanthal alloys (Fe-5.8%Al-22%Cr). The framework becomes less reliable with further deviations from the base composition and optimal processing condition.

The processing map for the particle reinforced Kanthal APM is shown in Fig. 3.3. Compared to the Kanthal A1, we again see similar trends from lack of fusion to keyholing. Keyhole porosity was observed for the high power 300, 350, and 400 W cases at the slowest laser speed tested for Kanthal APM, 400 mm/s. However, none of these cases had a melt pool depth to width ratio above 0.4. The optimal processing condition was also identified as the 300 W, 800 mm/s case with a very similar vapor depression depth (66 μm versus 62 μm) when compared to the Kanthal A1. However, the Kanthal APM had a 23% reduction in melt pool width (341 μm). In general, melt pool widths had a larger fluctuations between similar conditions than depths for the same conditions. Overall, the reinforced Kanthal APM processing map qualitatively matches the particle free Kanthal A1.

For a more quantitative comparison, the vapor depression depths for both alloys are compared for different laser powers as a function of laser speed (Fig. 3.4). For all laser powers and for both alloys shown the depth profiles quickly decrease before starting to plateau at higher laser speeds with vapor depths increasing between 250-400% from 400 to 1200 mm/s depending on laser power. As laser power increases, so does the vapor depression depth increasing from a maximum of 150-200 μm to 375-425 μm from 200 to 400 W (Fig.

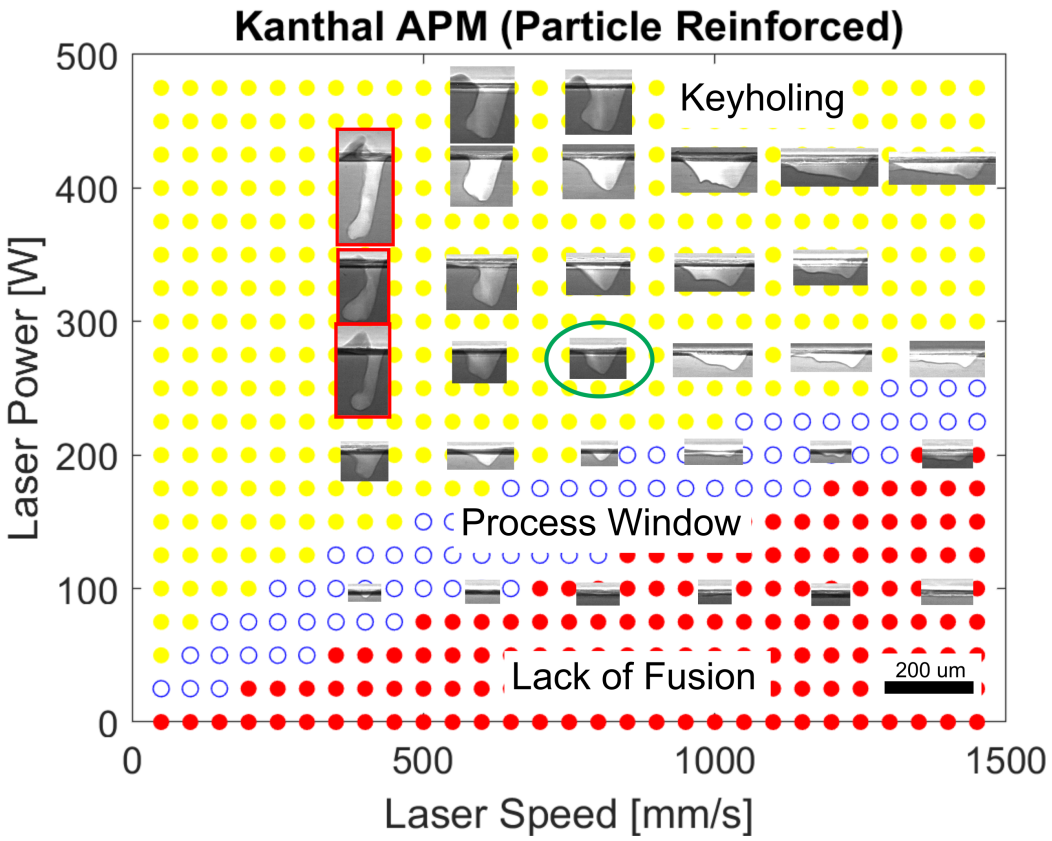


Figure 3.3: Laser Power vs Laser Speed Processing Map for Kanthal APM overlaid with Rosenthal Model. The images bordered in red had observable keyhole porosity. The circled green case at 300 W and 800 mm/s was identified as the optimal condition. The dotted background colors represent melt pool regimes.

3.4a,d). Keyhole porosity was only observed for vapor depression depths greater than 125 μm suggesting this as an upper limit for defect free layer thickness for the laser spot size used of 80 μm. Actual operation should occur well below this layer thickness as a safety margin for defects and improved surface finish.

When comparing the reinforced Kanthal APM and particle free Kanthal A1, both alloys follow the same general trends, and plateau to generally the same vapor depression depths for each laser power. The largest magnitude differences occur at the slowest common laser speed of 400 mm/s. These are the conditions where keyhole porosity was observed suggesting an unstable vapor depression that has a depth that fluctuates with position (Select 400 W Laser Scan Videos). Overall, across the conditions of Fig. 3.4, the two alloys are only 2% different with Kanthal APM having on average a 2 μm deeper melt pool. This is small enough to consider that both alloys can be represented by the same processability maps and onset transitions suggesting a path for low concentration reinforced alloys. However,

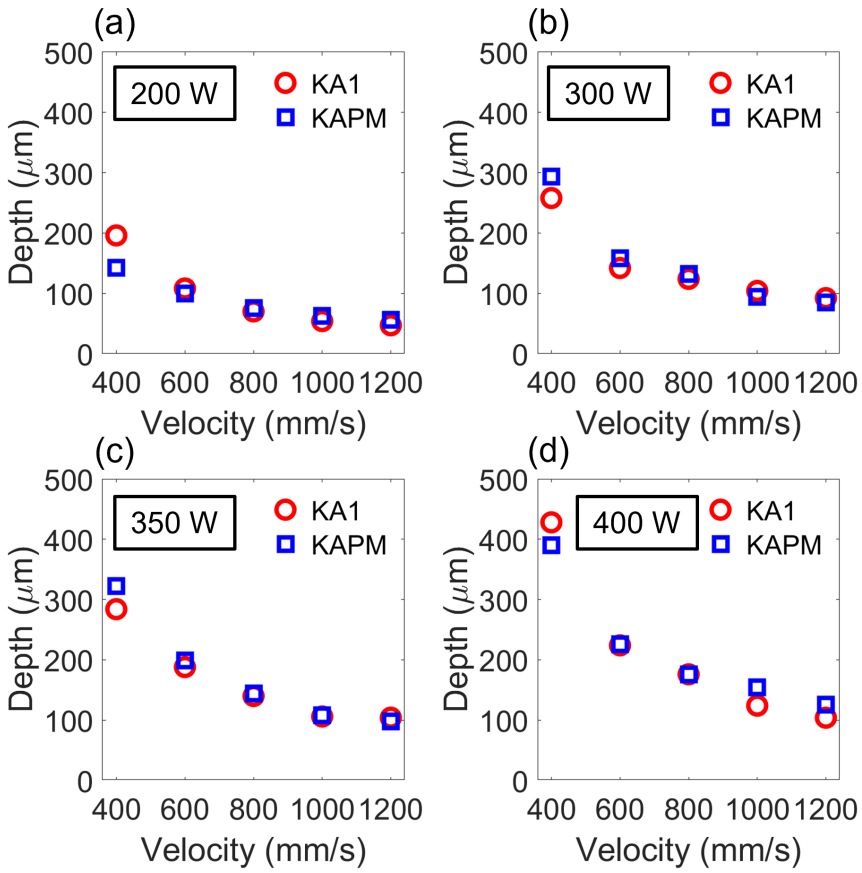


Figure 3.4: Vapor Depression Depth versus Laser Velocity for different laser powers. Comparison of Kanthal A1 and Kanthal APM.

additional melt pool depth and width measurements are needed to quantify the measurement uncertainty. While nanoparticles can impact melt pools by increasing viscosity this increase is proportional to concentration and inversely proportional to nanoparticle size [117], which suggests that 0.1 wt% of nanoparticles at $\sim$ 250 nm size is too low to significantly impact viscosity.

3.4 Conclusion

Laser power versus speed processing maps from *in-situ* dynamic X-ray radiography are shown for the particle-free Kanthal A1 and reinforced Kanthal APM FeCrAl alloys under a simulated laser powder bed fusion process. The lack of fusion to keyholing regimes are traversed with an ideal operating condition identified for both alloys of 300 W and 800 mm/s for a spot size of 80 μm, hatch spacing of 50 μm, and layer thickness of 30 μm. We see decent agreement between the Rosenthal model and observed melt pool morphologies with higher

laser speeds suggesting the model can be used as a first estimate for processability for similar FeCrAl alloys under certain conditions. When laser power increases at sufficiently low laser speeds, beyond a certain threshold ($>$ 200-300 W and $\leq$ 400 mm/s), the Rosenthal model is no longer a good estimate since recoil pressure creates vapor pockets where conduction is less important. This regime corresponds to the onset of keyhole porosity, but was not well predicted by melt pool depth to width ($D/W \geq 0.5$) in part due to large fluctuations in measuring melt pool width. Comparison between vapor depression depths for Kanthal A1 and Kanthal APM reveal a quick decline in vapor depth as laser speed increases from 400 to 600 mm/s with a more gradual decline for higher laser speeds. No significant difference in melt pool/vapor depression morphologies across the two alloys was observed suggesting that the low concentration of ODS particles for the Kanthal APM have minimal impact on melt pool morphology. The impact of this result suggests the same laser processing conditions of the base particle free alloy can be used as a starting condition when developing reinforced alloys with nanoparticle concentrations that while low ($\sim$ 0.1 wt%) are still high enough to significantly improve mechanical and corrosion properties. This provides a path for improving existing base alloy properties without changing base elemental composition. Additional experimentation, such as corrosion testing and high temperature creep tests, are needed to test if additively manufactured Kanthal APM has similar improvements compared to its conventionally manufactured version. Overall, the vapor depression and melt pool analysis of this study helps aid additive manufacturing development of both un-reinforced and reinforced FeCrAl alloys.

CHAPTER 4

Modeling and Experimental Demonstrations Reveal Ragone Framework for Salt Hydrate Thermochemical Energy Storage

Adapted in part from a manuscript under review: Kinzer, B., Ghosh, D., Crowley, D., Jatkar, A., Bala Chandran, R., "*Modeling and Experimental Demonstrations Reveal Ragone Framework for Salt Hydrate Thermochemical Energy Storage.*"

4.1 Introduction

A promising thermal energy storage approach is to store energy as heat in chemical bonds by driving reversible endothermic/exothermic reactions, i.e., thermochemical energy storage. This approach is estimated to yield high energy densities ($0.5 - 2\text{MJ/kg}_{\text{material}}$) that can be up to tenfold larger than thermal energy storage via phase change and sensible temperature change in materials [68, 69, 70, 67]. Notably, these energy densities can approach that of Li-ion batteries [154, 155] at a fraction of the cost ($\$100 - \$350$ vs $\$15 - \$75$ per kWh) [17, 85] for equivalent storage duration.

Common and simple salts including halides ($MgCl_2$, $CaCl_2$, $SrCl_2$, $SrBr_2$), sulphates ($MgSO_4$) and carbonates (K_2CO_3) are leading materials for thermochemical energy storage due to their low cost, low toxicity, and reasonable stability. The listed materials are especially attractive for building applications as they can discharge energy at temperatures appropriate for space ($\sim 40°C$) and water heating applications ($> 65°C$) [68, 69, 66, 156]. Heat is generated and consumed during the uptake (hydration) and release (dehydration) of water vapor, respectively. Water (vapor) is impregnated into the salt lattice structure, ideally without dissolution or any phase change during hydration/dehydration [68]. Salt hydrates and more broadly thermochemical materials have been targeted for seasonal storage

applications, because the chemical free energy can be stored indefinitely and loss-free at ambient conditions[87, 81, 88, 89, 90, 83]. Salts are charged over the summer using excess solar and/or wind, and then slowly discharged during winter for heating applications resulting in a small number of charge/discharge cycles with low power densities ($\sim$ 1 W/kg). Several salt hydrate materials have been demonstrated experimentally, for multi-day and seasonal storage applications [83, 99] such as with a 400 kg pure $SrBr_2$ reactor with a reported specific power of 0.75-2.0 W/kg [87, 83]. $SrBr_2$ vermiculite composite has also been shown to be a stable, cyclable, salt-hydrate material for thermochemical energy storage [66, 80, 96, 76, 77], and therefore is experimentally characterized in our study. High power reactors consisting of a thin layer of $<$ 1 kg of LiCl vermiculite and $CaCl_2$-graphene aerogel salt have also reached specific powers well over 100 W/kg [97, 157].

Donkers et al. presented a comprehensive analysis of opportunities and limitations for seasonal heat storage with salt hydrate materials concluding that none of the 25 screened salt hydrates were viable for seasonal storage for the proposed 10 GJ capacity residential systems [66, 81]. The most promising salt, K_2CO_3, based on specific screening criteria, would require a massive 75 tons of salt to store the estimated $\sim$50 GJ the average U.S. residential household consumes annually for space and water heating end-use applications [158]. Since the economic value stream occurs at most a couple of times per year for seasonal storage, this imposes very low cost targets – \$3 per kWh for $\sim$100 h of storage [84]. While these aggressively low cost targets might be hard to achieve with salt hydrates, recent studies demonstrate the promise of $CaO/Ca(OH)_2$ materials [159].

Even though many thermochemical materials may not be currently lucrative for seasonal storage, they could be promising for daily load shifting applications with higher cost targets; Albertus et al. point to a target of $\sim$ \$40 per kWh for $\sim$10 hours of storage [84]. In contrast to the many tons ($>$ 10 tons) of salt needed for seasonal storage, only a few dozen kilograms is required in this case, and presents a pathway for modular, on-site thermal storage for buildings. In our recent investigation, Pham et al. demonstrated that discharge power densities have to be sufficiently large (up to 100 W/kg) to take advantage of electricity price arbitrage for building heating applications [78]. This, together with the recently proposed U.S. Department of Energy target of shifting 4 hours of peak load for residential homes using thermal energy storage [85], point towards the need for materials and salt hydrate reactor designs that can discharge at high specific power ($>$ 44 W/kg and $>$ 188 W/kg for $SrBr_2$ composite and $MgSO_4$ respectively based on a 4 hour discharge of their maximum specific energy of roughly 175 Wh/kg and 750 Wh/kg respectively [160]).

When a storage system is discharged rapidly to meet high demands in specific power, for instance, to match a steep ramp-up in grid power demand, only a fraction of the total storage

capacity can be utilized effectively. The Ragone framework was introduced to explicitly quantify these tradeoffs in specific power (W/kg) and the specific energy (Wh/kg) [94]. This framework was originally applied to Li-ion batteries, where high discharge rates cause higher voltage drops, and therefore more quickly attains the cut-off voltage, below which the battery cannot be operated [94, 161]. The same framework has recently been adapted and applied to phase-change thermal energy storage [5, 162, 163, 164, 165, 166]. However, the thermochemical salt hydrate community has only recently begun reporting power densities at specific points during discharge based on experiments at the materials-scale ($\leq$ 1 g of materials tested) [97, 167, 168]. Therefore, these tradeoffs are not as extensively reported at the larger, reactor-scale with $\sim$100 – 1000 g of materials.

Heat and mass transfer models combined with reaction rate kinetics in porous media have been previously developed for salt hydrate [90, 103, 169, 104] and sorption materials in traditional packed bed reactors [103, 104, 72, 170]. Models have also been developed to assess performance improvement in new reactor designs, such as the use of truncated cones to reduce pressure drop [9], in honeycomb reactor designs with metallic fins to improve heat transfer [171], and to propose radial flow reactors to maximize reaction rates [172]. For salt hydrate materials, comprehensive models have been developed that traverse various operating regimes limited by either mass transport or reaction kinetics, or when influenced by both in the transition regime [169, 91, 92]. Huinink et al. developed a rigorous analytical modeling framework to predict the velocity and width of a moving reaction front during hydration for an infinitely long and isothermal packed beds of large (millimeter sized) particles [169]. On the basis of a Damkohler number [93], limiting factors due to mass transfer or kinetics, or due to both factors in a mixed regime is identified, and related back to the reacting front velocity and width, and the power output. However, this study did not consider finite-size effects of the packed bed and the energy balance equation to obtain effects of local temperature gradients, which results in high-end estimates for the specific power discharged during hydration. Additionally, tradeoffs between the estimated specific power and specific energy, and their dependence on the Damkohler number was not quantified. A recent study by Raemakers et al., provided experimental validation of the theoretically predicted transition from mass transport to kinetic limitations with increasing flow rate using K_2CO_3-graphite composite [91] materials using nuclear magnetic resonance imaging of packed bed reactors. Even with all these significant outcomes, there remains a gap in comprehensive multiphysics model predictions for the specific power and energy tradeoffs, their dependence on reactor design, transport and kinetic conditions, and a connection of these results with daily load-shifting applications. Additionally, most model-based predictions for salt hydrate/sorption packed bed reactors either empirically fit kinetics to reactor

performance [90, 170, 173] or use experimentally measured inputs for kinetic parameters from the materials-scale thermogravimmetric measurements [9, 171], but do not directly compare predictions of changes in design with experiments at the reactor-scale. This leads to a disconnect in the specific power and capacity tradeoffs between the materials- and the reactor-scale models and measurements[168, 91, 174].

Our study bridges these knowledge gaps across different length-scales with integrated computational modeling and experimental characterization at both the materials- and the reactor- length scales. Multiphysics, continuum models are developed at the reactor-scale to probe the interplay of flow, heat and mass transport, and hydration reactions in packed beds of salt particles for varying design and operating conditions. Experimental characterization of overall thermochemical performance and in quantifying tradeoffs in specific power and energy is performed with $\sim$ 100 g of $SrBr_2$ vermiculite composite in a packed bed reactor as a function of three different air flow rates. This material is specifically selected as it has been reported to be stable for thermal cycling, but predominantly characterized at the reactor-scale [175] for long duration storage ($>$ 100 hours) applications. Results and comparisons shed light on key dimensionless parameters and the sensitivity of select model parameters in predicting overall performance, and importantly provide a pathway to directly interrogate and understand the scaling gap between the materials- and reactor-scale measurements. Notable advancements of our work compared to prior studies include the (1) development and application of Ragone plots for salt hydrate thermochemical reactors to compare tradeoffs between reactor energy and power at both the materials- and the reactor-scale; (2) identification of reduced-order, dimensionless parameters that govern specific power and energy tradeoffs; (3) assessment of limitations of mass transport versus kinetics regimes showing increasing air velocity eventually has a diminishing return on power output for high power applications, and (4) an experimental investigation of $SrBr_2$ vermiculite composite reactor demonstrating operation at 9 W/kg (20 hour discharge) at $>$ 95% composite conversion. On the whole, our study advances fundamental understanding to enable the development of emerging, salt hydrate thermochemical energy storage reactors for daily load shifting in building space and water heating applications .

4.2 Methods

This study applies both computational and experimental methods to characterize the performance of salt hydrates in a packed bed reactor. For the modeling study, we consider two salt hydrates based on their high energy densities, stability, and low recharge temperatures during dehydration: pure potassium carbonate (K_2CO_3) and strontium bromide-expanded

Table 4.1: Material properties, kinetic parameters, and packed bed reactor design and morphology categorized based on the materials — K_2CO_3 and $SrBr_2$ composite considered for baseline model predictions and experimental conditions

	Parameters	K_2CO_3 [171, 176]	$SrBr_2{\cdot}1H_2O$ [177, 95]	
		Base Model	Base Model	Experiment
Salt properties	Reaction enthalpy, ΔH_{rx}	3.56 MJ/kg_{H2O}	3.35 MJ/kg_{H2O}	$1.95 - 3.35$ MJ/kg_{H2O}
	Particle diameter, d_p	500 μm	500 μm	2-3 mm
	Thermal conductivity, k_s	0.4 W/(mK)	0.22 W/(mK)	
	Specific heat, $C_{p,s}$	830 J/(kgK)	710 J/(kgK)	
	Dehydrated density, ρ_s	2210 kg/m^3	620 kg/m^3	
	Molar mass, M_s	0.1382 kg/mol	0.2654 kg/mol	
Reaction kinetics	Activation energy, E_a	46.22 kJ/mol	N/A	
	Rate constant, C_0	5.14×10^4 1/s	3.18×10^{-4} 1/s	
	Kinetic pre-factor, K^*	0.5 – 2.0	0.05 – 1.0	
	Number of moles of water, N	1.5	5	
	Salt loading ratio, w_s	0.196 kg_{H2O}/kg_{salt}	0.187 kg_{H2O}/kg_{salt}	
packed bed reactor	Porosity, ε	0.6	0.6	0.5
	Length, L	0.125 m	0.125 m	0.125 m

vermiculite composite ($SrBr_2$ composite) [66, 76, 77]. Their corresponding reactions are $K_2CO_3(s) + 1.5H_2O(g) \longleftrightarrow K_2CO_3 \cdot 1.5H_2O(s)$ and $SrBr_2 \cdot 1H_2O(s) + 5H_2O(g) \longleftrightarrow SrBr_2 \cdot 6H_2O(s)$. Parametric explorations are performed to predict the influence of air flow velocity and relative humidity, reactor length, and kinetic parameters on performance. Experiments are conducted with the $SrBr_2$ composite, at both the materials (1 g) and the reactor-scale (100 g). Models are applied to predict, compare, and interpret experimental data obtained for this reactor only with the $SrBr_2$ composite.

4.2.1 Theoretical/Computational modeling approach

A transient, two-dimensional (2D), continuum model is developed for moist air flowing through a packed bed reactor with solid particles. Pure K_2CO_3 and $SrBr_2$ composite particles constitute the solid phase, while the fluid phase (humid air) is modeled as a mixture of air and water vapor. Finite element discretization of the governing equations for mass, momentum, species and energy conservation is performed in COMSOL [178]. In this study, we only focus on modeling the thermal discharge step involving hydration of the salt, although the same model can also be modified and applied to investigate the thermal charging step with dehydration reactions in the salt.

Modeling Domain: Fig. 4.1a shows the computational domain with the initial and bound-

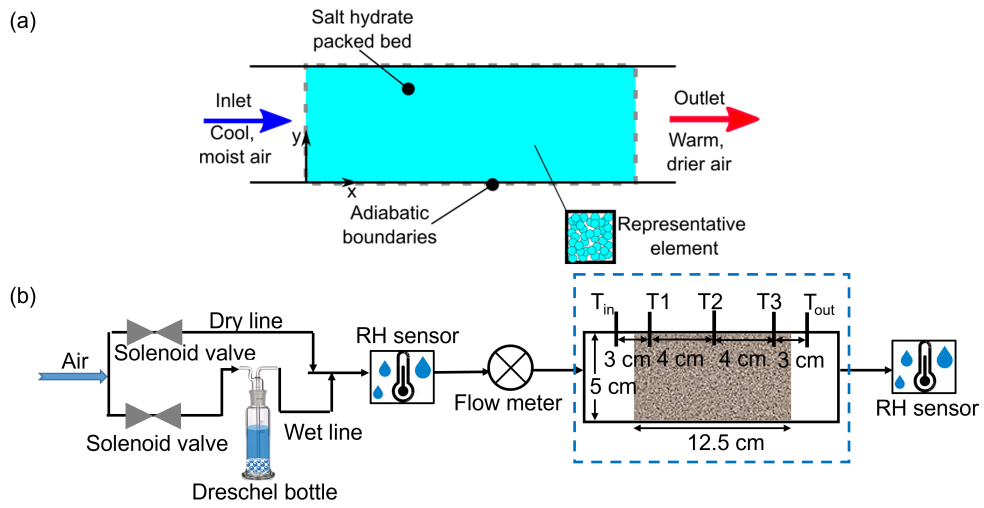


Figure 4.1: (a) Computational continuum modeling domain for hydration reaction and (b) schematic of the experimental flow loop in a packed bed reactor with salts undergoing thermochemical hydration and dehydration reactions for energy storage.

ary conditions. A 2D, rectangular cross-section, is filled with a packed bed of monodisperse, spherical particles of the material of interest. Particle diameters of 500 μm and 3 mm are considered depending on the study. The baseline length, L, and width, W, of channel in the model are 0.125 m and 0.05 m respectively with an assumed depth, D, of 0.05 m, and these dimensions match with the experiments.

Key modeling assumptions include: (i) humid air is treated as an ideal gas mixture of air and water vapor; (ii) local thermal equilibrium is assumed between the solid and the fluid phases supported by a scaling analysis, which shows that the expected temperature difference between the two phases is much less than 1°C (Section B.2); (iii) for $SrBr_2$ composite, the $SrBr_2$ and vermiculite are treated as a single solid phase rather than separating contributions from each component; and (iv) adiabatic reactor walls to preclude any heat loss.

Initial Conditions: The initial temperature of both the solid and fluid phases are the same as the inlet temperature of the air to the packed bed, T_{in}; initial water vapor concentration, c_{in}, is obtained based on the inlet air relative humidity (RH) and saturation pressure for water, p_{sat}, as $c_{\text{in}} = RHp_{\text{sat}}/(RT)$ where the $R = 8.314$ J/(K mol) is the ideal gas constant and p_{sat} in Pa is obtained from the Antionne equation (Eq. 4.1 [179]). RH is given by $RH = p_{\text{f}}/p_{\text{sat}}$. The fluid phase is initialized to be at rest, $\vec{u} = 0$.

$$p_{\text{sat}} = 10^5 \times 10^{6.21-\left(\frac{2355}{T+7.559}\right)} \tag{4.1}$$

Boundary Conditions: The top and bottom walls are modeled with no-slip for flow, and

no-flux for temperature and species. The adiabatic (no heat loss) assumption for the reactor is an idealization, but allows us to predict maximum power output from the materials. At the inlet, moist air is supplied at prescribed relative humidity and at an inlet temperature of 20°C, unless stated otherwise. The baseline value for the inlet relative humidity of $RH_{\text{in}} = 45\%$, leads to stable hydration for $SrBr_2$ composite, but above the the deliquescence point for the pure K_2CO_3, where salt solutions can form [69, 180]. However, this effect is ignored in our study. At the outlet, the pressure is constrained to be atmospheric for the fluid phase; for both temperature and species concentration in the solid and fluid phases the outflow boundary condition is implemented, which translates to convection-driven species and energy transport at the outlet, and therefore no diffusive flux normal to the outlet.

Model Parameters: Table 4.1 provides relevant thermophysical properties for both materials modeled in this study, and categorized based on the models that are purely predictive, and with some modifications included to better compare models against measurements for the $SrBr_2$ composite; pertinent properties for air and water vapor are listed in Table B.1. All thermophysical properties are assumed to be constant and obtained at 300 K, unless otherwise mentioned. For the pure K_2CO_3, reported experimental data from Gaeini et al. [4] is used for reaction kinetics and the hydration reaction enthalpy. For the$SrBr_2$ composite, specific heat and thermal conductivity properties are adopted from the literature by assuming a weighted average of $SrBr_2$ and expanded vermiculite properties based on the 50 wt%-50 wt% $SrBr_2$ vermiculite ratio [177, 95]. Reaction kinetics and enthalpy values are obtained from in-house experimental data (Section B.3).

Governing equations: Volume-averaged equations are used for the solid and the fluid phases in the porous medium for all conservation equations [74, 181, 182]. While the permeability, bulk density, and the porosity (intra- and inter-particle) is expected to change as a function of the fractional hydration extent [87], these values are assumed to be constant to retain simplicity in our analysis. The density of the solid phase in all the transport equations corresponds to that of the dehydrated state of the salt (Table 4.1). Standard porous media transport equations for mass, momentum, energy and species transport are applied, and provided in Section B.1. Specific details on the reaction kinetics is elaborated below.

Reaction kinetics: Reaction rate equations for most common salt hydrates are obtained from thermogravimmetric measurements [183]. Therefore, we adopt a functional form for the rate equation that is broadly relevant for fitting thermogravimmetric data as in Eq. 4.2 adapted from Kant et al., [171] that applied a general reactive gas-solid model from Mazet et al., [184] for hydration reactions in salts,

$$\dot{\alpha} = K^{*} C_0 exp\left(-\frac{E_{\text{a}}}{RT}\right)(1-\alpha)^n \left(1-\frac{p_{\text{eq}}}{p_{\text{f}}}\right)^m \tag{4.2}$$

where $\dot{\alpha}$ is the rate of change in the fractional hydration extent, α. $\alpha = 0$, represents a fully dehydrated salt, and $\alpha = 1$ corresponds to the fully hydrated state. C_0 is the surface-dependent and material-dependent reaction rate constant; E_a is the Arrhenius activation barrier that makes reaction kinetics to be strongly dependent on temperature. This functional form in Eq. 4.2 is affected by materials-specific factors, as kinetics can be limited either individually or due to the combined effects of diffusion rates of water vapor, nucleation rates, geometric swelling/shrinking of the particles, and intrinsic reaction order with respect to the reaction extent [183]. In Eq. 4.2, $n = 1$ for $SrBr_2$ composite, and $n = 2/3$ is applied for the pure K_2CO_3 salts based on reported limitations due to the reaction order [183] and particle size shrinking/swelling during dehydration/hydration respectively [4]. K^* is an additional kinetic pre-factor term used to perform parametric explorations on the reaction rate constant. Finally, the rate of reaction also depends on the relative difference between the local partial pressure of the water vapor, p_f, and the temperature-dependent equilibrium water vapor partial pressure, p_{eq}, quantified by $\left(1 - \frac{p_{eq}}{p_f}\right)^m$, where the order, m is empirically determined from measured data. For both materials considered, $m = 1$ is assumed in this study. The implication of this term is that the reaction rate will increase, the farther the local water vapor pressure, p_f, is from the equilibrium pressure, p_{eq}, and becomes 0 when equilibrium is attained. The equilibrium vapor pressure and its dependence varies from one salt to another, and having a pure versus a composite salt. The relative difference in the local and equilibrium water vapor pressure could have also been quantified by a different form, $\left(\frac{p_f}{p_{eq}} - 1\right)^m$ during hydration [183]. We ran a few of our simulation cases with this variant of the equation, and observed that largely similar trends in results are obtained, but the magnitudes can be different dependent on the flow rates tested.

The temperature dependent kinetic parameters (Table 4.1) and equilibrium vapor pressure, $p_{eq,K2CO3}$, terms (Eq. 4.3) are adopted from literature for the pure K_2CO_3 [4]. However, since the $SrBr_2$ composite is synthesized in-house, thermogravimmetric (1 g) measurements are performed at two different relative humidity (30% and 45% RH) to yield best-fit datasets for $p_{eq} = 255$ Pa, and $C_0 exp\left(-\frac{E_a}{RT}\right) = 3.2 \times 10^{-4}$ 1/s, at room temperature, $T = 22°C$. Since the measurements are only conducted at room temperature, the reported activation barrier of, $E_a = 8044$ K for the pure $SrBr_2$ is assumed [83]. Therefore, our current fitting process does not fully consider the effects of temperature on both, the true activation barrier and the equilibrium vapor pressure for the $SrBr_2$ composite, $p_{eq,\ SrBr2\text{-}composite}$ (Eq. 4.4). More comprehensive details of these measurements and the fitting process are detailed in Section B.3 and Fig. B.1. In both Eq. 4.3 and Eq. 4.4, the equilibrium vapor pressure is expressed in Pa.

$$p_{eq,K2CO3} = 4.228 \times 10^{12} exp\left(\frac{-7337}{T}\right) \tag{4.3}$$

$$p_{\text{eq, SrBr2-composite}} = 1.741 \times 10^{14} exp\left(\frac{-8044}{T}\right) \tag{4.4}$$

The rate of change in the fractional hydration extent informs the volumetric rate of water vapor uptake by the particles, $\dot{r}^{'''}$ (Eq. 4.5), in the species conservation equation (Eq. B.1 in Section B.1) and the volumetric rate of heat release (Eq. 4.6) due to exothermic hydration reactions

$$\dot{r}^{'''} = N\rho_{\text{s}}\frac{M_{\text{v}}}{M_{\text{s}}}\left(1-\varepsilon\right)\dot{\alpha} \tag{4.5}$$

where, N is the number of moles of water involved in the salt reaction (Table 4.1), M_{v} and M_{s} are the molar mass of water and the salt respectively, ρ_{s} is the bulk density of the dehydrated salt particles, and ε is the porosity.

$$q^{'''} = \Delta H_{\text{rx}}\dot{r}^{'''} \tag{4.6}$$

where ΔH_{rx} is the salt reaction enthalpy ($\text{MJ/kg}_{\text{H2O}}$).

Damkohler analysis: We use a dimensionless Damkohler number, Da, which compares rate of reaction with that of species transport [93], to generalize the dependence of Ragone plots on design and operating conditions. Da in Eq. 4.7 is specifically defined as the ratio of the maximum possible reaction rate, which is expected initially at the inlet of the packed bed, to the rate of convective mass transport of the reacting water vapor. Therefore, $Da << 1$ is generally indicative of kinetically-limited operation conditions, whereas, $Da >> 1$ transitions to a transport limited operating regime.

$$Da = K^{*}C_0 exp\left(-\frac{E_{\text{a}}}{RT}\right)\left(1-\frac{p_{\text{eq}}}{p_{\text{f}}}\right)\frac{L}{\vec{u}}\frac{\rho_s(1-\varepsilon)w_{\text{s}}}{\rho_{\text{f}}\xi_{\text{f}}} \tag{4.7}$$

where the hydration reaction rate at the inlet is given by Eq. 4.8 and the rate at which water vapor is supplied to the reactor is given by Eq. 4.9

$$\dot{r}_{\text{reaction}} = \rho_s AL\left(1-\varepsilon\right)w_{\text{s}}\dot{\alpha}|_{\text{inlet},\alpha=0} \tag{4.8}$$

$$\dot{r}_{\text{transport}} = \vec{u}A\rho_{\text{f}}\xi_{\text{f}} \tag{4.9}$$

In Eq. 4.9, A is the cross-sectional area of the reactor, $\vec{u}$ is the Darcy or the superficial velocity, and ρ_{f} the water vapor density. $\xi_{\text{f}} = \frac{m_{\text{v}}}{m_{\text{v}}+m_{\text{da}}}$ is the saturation water vapor mass loading fraction with m_{v} as the water vapor mass and m_{da} is the dry air mass, which we assume a constant $\xi_{\text{f}} = 0.15$ $\text{kg}_{\text{H2O}}/\text{kg}_{\text{air}}$ for this study. In Eq. 4.8, L is the length of the reactor, ε is the reactor porosity, and w_{s} is the salt loading ratio, which is the stoichiometric

mass of water that gets added during hydration per unit mass of the total salt present in its pure or composite (includes both pure salt and composite host). $\dot{\alpha}|_{\text{inlet},\alpha=0}$ represents the maximum reaction rate based on the intrinsic kinetics (Eq. 4.2) for the salt at the given inlet humidity. $\dot{\alpha}|_{\text{inlet},\alpha=0}$ is evaluated at $\alpha = 0$ since this is when the reaction rate is fastest providing a constant, upper bound to evaluate Da based on material properties.

Parametric explorations : To traverse operational regimes limited by mass transport or kinetics, or transition/mixed regimes that are influenced by both, parametric sweeps are conducted to explore a wide range of Da (59.5-0.4 for K_2CO_3 and 14.7-0.1 for $SrBr_2$ composite for base model values). Variations in Da can track changes in both reactor design (e.g., geometry and dimensions of the packed bed) and the operating conditions (air flow rate, inlet humidity). For instance, Da will increase when the air flow rate slows down or when the length of the packed bed becomes larger or with improved kinetics for the material. For our study, largely only the inlet velocity, $\vec{u}$, reactor length, L, and the kinetic pre-factor, K^*, are varied to achieve the variations in Da; a comparison case is evaluated by also varying the inlet relative humidity. Inlet velocities of $\vec{u}$ = 0.013-2 m/s, L = 0.03125-1.2 m and K^* = 0.05-2.0 are modeled.

Simulation procedure: An extra fine triangular mesh of roughly 0.0025 m elements is used, which is determined by reducing the mesh size until halving the mesh no longer has any impact on the results or stability for a $SrBr_2$ composite simulation at $\vec{u}$ = 0.013 and 2 m/s to test the extremes of the simulation ($< 0.1\%$ difference). The adaptive time step, Δt, ranges from an initial value of 10^{-4}s to 200 s as the simulation progresses to ensure convergence and to minimize simulation time. Doubling of initial time step again has $<$ 0.1% difference in reaction time. All simulations are run from a fully charged state until the entire reactor is fully reacted. For many cases, the reaction slows down dramatically when $\alpha > 0.98$, and therefore we end the simulations then to avoid stability issues.

4.2.2 Ragone plots

Ragone plots that quantify specific power as a function of the specific energy capacity are obtained, both from model predictions and measurements. Instead of reporting instantaneous quantities, time-averaged specific power is obtained versus the time-averaged capacity that is utilized up to a select amount of time, t. This study focuses on reporting time-averaged quantities to understand tradeoffs across the entire discharge period and reactor utilization rather than a specific moment.

From a modeling standpoint, these quantities are directly calculated from the predicted

outputs in Eq. 4.10 and Eq. 4.11.

$$\overline{sP}_{\text{chem, model}} = \frac{k_{\Delta H_{\text{rx}}} \int_0^t \langle \dot{\alpha} \rangle \, dt}{t} \tag{4.10}$$

$$\overline{sE}_{\text{chem, model}} = k_{\Delta H_{\text{rx}}} \int_0^t \langle \dot{\alpha} \rangle \, dt \tag{4.11}$$

where $\langle \dot{\alpha} \rangle$ is the instantaneous, spatially-averaged values of the fractional hydration rate calculated in the model; $k_{\Delta H_{\text{rx}}}$ is a conversion factor that converts the reaction enthalpy (Table 4.1), ΔH_{rx}, which is normalized per unit mass of water uptake, to per unit total mass of the active material, i.e., pure salt or composite, undergoing reactions. This conversion factor is related to the reaction enthalpy as, $k_{\Delta H_{\text{rx}}} = 277.8 \frac{\text{Wh}}{\text{MJ}} \Delta H_{\text{rx}} \frac{M_{\text{f}}}{M_{\text{s}}} N$. Since $\langle \dot{\alpha} \rangle$ directly calculates the reaction rate, energy that goes into sensible heating of particles is captured, which would not be the case for a calculation based on inlet and outlet temperatures. However, this effect only largely impacts the results in the initial duration when $\alpha < 2\%$.

To obtain the materials-scale specific power and energy in Ragone plots, the instantaneous reaction rate expression (Eq. 4.2) with kinetic parameters in Table 4.1 in Eq. 4.10 and Eq. 4.11 is used; for $SrBr_2$ composite $\Delta H_{\text{rx}} = 3.35$ MJ/kg_{H2O} is assumed.

From the reactor-scale measurements, the specific power and energy are obtained using Eq. 4.12 and Eq. 4.13 respectively, where, the integrals are replaced with summation over discrete time steps. Since spatially-averaged reaction extents, α, are not directly measured, the specific power is obtained based on the measured air temperatures at the inlet, T_{in}, and the outlet, T_{out}, and the specific energy is obtained by integrating the instantaneous specific power measured. Eq. 4.13 ignores any sensible heat stored in the solid particles. However, this again only impacts results when $\alpha < 2\%$.

$$\overline{sP}_{\text{chem,exp}} = \frac{\dot{m}_{\text{f}} C_{\text{p,f}} \sum_{i=0}^{t} (T_{\text{out}} - T_{\text{in}}) \, \Delta t_{\text{i}}}{m_{\text{s}} t} \tag{4.12}$$

$$\overline{sE}_{\text{chem,exp}} = \sum_{i=0}^{t} \overline{sP}_{\text{chem,exp}} \Delta t_{\text{i}} \tag{4.13}$$

where, $C_{\text{p,f}}$ is the specific heat of air, m_{s} is the total mass of the dehydrated pure salt/composite, and $\dot{m}_{\text{f}} = \rho_{\text{f}} \vec{u} A$ is the air mass flow rate, and $\Delta t_{\text{i}} = 5$ s is the experimental sampling rate.

4.2.3 Parasitic power for pumping and humidification

The viability of the salt hydrate reactor depends not just on maximizing the thermochemical power output (Eqs. 4.10, 4.12), but also towards minimizing parasitic power requirements due to pumping [176] and humidification [81].

The instantaneous power required to pump air through the porous bed to overcome the pressure drop due to both inertial and viscous drag effects is calculated as in Eq. 4.14, and normalized per unit mass of the total mass of the pure/composite salt material present in the reactor [176].

$$sP_{\text{pump}} = \frac{AL\vec{u}\nabla p}{AL\rho_s(1-\varepsilon)} = \frac{1}{\rho_{\text{s}}(1-\varepsilon)}\left(\frac{\mu_{\text{f}}}{\kappa}\vec{u}^2 + \frac{C_{\text{f}}\rho_{\text{f}}}{\sqrt{\kappa}}\vec{u}^3\right) \tag{4.14}$$

where the pressure gradient, ∇p, is described in Eq. B.2.

The maximum energy penalty for humidifying the air stream is the enthalpy of vaporization of water, $\Delta H_{\text{vap,water}} = 2.43$ MJ/kg$_{\text{H}_2\text{O}}$ [185]. However, the target water vapor concentrations in the inlet stream (e.g., 45% RH is modeled in this study) may only require a fraction of this moisture if humidity can be sourced from the ambient. Therefore, in Eq. 4.15 we scale the enthalpy of vaporization by a moisture supply mass fraction parameter, ξ_{humid}, which will be dictated by the relative humidity needed in the inlet stream, RH_{in}, to achieve the target inlet vapor concentration. To convert to an instantaneous specific power, we multiply by the mass flow rate of air, $\dot{m}_{\text{f}}$ and again normalized by total salt mass, m_s.

$$sP_{\text{humid}} = \xi_{\text{humid}}\frac{\Delta H_{\text{vap,water}}\dot{m}_{\text{f}}\xi_{\text{v}}RH_{\text{in}}}{m_{\text{s}}} \tag{4.15}$$

4.2.4 Experimental

Materials preparation: Strontium bromide and expanded vermiculite composite is synthesized using a previously reported wet impregnation method in a $\sim$ 1:1 mass ratio of $SrBr_2$ and vermiculite [96]. Prior to the composite formation, the expanded vermiculite (Millipore Sigma 2-3 mm) is subjected to dehydration by heating in a muffle furnace (Omni R & D 1 L) at approximately 120°C to eliminate any moisture present. Next, the $SrBr_2$ (Thermo Scientific 99% purity) solution is prepared by dissolving the salt in deionized (DI) water, and then thoroughly mixed with the vermiculite to ensure uniform impregnation into pores. The resulting $SrBr_2$ vermiculite mixture is subjected to further heat treatment in the muffle furnace at approximately 120°C (±5°C/min) in batches of 100 g for a duration of nearly eight hours to completely dehydrate the salt composite, when changes in sample mass becomes negligible. Stoichiometrically, a mass change of 16.95 g is expected for every 50 g of

the $SrBr_2 \cdot H_2O$ present in the mixture.

Reactor design, fabrication and instrumentation: The reactor is fabricated using a square polycarbonate tube (McMaster) with dimensions of L x W x H of 20 cm x 5 cm $\times$ 5 cm (Figure 4.1b); Fig. B.7 in the SI shows a picture of the real reactor without insulation. Inside the reactor, the salt composite is carefully positioned with aid of plastic meshes (McMaster, mesh opening size of 0.4 mm) placed near the inlet and outlet, and covering the cross-sectional area. Two thermocouples are placed in the pure air stream near the inlet and outlet of the packed bed , and three additional thermocouples are placed within the 12.5 cm salt composite section (Figure 4.1b; Fig. B.7). To minimize heat losses, two layers of 0.75" thick Buna-N/PVC foam (Supplier McMaster, R value 3) are used for insulation.

The reactor is instrumented with an in-house humidistat flow loop [186]. The flow loop incorporates solenoid valves (Enfield, PFV-W12E05-P050C-0200) to control the relative humidity of the inlet air stream, humidity sensors (Adafruit, SHT45, $\pm$1% RH), an inlet flow meter to control the humid air flow rate (Sensiron, SFM4300-20-P, $\pm$2%), K-type thermocouples (Frienda, ke6u9, $\pm$0.5°C), and a temperature logger (Pico Log, TC-08), to record and log temperature changes throughout the experimental process, as illustrated in Figure 4.1b. The uncertainties associated with the instrumentation are used when reporting measured data as described in Section B.6 and Table B.2. To generate the necessary humidity and flow rate, the dry air stream is mixed with the wet air stream from a Dreschel bubbler (Al-WSCI, Borosilicate Glass, 600 ml). Precise regulation of both the dry and wet air flow rates is achieved by controlling the solenoid valves with an Arduino Proportional-Integral-Derivative (PID) controller, whose parameters (baseline values,$K_\mathrm{p} = 0.6, K_\mathrm{i} = 0.75\mathrm{s}^{-1}, K_\mathrm{d} = 0.0005\mathrm{s}$) parameters are adjusted to supply steady humidity values within 2 minutes of the start of the experiment. All measured outlet flow rates are within 3% of the inlet flow rate, signifying minimal leakage. To calculate the net uptake of water vapor by the pure/composite salt in the reactor, its mass is measured before and after a full hydration measurement with a lab balance(RUISHAN Lab RSTP, $\pm$ 10 mg). From these measurements the fractional extent of hydration at the end of every measurement is obtained (Section B.5 and Fig. B.6).

Unless otherwise mentioned, all experiments are conducted with the inlet air at room temperature, approximately 22°C , and with an inlet humidity set at 45%. To explore the effects of decreasing Da number, three different mass flow rates — 2, 4 and 6 standard litres per minute (LPM) are used. The maximum air flow rate is constrained to 6 LPM based on the orifice opening of the solenoid valves. To parallelize testing efforts, a dedicated reactor is used for every flow rate tested, and the test is repeated 3 times at each flow rate. At a fixed flow rate, the composite material is replaced by a new batch only if it exhibited drastically different reactivity compared to other trial measurements. The reactions are continuously

monitored until the outlet humidity is within 2% of the inlet humidity of 45%, indicative of complete reaction or full hydration of the salt composite. After every hydration step, the salt is recharged/dehydrated by supplying dry air (0% RH) at either room temperature (22°C) or at a slightly warmer temperature (30°C) to accelerate the rate of dehydration. As a control measurement and to isolate the influences of the vermiculite host on the hydration behavior, one trial is performed with a packed bed of particles with fully dehydrated vermiculite in the reactor at 2 LPM, 4 LPM, and 6 LPM (Fig. B.5 and Fig. B.6).

4.2.5 packed bed reactor: Experiment and model comparisons

Packed bed reactor model predictions are compared to experimentally measured data for the $SrBr_2$ composite. Select model parameters are modified for the sake of these comparisons to better match the experimental conditions, and these differences are noted wherever relevant, and listed in Table 4.1 within the experimental category. Specifically, larger, millimeter-sized particles are tested experimentally compared to the 500 μm particle size modeled for baseline conditions. When the model is used to compare against experimental measurements, the same adiabatic boundary condition is adopted, but the reaction enthalpies are adjusted so that it effectively accounts for the heat losses that occur in practice (Table 4.1). Reaction enthalpies of 1.95 MJ/kg_{H2O}, 2.42 MJ/kg_{H2O}, and 3.35 MJ/kg_{H2O} are used for air flow rates of 2, 4 and 6 LPM respectively based on the ratio of the measured energy output and the measured mass of the water uptake of the reactors. While in theory this specific reaction enthalpy should not be dependent on the flow rate, these differences arise due to changes in the actual heat losses under these test conditions. Based on heat-loss estimation experiments (Section B.7, Fig. B.8, Table B.3) conservative estimates show that rate of heat loss can be as much as 57%, 18% and 23% of the thermochemical power output for the 2, 4 and 6 LPM cases respectively. This general trend of decreasing heat losses with decreasing residence time in part explains the increase in the measured reaction enthalpy with air flow rate.

Packed bed porosity and salt density from neutron computed tomography: To better estimate inter-particle porosity in the packed bed and to characterize the internal morphology, we leverage data obtained from neutron computed tomography images of the dehydrated $SrBr_2$ composite (42 μm pixel size) at the MARS CG-1D beamline at High Flux Isotope Reactor at Oak Ridge National Laboratory. We used seeded watershed segmentation in Amira to estimate a porosity of $\varepsilon = 50\%$ (Section B.4 and Fig. B.2). Based on the measured mass loaded within a known volume of the reactor, the effective/bulk density of the solid phase in the reactor is deduced as $\rho_{\text{bulk}} = 310$ kg/m^3. Based on this the intrinsic density of the composite is determined as $\rho_{\text{s}} = \rho_{\text{bulk}}/(1-\varepsilon) = 620$ kg/m^3.

A primary use-case for these comparisons is to provide insights on the sensitivity of model parameters to the deviations between model predictions and experimental values. In this regard, the kinetic rate constant, and therefore the pre-factor term, K^* (Eq. 4.2) turns out to be very sensitive to the predicted results. To determine best-fit K^* values based on comparisons with reactor-scale measurements, the root mean square error (RMSE) (Eq. 4.16) between predictions and measurements is minimized.

$$\mathrm{RMSE} = \sqrt{\frac{1}{N}\sum_{i=1}^{N}\left(y_{\mathrm{exp},i} - y_{\mathrm{model},i}\right)^2} \tag{4.16}$$

where y_{exp} is the experimentally observed data point and y_{model} is the model prediction at that same point in time. This RMSE value is calculated and averaged over time for both temperature and water vapor concentration at the outlet throughout the duration of each experiment.

4.3 Results and Discussion

4.3.1 Model predictions for reactor-scale thermochemical performance

Fig. 4.2 explores the role that kinetics and mass transport, captured by the Damkohler number, Da, play on the thermal and chemical performance during hydration for pure K_2CO_3 in a packed bed reactor with $L = 0.125$ m. While the results presented and discussed are specific to the salt and reactor design considered, the general trends are broadly applicable for any thermochemical material, with the exact transition points in Da being tied to salt-specific kinetics and other design/operational parameters (Table 4.1). Results are presented for: (i) the mass transport limited case with $Da = 3.10$ (Fig. 4.2a–d) and (ii) kinetics limited case with $Da = 0.77$ (Fig. 4.2e–h). To traverse this Damkohler number transition we artificially modify the kinetic pre-factor, K^*, in Eq. 4.2 , to $K^* = 2$ and $K^* = 0.5$. Stoichiometric calculations based on materials-scale kinetic parameters for K_2CO_3, suggest that the hydration would be fully complete in about 115 min. Therefore, we compare these two cases for 120 mins of total simulation time.

For the mass transport limited case with $Da = 3.10$ ($K^* = 2$), the rate of the reaction is mainly restricted by the availability of water vapor. This regime is marked by a rapid rise in temperature and fall in water vapor concentration (Fig. 4.2a,b) along the flow direction, before leveling off near the reactor outlet. For all times $t \leq 90$ min, the outlet air temperature

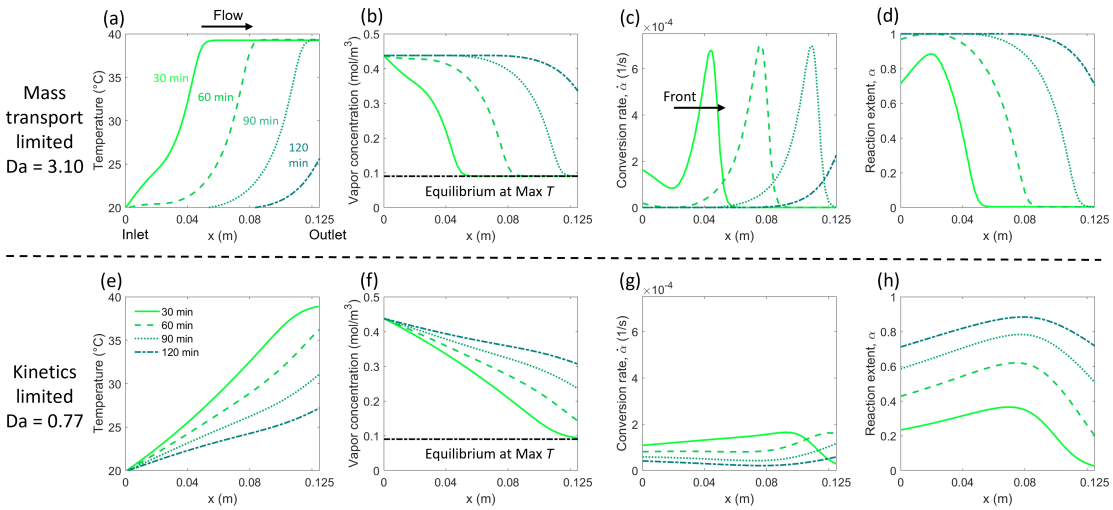


Figure 4.2: Model predictions for a packed bed of K_2CO_3 particles with (a-d) mass transport limited, kinetic pre-factor of $K^* = 2.0$, and (e-h) kinetically limited with $K^* = 0.5$ conditions. Profiles are shown at 30, 60, 90, and 120 minutes for (a,e) temperature, (b,f) water vapor concentration, (c,g) fractional hydration rate, and (d,h) fractional hydration extent. Baseline model parameters are modeled with $\varepsilon = 0.6$, $RH_{\text{in}} = 45\%$, $\vec{u} = 0.5$ m/s, $L = 0.125$ m, $T_{\text{in}} = 20$°C. Equilibrium at Max T line indicates equilibrium vapor concentration corresponding to the maximum temperature predicted.

rises steadily by over 18°C from the inlet, and the water vapor concentration reaches the equilibrium vapor concentration based on the maximum temperature lift possible for the given inlet conditions. This steady outlet air temperature translates to a steady thermal power produced during discharge. At $t = 120$ min (Fig. 4.2a), the rise in temperature is curtailed to about 5°C, resulting in a drop-off in the thermal power discharged. Consistent with prior work ([169, 104, 72]), the spatial profile of the hydration rate (Fig. 4.2c) exhibits a moving wave front, where the peak reaction rate continuously shifts from the inlet to the outlet with time. Correspondingly, the salts present near the inlet are the first to get fully hydrated, i.e., reaction extent is 1 (Fig. 4.2d), and hydration extents increase with time towards the reactor outlet. The local peak in the hydration rate is dictated by competing driving forces along the flow direction (Eq. 4.2). From the inlet to the outlet, the excess vapor concentration beyond the temperature-dependent equilibrium concentration $(1 - \frac{p_{\text{eq}}}{p_{\text{f}}})$ decreases as the salt consumes water vapor, whereas, the Arrhenius contribution to the reaction rate $(exp(-E_{\text{a}}/RT))$ and fraction of the salt (i.e., $1-\alpha$) that remains to be hydrated increases. The mass flow rate of the reacting water vapor dictates how sharp the moving reaction front is (Fig. 4.2c). At slower mass flow rates and equivalently larger Da values ($>> 1$), the outlet temperature and therefore thermal power discharged is constant for a longer amount of time, at the expense of a smaller magnitude.

Fig. 4.2e–h tracks the performance for kinetically limited operating conditions, with $Da = 0.77$, ($K^* = 0.5$). While temperature and water vapor concentration change steeply (Fig. 4.2a,b) in the transport limited regime, more gradual and linear changes (Fig. 4.2e,f) are predicted in the kinetics limited regime. Moreover, for $t \leq 90$ min, the near-steady air outlet temperature and thermal discharge power is replaced with a decreasing trend. Even though there are competing spatial variations in the excess water vapor available to react and the fraction of salt that remains to be hydrated (Figs. 4.2f,h), these effects are more subdued than in the mass transport limited regime. Therefore, reaction rate decreases (Fig. 4.2g) as the fraction of hydrated salts increases (Fig. 4.2h) throughout the reactor volume with time. The shifting outlet air temperature and therefore the related power output indicates the need for an integrated control system that tunes operating conditions to better match power demand [187]. Distinct from the transport limited case where more than 97% of the salt on average gets hydrated (Fig. 4.2d), for the kinetics limited case the spatially-averaged reaction extent is only about 82% (Fig. 4.2h) over 120 mins, which indicates that slow kinetics can severely impede material utilization in the reactor.

Overall, Da serves as an effective dimensionless quantity to relate transport and kinetic limitations with thermochemical performance. Fig. 4.2 presents results that are both close to $Da = 1$ ($Da = 3.10$ and $Da = 0.77$). Therefore, these results are influenced by both transport and kinetic limitations. For $Da >> 1$, where mass transport of reactants is more severely limited, the moving wave fronts will become sharper than in Fig. 4.2c since only a small region of the bed is active at any time and result in nearly 100% of the salt bed being hydrated within 120 min. Whereas, for $Da << 1$ in the fully kinetically limited regime, the reaction rate profiles will become more flat than in Fig. 4.2g, resulting in increasingly lower fractions of the salt being hydrated over the same duration until the kinetic limit is reached.

4.3.2 Specific power and energy relationships with the Damkohler number

Figs. 4.3a,b translate the effects of the Damkohler number, Da, from the spatio-temporal predictions in Fig. 4.2 to tradeoffs in the mass-specific power output and energy capacity, i.e., Ragone plots. Power and energy are normalized by the masses of the dehydrated salt present; for the composite the total mass of the salt and the vermiculite host is taken into account. For these results, hydration reactions are modeled in both pure K_2CO_3 and $SrBr_2$ composite salts, and with base model parameters listed in Table 4.1 with a range of inlet air flow velocities, $\vec{u} = 0.013 - 2$ m/s (Section 4.2.1).

As we traverse from 0 to the maximum specific energy capacity in Fig. 4.3a,b, the

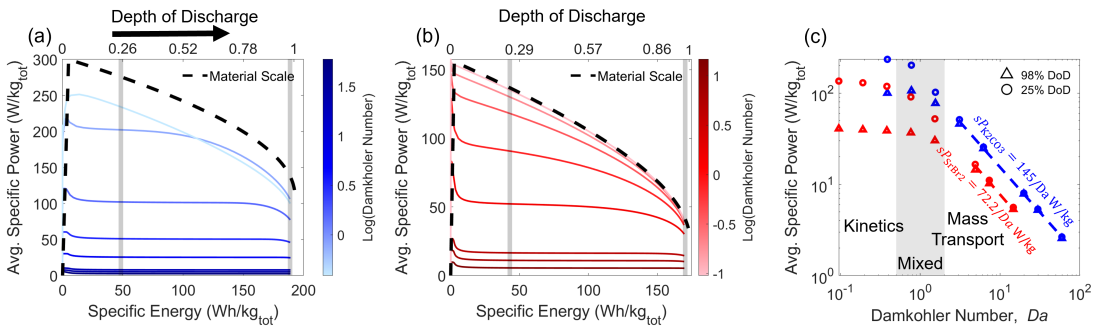


Figure 4.3: Ragone plots based on model predictions for packed bed reactor hydration with $\varepsilon = 0.6$, $RH_{\text{in}} = 45\%$, $L = 0.125$ m, $T_{\text{in}} = 20°\text{C}$, $K^* = 1$ with velocities: $\vec{u} = 0.013 - 2\text{m/s}$ for (a) K_2CO_3 and (b) $SrBr_2$ composite ($\Delta H_{\text{rx}} = 3.35$ MJ/kg$_{\text{H2O}}$). Discharge is from left to right and shaded lines indicate 25% and 98% depth of discharge (DoD). (c) Average specific power at 25% and 98% depth of discharge vs Damkohler number, Da, for both salts. Shaded region shows mass transport to kinetic transition between $2 \leq Da \leq 0.5$. Fit shown is for data points when Da > 2.

depth of discharge of the thermochemical reactor increases from 0 to 1. As Da increases, we transition from kinetic to mass transport limitations, with reactor-scale performance eventually approaching materials-scale test data. For both salts, the specific power output during discharge is smaller for large Da values, because slower air flow rates lead to slower transport of the reacting moisture to the salt. Fig. 4.3c depicts the dependence of output power densities on the Da number for two depths of discharge – 25% and 98% to represent reactor performance at early and late times respectively. At high Da both early and late specific power match indicating constant power output throughout the vast majority of the discharge. As Da decreases, the specific power increases linearly until $Da \sim 1$, and can be analytically predicted, $sP_{\text{SrBr2}} = 72.2/Da$ W/kg and $sP_{\text{K2CO3}} = 145/Da$ W/kg, when $Da \geq 2$ (Fig. 4.3c). When Da falls below 1, there is an increasing deviation between the early and late reactor performance, because in the kinetics limited regime the reaction rate slows down when there is less salt left to react (Eq. 4.2). As Da continues to decrease, larger deviations from the linear relationship occur with specific powers eventually leveling off to intrinsic kinetic limitations for sufficiently small Da.

The Da values are larger for K_2CO_3 compared to the $SrBr_2$ composite at equivalent air flow velocity, inlet humidity, and reactor dimensions. This effect is attributed to the much larger density of the reactive material in the pure salt versus the composite (250% higher) and the smaller equilibrium vapor pressure, which results in a larger vapor pressure driving force $(1 - p_{\text{eq}}/p_{\text{f}})$ at the inlet, despite the slightly smaller kinetic pre-factor (8% lower $C_0 exp\left(-\frac{E_a}{RT}\right)$ at inlet conditions for K_2CO_3). These differences contribute to the maximum specific power

of K_2CO_3 more than doubling compared to the $SrBr_2$ composite (300 W/kg versus 140 W/kg), even though their specific energy capacities values are comparable (193 Wh/kg versus 174 Wh/kg (Table 4.1)). Particularly, the larger vapor pressure driving force leads to nonlinear differences in the reaction rate and the rate of heat released during hydration, which can further amplify the differences in the outlet air temperature and the specific power. Fig. B.4 shows how K_2CO_3 has a higher peak outlet temperature and faster discharge time at equivalent Da ($Da = 0.38$) than $SrBr_2$ composite due to these effects.The same factors are also likely why there is a relatively larger rate of decrease in specific power with increase in Da in the linear, mass transport limited region for K_2CO_3 (Fig. 4.3c).

Results in Fig. 4.3 are further interpreted and related to typical demands in terms of power densities (W/kg) for long term or seasonal storage (> 100 hours) versus daily load shifting (4-8 hours). The mass transport limited regime with $Da \gg 1$ results in a constant output temperature with low specific power densities, and therefore amenable for long-term storage applications ($\leq$ 1 W/kg). Whereas, the kinetically limited operation with $Da < 1$ can yield high power densities needed for the high power and daily load shifting applications ($\sim$ 20-100+ W/kg) with the ceiling in specific power coupled to intrinsic material kinetics [87, 81]. Therefore, materials and reactor design, and operating conditions should be optimized towards attaining smaller Da values to maximize specific power output during thermal discharge. However, these changes to Da will also secondarily influence parasitic pumping and humidification energy costs (Section 4.3.3).

Overall, these results showcase a powerful, reduced-order relationship between the specific thermal power discharged (W/kg) and the Damkohler number. Especially, in the mass transport limited regime, the specific power is inversely related to Da, with a salt-specific proportionality constant. Performance limiting factors can be classified if they arise due to intrinsic kinetics, mass transport, or influences from both in the mixed regime. More significantly, we can make *a priori* estimates of the specific power during discharge/charge for thermochemical storage systems with knowledge of the inlet state of air (temperature, vapor pressure), reactor design and operating conditions, and materials-specific kinetics and thermodynamic parameters. This yields the simplicity of tracking and mapping performance predictions with changes in materials as well as reactor design and operating parameters. However, to better collapse the data for specific power across different materials, a more expansive set of dimensionless quantities need to be considered beyond just the Da number, to account for compounded effects of spatial variations in temperature, concentration and reaction rates on the specific power that are not fully captured from a Da number just based on the inlet state (Eq. 4.7).

While Fig. 4.3 is generated by varying inlet velocity, other parameters can also change

Da. Fig. B.3a shows the Ragone plot for variable reactor length, and this exactly matches results in Fig. 4.3 for the same Da. However, due to changes in the maximum temperature lift at different inlet relative humidity, the RH_{in} and inlet velocity plots no longer exactly match for equivalent Da (Fig. B.3b), but the trends and the order-of-magnitude in the variation of specific power with Da are still similar.

4.3.3 Parasitic loads can be substantial

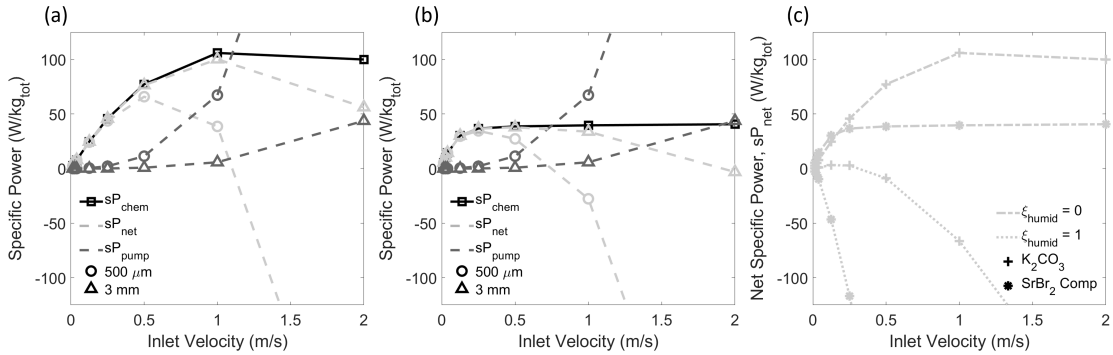


Figure 4.4: Influence of inlet air velocity on parasitic pumping power requirements, sP_{pump}, with (a) K_2CO_3 and (b) $SrBr_2$ composite at 500 μm and 3 mm particle sizes, where sP_{chem} is the model predicted average thermochemical power from hydration reactions at 98% depth of discharge for varying velocities and the same as $\overline{sP}_{\text{chem, model}}$ (Eq. 4.10), and sP_{net} is the net specific power which discounts pumping power, sP_{pump}, from the thermochemical power produced, sP_{chem}.(c) Impact of moisture supply fraction, ξ_{humid}, on the net specific power, sP_{chem}, which discounts the humidification power load, sP_{humid} (Eq. 4.15), from the thermochemical power produced, sP_{chem} for varying velocities for both salts. Model cases are for $\varepsilon = 0.6$, $RH_{\text{in}} = 45\%$, $L = 0.125$ m, $T_{\text{in}} = 20°\text{C}$, $K^* = 1$, and $\Delta H_{\text{rx,SrBr2}} = 3.35$ $\text{MJ/kg}_{\text{H2O}}$ with air inlet velocities: $\vec{u} = 0.013 - 2\text{m/s}$.

Fig. 4.3 shows the maximum thermal power discharged from hydration reactions. However, pumping (Eq. 4.14) and producing a controlled humid stream (Eq. 4.15) require additional energy inputs. Fig. 4.4a,b shows the maximum thermochemical average power at the end of discharge (98% depth of discharge) produced based on model predictions ($\overline{sP}_{\text{chem, model}}$, Eq. 4.10), the pumping power (sP_{pump}, Eq. 4.14), and a net power, sP_{net}, produced that discounts sP_{pump} from $\overline{sP}_{\text{chem, model}}$ for two different characteristic particle sizes of $d_{\text{p}} = 500$ μm and 3 mm in the packed bed, and for both materials. In both cases, the pumping power is negligible ($< 2\%$ of output power) at and below $\vec{u} = 0.125$ m/s for $d_{\text{p}} = 500$ μm. However, since pumping power increases dramatically with velocity ($\propto v^3$), when the air flow velocity increases beyond 1 m/s for the $SrBr_2$ composite 500 μm case (Fig. 4.4b), pumping power requirements become larger than power output from the ther-

mochemical reactor. Because of the competing effects of flow velocity on the thermal power discharged and the pumping power, an optimum air flow velocity maximizes the net power produced [176]. Optimum flow velocities of $\vec{u} = 0.5$ m/s, and $\vec{u} = 0.25$ m/s is obtained for the K_2CO_3 and $SrBr_2$ composite respectively, where the pumping amounts to 15% and 7% of the thermal power discharged due to hydration reactions. When the particle size increases to that of the vermiculite matrix material (d_p= 3 mm) used for our experiments with $SrBr_2$ composite (Section 4.2.4), the contribution from pumping decreases by nearly an order of magnitude. This provides the advantage of net positive power production during operation at even higher flow rates (Fig. 4.4a,b), and the optimal velocity shifts to larger values, similar to what is reported in [176]. Therefore, millimeter-sized, porous particles/pellets can be promising from a reactor design standpoint, especially for axial flow reactors, as it balances low parasitic pumping energy with high surface area from intra- and inter-particle fluid phase porosity.

Humidification: Fig. 4.4c shows the net power output when accounting for the humidification load, sP_{humid} (Eq. 4.15), based on the same model results of Fig. 4.3 (Fig. 4.4c ignores pumping power requirements). At $\xi_{\text{humid}} = 0$ moisture supply fraction, the net capacity equals the thermodynamic salt reaction enthalpy with full capacity, which can occur such as when sourcing 12 mbar of vapor pressure from a ground borehole at 10°C [66]. If all moisture must be externally generated, $\xi_{\text{humid}} = 1$, with no regeneration, [81], negative net powers can occur. Although the enthalpy of vaporization of water is lower than the reaction enthalpy of the salt hydrates tested, since the hydration reaction only occurs until p_{eq} a significant portion of the generated water vapor is not consumed. Even in the mass transport limited regime case of $\vec{u} = 0.013$ m/s where p_{eq} is reached, the net power output for K_2CO_3 is reduced to 13% of $\overline{sP}_{\text{chem, model}}$ with $SrBr_2$ composite having a negative sP_{net}. At higher inlet velocities in the kinetically limited regime this effect is compounded with large negative net powers since an even smaller fraction of generated incoming moisture reacts (Fig. 4.2b,f). This points to the need to utilize a free moisture source from the ambient or from boreholes to reduce ξ_{humid} and/or recycle moisture released during dehydration although these strategies may be limited and can add cost to the system [81]. Since this study focuses on reactor design and not climate, when comparing the performance of different materials and systems, the parasitics due to both pumping and moisture generation are not reported in the rest of the analyses.

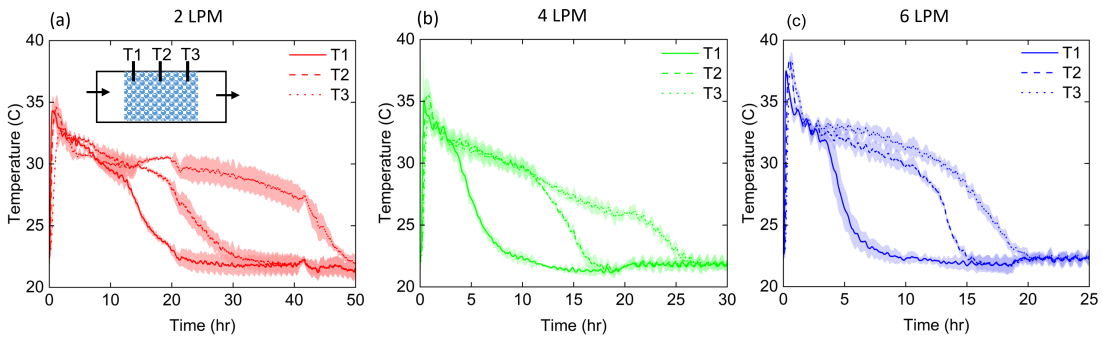


Figure 4.5: Spatial and temporal variation of air temperature in the experimental packed bed reactor with $SrBr_2$ composite with the inlet air at 22°C and a fixed relative humidity of 45% RH_{in} for air flow rates of (a) 2 LPM, (b) 4 LPM, (c) 6 LPM. Inset shows thermocouple T1, T2 and T3 locations inside reactor. Shaded color regions are standard deviations obtained from 3 independent experimental trials.

4.3.4 Insights from comparative assessment of reactor-scale measurements and model predictions

Fig. 4.5 reveals experimentally obtained spatio-temporal temperature profiles in the $SrBr_2$ composite for 3 different air flow rates of 2, 4 and 6 standard liters per minute (LPM), all with a fixed inlet relative humidity of 45%. All the flow rates tested exhibit a steep rise in the air temperature across the most of the length of the bed within the first hour of the hydration reaction. This initial peak coincides with thermal characteristics measured with pure vermiculite at equivalent conditions (Fig. B.5). However, this temperature rise drops off quickly (within 2 hrs at 2 LPM and 1 hr at 6 LPM) for the pure vermiculite in contrast to the gradually changing temperatures with the composite materials. These trends are suggestive of faster rates, but smaller thermal capacity for water vapor uptake (10% of total energy at 6 LPM) by the pure vermiculite as compared to the composite salt, and consistent with hydration extents reported in prior work with vermiculite [99]. At all flow rates, the salts present in the reactor near the inlet (represented by T1) is the fastest to hydrate and therefore results in an early drop off in temperature. Subsequently, hydration starts to occur further downstream from the inlet, which results in the temperatures in the midsection (T2) and near the outlet to also decreasing at later times (T3). For instance, in the case of 2 LPM, T1 begins dropping off at 12 hours, T2 at 20 hours, and T3 at 40 hours with each location taking several hours before finally returning to the inlet temperature. Comparing the three different flow rates, the moving reaction front behavior accompanied by a consistently shifting peak temperature value, is most pronounced for the case of 2 LPM, confirming larger mass transport limitations for the slower flow rates (Fig. 4.2a). The reaction rate significantly

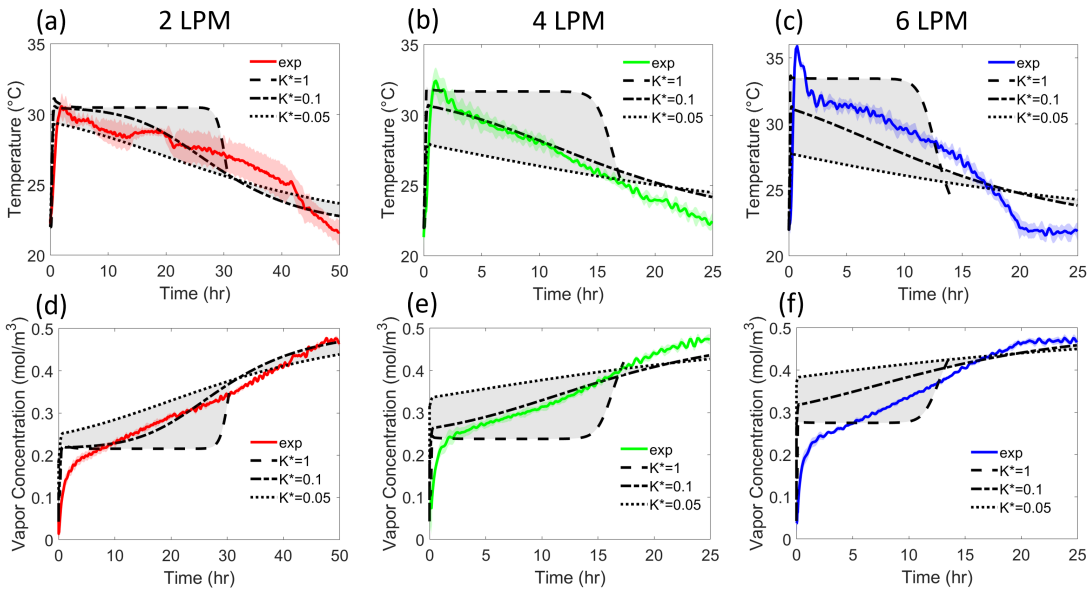


Figure 4.6: Comparison of $SrBr_2$ composite experimental reactor (labeled as exp) with model predictions at different flow rates and as a function of kinetic pre-factor, K^* values modeled for the (a-c) outlet temperature and (d-f) outlet water vapor concentration. Shaded color regions are standard deviations across 3 trials. Model assumes $\varepsilon = 0.5$, $RH_{\text{in}} = 45\%$, $L = 0.125$ m, $T_{\text{in}} = 22°\text{C}$, $\rho_{\text{s}} = 620$ kg/m^3. $\Delta H_{\text{rx}} = 1.95$, 2.42, 3.35 MJ/kg$_{\text{H2O}}$ for 2, 4, and 6 LPM cases respectively.

slows down and all the measured temperatures have returned to the inlet state (marked by 98% hydration) after $t = 50$, 25, and 20 hours for the 2, 4, and 6 LPM respectively. From 2 to 4 LPM, we see that discharge time halves indicating a proportional increase with Da (Fig. 4.3c). If the proportional response continues we would expect the 6 LPM hydration to finish in 16.7 hours instead of the reported 20 hours suggesting that the non-linear Da versus specific power regime of Fig. 4.3c has been reached. This suggests that the 6 LPM is more limited by kinetics, whereas the 2 LPM is more strongly affected by mass transport limitations. Overall, these results indicate operation in the mixed regime where increases in flow rate can still improve specific power output even though the temperature profile no longer plateaus as expected in the mass transport limited regime (Fig. 4.5).

Fig. 4.6 presents a comparison of the outlet temperature and water vapor concentrations between measurements and model predictions. Broadly trends in the outlet air temperature with time and the air flow rate are similar to those presented within the bed (Fig. 4.5). The magnitude of the peak outlet temperature increases with increase in the air flow rate, from 30°C to 35°C for 2 and 6 LPM air flow rates. However, it also drops back faster to the inlet temperature for the faster flow rate. This is consistent with the increased rate of

hydration and the associated heat release, and the rapidly declining power density (Fig. 4.3) with increase in air flow rate. In contrast to the outlet temperature, which rises in the first hour of hydrating the material, the outlet water vapor concentration (Fig. 4.6d-f) is nearly fully depleted instantaneously (< 30 s), and therefore the outlet water vapor concentration rapidly reaches its minimum value before slowly rising back to the inlet vapor concentration of 0.49 mol/m^3. As the hydration reaction progresses, more of the salt in the reactor has undergone full hydration, and consequently, the moisture content increases with time at the outlet, similar to what is expected in the kinetics limited regime (Fig. 4.2f) again suggesting increased kinetic limitations as the flow rate increases.

The same model as described in Section 4.3.2 with the $SrBr_2$ composite is applied (Fig. 4.3), but with experimentally deduced values for the bed porosity, reaction enthalpy, and the inlet temperature. Amongst the many input parameters to the model, the kinetic pre-factor, K^* can have large uncertainties, and the model predictions are found to be highly sensitivity to this parameter, and Fig. 4.6 shows these effects. Using a baseline value for the kinetic pre-factor, $K^* = 1$ over-predicts the outlet temperature and under-predicts the outlet vapor concentration for all the flow rates, ($RMSE_{\text{avg}}$ = 2.51°C, 0.063 mol/m^3). When the kinetic pre-factor is reduced to $K^* = 0.1$, both the initial peak temperature and the transient temperature profile fits improve dramatically ($RMSE_{\text{avg, T}}$ = 1.46°C). Similarly, the shape of the outlet vapor concentration is also better captured, even though the RMSE values are comparable to K*=1 ($RMSE_{\text{avg, c}}$= 0.063 mol/m^3). The errors in the predicted outlet temperature and vapor concentration increases when the kinetic pre-factor is further reduced to $K^* = 0.05$, resulting in $RMSE_{\text{avg}}$ = 1.99°C, 0.107 mol/m^3. Therefore from the 3 values of pre-factors that are modeled, $K^* = 0.1$ results in the best fits for predicting the outlet temperatures and water vapor concentrations. While the rate of change in the outlet temperature and the water vapor concentration increases in the experimental dataset towards the end of the hydration reaction, this has a decreasing trend in the model predictions (Fig. 4.6). Possible reasons for this stems from differences in the total thermal mass modeled (including reactor walls, insulation, etc.) versus what actually contributes to the experimental measurements. When $K^* = 0.1$, the resulting Da values are 1.80, 0.90, and 0.60, for air flow rates of 2, 4, and 6 LPM, respectively.

The discrepancy in the best-fit values for the kinetic rate pre-factor between the reactor-scale ($\sim$ 100 g of composite) and materials-scale ($\sim$ 1 g of composite) measurements is attributed to several factors. The materials-scale kinetic measurements are only conducted at room temperature for two different relative humidity with temperature dependent terms based on the pure salt. If the temperature dependence of p_{eq} and kinetic pre-factor of the composite is different than the pure salt this uncertainty could have a significant impact on

the driving forces for hydration. Additionally, there are differences in the specific surface area available for reactions between the materials-scale and the reactor-scale tests. Since this is a heterogeneous gas-solid reaction, rate constants should be normalized to the reacting surface area of the particles. While the materials-scale tests are performed with air flow over a thin layer of a loosely packed bed at the reactor-scale the bed is more tightly packed. Another factor is that based on theoretical densities and salt loading ratios, pure $SrBr_2$ is expected to swell 119% from $SrBr_2 \cdot 1H_2O$ to $SrBr_2 \cdot 6H_2O$ [188]. This effect has been previously reported by measuring almost an order of magnitude reduction in the bed permeability during hydration with pure $SrBr_2$ materials [87]. Although the extent of swelling is expected to be lower with the impregnated salt in the composite materials, if present to even a moderate extent, it can cause differences in the specific surface area for the materials- and the reactor-scale measurements. On this regard, even though neutron tomography reveals a well connected-pore network for the dehydrated $SrBr_2$ composite with multiscale pores (Fig. B.2), during hydration some of the smaller channels could close reducing the exposed surface area. To isolate specific contributions requires more extensive parametric explorations and control measurements, such as measurements of surface area before and after hydration and a temperature dependent thermogravimetric analysis study for improved rate/equilibrium equation estimates.

Fig. 4.7 compares the experimental and model predictions for the packed bed reactor in a Ragone plot. These results are largely consistent with our earlier predictions (Fig. 4.3a), where the specific power increases with increasing air flow rate. The model ignores contributions from the vermiculite, so the initial peak in the specific power is underestimated even with the best-fit values for the kinetic parameters. Better fits are likely to be achievable for salts operating in the mass transport limited regime without a reactive host [90, 103]. The deviations between model and experiment for the specific energy capacities is minimal and largely within the experimental trial-to-trial and systematic uncertainties (Table B.2). For instance, the mass of the active material loaded in the reactor changes slightly in every trial, whereas a constant packed bed porosity is modeled for all the cases in Fig. 4.7.

Unlike the results in Fig. 4.3, the measured specific energy capacity effectively increases with flow rate, because of the reduction in the fractional heat losses (Section B.7). For the 2 LPM case, the experimental results output a relatively constant power density of 2.5 W/kg owing to operation largely in the mass transport limited regime ($Da \sim 1.80$) based on the best fit of $K^* = 0.1$ kinetic pre-factor. When the flow rate increases to 6 LPM, maximum specific power reaches 11 W/kg before decreasing to a final specific power of 9 W/kg, with this decline with reaction extent again tracking with operating in the largely kinetics limited regime ($Da \sim 0.60$). At 6 LPM, a specific energy of 164 Wh/kg is reached, which is within

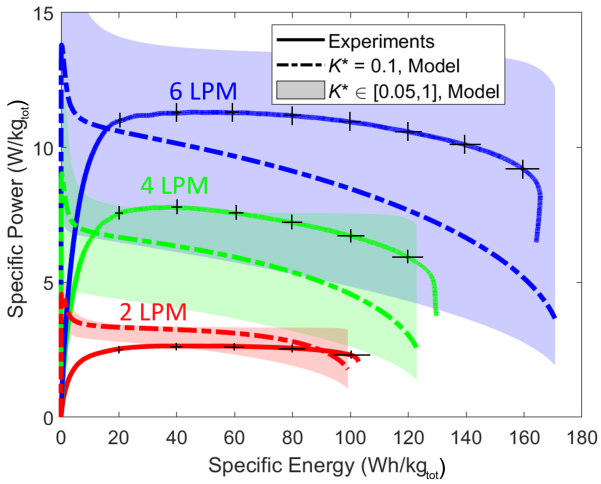


Figure 4.7: Experimental and model predictions for the Ragone plot at 2, 4, and 6 LPM for the packed bed reactor with $SrBr_2$ composite. Shaded region represents bounds of model results for kinetic pre-factors of $K^* = 1$ and $K^* = 0.05$. Error bars represent experimental uncertainty in specific power and specific energy at select points. Model assumes $\varepsilon = 0.5$, $RH_{\text{in}} = 45\%$, $L = 0.125$ m, $T_{\text{in}} = 22°\text{C}$, $\rho_s = 620$ kg/m^3. $\Delta H_{\text{rx}} = 1.95$, 2.42, 3.35 MJ/kg$_{\text{H2O}}$ for 2, 4, and 6 LPM cases respectively.

6% of the theoretical capacity of the $SrBr_2$ composite indicating a near complete reaction. This is also supported by the assessment that close to the theoretical mass of water vapor is being taken up (Section B.5).

Fig. 4.7 shows that the kinetic pre-factor term, K^*, has a large impact on the tradeoffs between specific power and energy, similar to predictions in Fig. 4.6. The sensitivity of the power output to K^* increases with flow rate and as kinetic limitations become more dominant. Comparisons at later depths of discharge are more meaningful since a significant portion of initial power produced in the experiment goes into sensibly heating salt particles and reactor walls rather than increasing outlet temperature. This results in the model over-predicting early power output since the model directly tracks reaction rate. For all 3 flow rates, $K^* = 1$ over-predicts and $K^* = 0.1$ and $K^* = 0.05$ under-predict suggesting the true reaction kinetics are within these bounds. With the best-fit $K^* = 0.1$, the deviation at 98% of depth of discharge is -59% for 6 LPM versus -22% for 2 LPM. Additional cases are modeled by fixing the kinetic pre-factor term at $K^* = 1$, and instead varying the bed porosity between 0.35-0.65, which is well outside the experimental uncertaintyof $\pm$ 5%. For the baseline porosity of 0.5 and 6 LPM air flow rate, the deviation between experimental data and model prediction at 98% depth of discharge is 33%. With the lowest porosity ($\varepsilon = 0.35$) this deviation improves to 19% while worsening to 101% for the highest porosity

($\varepsilon = 0.65$). Overall, these sensitivity analyses indicate that changes and uncertainties in kinetic parameters and porosity can play a significant role in determining power output.

4.3.5 Benchmarking thermochemical performance of salt hydrates using Ragone framework

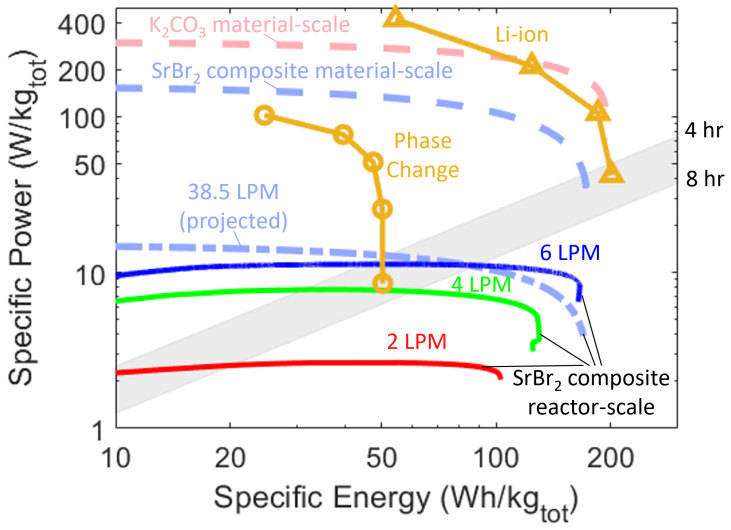


Figure 4.8: Ragone plot comparison of different energy storage devices. $SrBr_2$ composite material-scale is generated from this study and K_2CO_3 material-scale data is sourced from Geaini et al. [4]. 2, 4, and 6 LPM curves are from experiments from this study for $SrBr_2$ composite reactor. The 38.5 LPM (projected) case represents the maximum power output for the $SrBr_2$ composite reactor based on the best fit kinetic pre-factor of $K^* = 0.1$. Li-ion cell reference data is for a voltage cut-off of 3.5 V (triangles), and phase change reference is for n-tetradecane/graphite composite slab with cut-off temperature of 12°C (circles) [5]. Shaded region represents load shifting between 4 and 8 hours.

Fig. 4.8 comparatively evaluates salt hydrates at the materials- and reactor-scale with other energy storage materials/systems by applying the Ragone framework, similar to the analysis highlighted by Woods et al. [5]. Specific power based on discharging the specific capacity for duration of 4 and 8 hours is highlighted for the use-case of typical peak load shifting. Specifically, for buildings applications the U.S. Department of Energy (DOE) has set targets to shift half of building heating and cooling loads by utilizing $\geq 95\%$ of the thermal energy system capacity. [85]. For the $LiCoO_2$/graphite cell battery, experimental cell-data reported in ref. [189] is used with an assumed specific energy capacity of 200 Wh/kg, and with a cutoff voltage of 3.5 V (i.e., the voltage at which the battery can no longer output useful work). Each point represents a different constant current discharge profile with specific

energy calculated when the voltage drops below the voltage cutoff as reported in Woods et al. [5]. Experimental data obtained for a tetradecane/graphite composite slab cooling down glycol liquid to be below 12°C by Woods et al. is additionally included. Varying the glycol flow rate changes the accessible specific energy, and this generated the dataset in Fig. 4.8.

At the materials-scale, K_2CO_3 follows the Li-ion battery performance in both specific power and energy, and has the potential to provide specific power outputs that far exceed the 4 hour load shifting target. In comparison, the maximum specific power of the $SrBr_2$ vermiculite composite is half that of K_2CO_3, due to the 1:1 mass ratio of the largely inert vermiculite host with that of the active $SrBr_2$ salt. However, the $SrBr_2$ vermiculite composite can still almost completely discharge within 4 hours and reach a specific energy that is 86% of the Li-ion cell, and threefold larger than the composite phase change slab.

At the reactor-scale, for the $SrBr_2$ vermiculite composite, the maximum specific energy that can be accessed exceeds those of phase change materials (at least 104% larger), and approaches the materials-scale values for the largest air flow rate tested. However, the specific power discharged is more severely hindered as compared to Li-ion cells, phase change composite slabs, and even its own performance at the materials-scale. A maximum specific power of 11 W/kg is achieved at the highest air flow rate of 6 LPM, and slowly drops by 18% to 9 W/kg at a final specific energy of 160 Wh/kg. Over an 8 hour discharge duration, 90 Wh/kg of the stored thermochemical energy is utilized, which is still 80% larger compared to the phase change material. At 2 LPM, specific power becomes even smaller, and only 10 Wh/kg and 20 Wh/kg of the 100 Wh/kg can be accessed within 4 hours and 8 hours respectively, which fares worse than the 50 Wh/kg capacity of the composite phase change slab. The 6 LPM ($\vec{u} = 0.039$ m/s) experiment suggests operation already in the kinetically limited regime ($Da \sim 0.6$) (Section 4.3.4). Therefore, we expect minimal improvements in specific power output with any further increase in the air flow rate (Fig. 4.3c). This is further confirmed by using our model to project the performance of this reactor at even larger flow rates by using the best-fit kinetic pre-factor of $K^* = 0.1$ leading to $Da < 0.1$. Even with a sixfold increase in air flow rate of 38.5 LPM ($\vec{u} = 0.25$ m/s and $Da = 0.094$), the maximum specific thermochemical power output at the end of discharge does not increase compared to the 6 LPM case.

Overall, this suggests that the 50 wt%-50 wt% $SrBr_2$ vermiculite composite, while still promising at the materials-scale, struggles to achieve the U.S. DOE target of 4 hours of peak load shifting while utilizing >95% of its capacity. This is largely attributed to the apparent reduction in the kinetics at the reactor-scale as compared to the materials-scale (Section 4.3.4), and underscores that size/length-scale dependent performance discrepancies in thermochemical materials are important to pay attention to [97], akin to results demon-

strated previously for phase change materials [190]. While the Ragone plots reported in this paper are gravimetric energy and power densities, volumetric energy and power (kWh/m^3 and kW/m^3) quantities can also be obtained, which will become pertinent in applications where the space requirement is a constraint.

4.3.6 Perspectives and Outlook

For all the model predictions and experiments reported in this study, inlet air is at room temperature, entering with a fixed inlet relative humidity of 45% RH_{in}, and with a 1:1 mass loading for both the active salt and the inert and porous vermiculite host material. A sure shot approach to improve specific power from the hydration reactions is to increase the inlet air relative humidity (Eq. 4.2). Increasing RH_{in} from 45% to 60% raises power output by 16% (Fig. B.3b), but this strategy has limits since 60% RH is likely above the composite's deliquescence point. Additional constraints on the inlet relative humidity stems from the parasitic latent heat requirements to produce water vapor (Section 4.3.3). Increasing the active salt fraction to greater than the 50 wt% examined in this study presents another approach to improve the specific power. At higher salt fractions both specific power and energy should increase. However, depending on the pore size and morphology of the host material, the salt can start to block the porous structure beyond an optimal threshold to result in a reduction of reaction rates, and therefore specific power [97]. Increasing the inlet air temperature, would overall rise temperatures everywhere, which can improve reaction rates by exponentially lowering the activation barrier. However, a competing effect arises from the reduction in the chemical driving force based on the excess water vapor concentration compared to equilibrium conditions (Eq. 4.2). While the effect of temperature is better captured for dehydration reactions based on thermogravimmetric measurements at the materials-scale, these have not been as extensively characterized during hydration, especially at the reactor-scale. Additional reactor design strategies that can improve performance include consideration of radial flow reactors to minimize pressure drops [191], and also the consideration of composite/porous host designs and morphologies that enable reversible swelling without blocking of vapor diffusion pathways during hydration [97]. Moreover, future work should explore dynamically altering the inlet conditions, including the humid air flow rate and its thermodynamic state, to better match supply with heating demands. In this regard, Zhang et al. recently implemented a PID controller to control the inlet fluid velocity to extend the duration of steady output power delivered in a phase change system [187].

Ultimately, the viability of using salt hydrates for energy storage will depend on the

cost-per-kWh at the reactor-scale. While generic cost estimates for thermal energy storage materials/devices exist, technoeconomic analysis for salt hydrates is not that prevalent beyond the materials-scale and therefore should be pursued with urgency. Our calculations on parasitic energy requirements, underscore that energy needed for generating the "fuel" for the hydration reaction — water vapor, can be a sizeable fraction or even larger than the thermochemical power produced depending upon design/operating conditions (Fig. 4.4). Therefore, ongoing and future thermochemical reactor designs with salt hydrates should report these energy costs, and develop methods to recover moisture between the hydration and dehydration steps.

4.4 Conclusions

Our study focuses on theoretical and experimental performance assessments of thermochemical energy storage with salt hydrates, which can thermally discharge/charge by undergoing reversible reactions involving water uptake/release. Model results and measurements demonstrate the interplay of heat and mass transfer with chemical reactions on overall performance, and specifically quantify the tradeoffs between power and energy for high power, buildings heating applications. In a significant departure from prior work, we predict and characterize experimental performance at both the materials- and the reactor-scale with 1 g and 100 g active material masses respectively.

A transient, 2-D, multiphysics reactor model is developed and applied to predict the thermochemical performance of two leading salt hydrate materials — K_2CO_3 and $SrBr_2$ composite — under different operational regimes limited by mass transport and intrinsic reaction kinetics. Beyond predictions of spatiotemporal variations in pertinent parameters such as temperature, reaction extent, water vapor concentration, etc., a modified Damkohler number, Da, is shown to be an effective reduced-order parameter to generalize the dependency of the thermal power discharged on reactor design and operating conditions, and materials' thermodynamic and kinetic parameters. The specific power discharged is inversely proportional to this Damkohler number in the mass transport limited regime for $Da > 2$, whereas it becomes kinetically limited when $Da < 0.5$, and we observe a regime with mixed influences from both mass transport and kinetics when $0.5 < Da < 2$. Another major contribution of our work is to extend and apply the Ragone framework for salt hydrate reactors to quantify the tradeoffs in specific power and energy. To meet high power loads, reactors will be likely operated in the kinetically limited regime, which exhibits variable discharge power and diminishing effects in performance from altering reactor design and operating conditions such as air velocity and inlet humidity. This transfers the onus of improved performance on

improving materials synthesis/design (e.g., composite materials synthesis) and kinetics. In contrast, mass transport limited reactors operate at a constant, but low discharge power. Model predictions are used to project theoretical air flow rates with a fixed inlet humidity of 45% to attain material-scale power outputs. However, at very large inlet air flow rates parasitics for pumping and humidification can become larger than the thermochemical power output. Therefore, optimization of reactor design/operation while also accounting for the parasitic power consumption is critical.

Experimental materials- and reactor-scale testing is performed with packed beds of 50 wt%-50 wt% $SrBr_2$ composite with flow over and flow through configurations respectively. At the fastest flow rate of 6 LPM tested, which as per the model is already in the kinetically limited regime, the reactor achieved a peak specific power of 11 W/kg that slowly decreased to 9 W/kg at a final specific energy of 164 Wh/kg, which is more than 90% of theoretical capacity. The reactor-scale specific power is at least ten times smaller than the specific power predicted by the model using best-fit kinetic parameters deduced from materials-scale characterization. These differences are attributed to larger temperature gradients and morphological changes at the reactor-scale as compared to the materials-scale testing. Beyond direct comparisons between model predictions and measurements, the value of the model stems from the insights on the sensitivity of select model parameters on performance. Specifically, we find that the kinetic rate constant and the packed bed porosity modeled can both significantly influence thermochemical performance and how well model predictions match experimental datasets.

The Ragone framework is applied to benchmark and assess the promise of thermochemical energy storage with salt hydrates with Li-ion and phase change energy storage. While the salt hydrates demonstrate promisingly high specific power that are competitive even with Li-ion cells at the materials-scale, the comparisons dramatically change at the reactor-scale. Despite the reactor-scale specific energy being three times larger (164 Wh/kg) than a reference, paraffin wax based phase change heat exchanger device for cooling applications reported by Woods et al. [5], the amount of accessible specific energy becomes comparable for both cases with a typical target of 4 hours of peak load shifting. This underscores the dual need for developing composite materials with improved intrinsic kinetics and optimized reactor design/operating conditions to meet application-specific energy and power needs.

Combined, this study develops and establishes modeling and experimental methods and tools to guide the development of thermochemical energy storage materials and reactors with salt hydrates. The insights gained are especially catered towards meeting high power demands for building heating applications.

CHAPTER 5

Spatial Distributions of Hydration Cycling in Salt Hydrates using Neutron Imaging

Adapted in part from a manuscript under preparation: Kinzer, B., Zhang, Y., Bilheux, J., Stringfellow, E., Jatkar, A., Crowley, D., Bala Chandran, R., "*Spatial Distributions of Hydration Cycling in Salt Hydrates using Neutron Imaging.*"

5.1 Introduction

By chemically absorbing (hydration) and releasing (dehydration) water vapor stored in air salt hydrates can store thermal loads at high energy densities with low material costs [66, 69, 156, 67]. While promising, salt hydrates slowly degrade with repeated hydration cycles, which has been observed at both the material and reactor scale [83, 168]. Particles may swell and agglomerate during hydration forming a solid layer blocking water diffusion pathways during hydration and subsequent dehydration [99, 79, 100]. *Operando* techniques have been deployed to further understand of how salt hydration occurs focused on understanding spatio-temporal profiles of reactors [102, 91, 103, 104]. Nuclear magnetic resonance (NMR), after calibration, allows quantitative measurement of water concentrations during hydration, but is limited to 1D scans with a reported 3-5 mm spatial and 30 minute temporal resolution [102, 91]. Magnetic resonance imaging (MRI) offers improved metrics with quantitative 2D scans with a reported up to 2 mm and 2 minute resolution (not simultaneously) [103]. Infrared thermal imaging (IR) can track the 2D thermal signatures of reactors producing heat in real time [104]. Spatial and temporal resolutions depend on IR camera specifications and field of view, but sub second and under 200 μm resolutions are possible with high end thermal cameras (e.g. FLIR T650SC) [104]. However, since thermal IR imaging reports temperature it is limited by an inability to directly track changes in hydration state, which only allows tracking when significant temperature change occurs. Due to the coarse spatial resolutions ranging from 2 to 5 mm of the above non-IR methods, these techniques cannot

investigate salt hydrates on the material scale with typical particle sizes ranging from a few millimeters to microns. This prevents a deeper understanding of how salts fail suggesting a need for higher spatial resolution techniques.

Neutron imaging can quantitatively track hydration states with 2D spatial resolution on the order of 50 μm and up to 1 second temporal resolution (although 30 second is more typical) offering the best combined metrics of any of the prior techniques [106, 107, 192]. *Operando* neutron imaging has been used to image the thermochemical absorption and desorption of NH_3 for both a pure and composite $SrCl_2$ salt reactor [106, 107]. A recent paper used neutron imaging to illustrate dehydration pathways for a single K_2CO_3 salt hydrate crystal [192]. However, since only a single crystal was studied the effects of cycling in an ensemble of particles is not determined, and no evidence of real time tracking is provided, so further real-time investigation of multiple salt hydrate particles where agglomeration can occur is still needed.

The standard for material characterization is thermo-gravimetric analysis (TGA) where hydration rates are tracked by measuring mass changes in a pan filled with salt a few millimeters thick [79, 4]. Yet, even in this small scale some salts show evidence of a solid layer diffusion barrier forming during hydration, which preferentially absorbs water vapor slowing access to most of the salt [79]. Supportive matrix materials, such as vermiculite and SiO_2 shells, have been used to increase the stability and cyclability of salt hydrates [193, 82, 156]. These composites can increase structural stability and provide an interconnected porous network to improve water vapor transport and provide room for swelling to prevent diffusion barriers from forming [99, 193]. Unlocked by the one to two orders of magnitude improved spatial resolution of neutron imaging, we first perform *operando* TGA experiments comparing the hydration and dehydration cycling between the pure and composite (expanded vermiculite host) forms for representative salts. We image two promising salt hydrates based on their high energy densities and popularity in literature [90, 9, 171, 172]: $SrBr_2$ and K_2CO_3 although K_2CO_3 had minimal reaction, possibly due to a nucleation barrier preventing hydration [194]. We compare water uptake and release for chambers filled with two different heights of salt showing how diffusion times change with salt height arguing for the importance of reporting standards for interpreting TGA results. We provide direct evidence of how particle swelling can slow down water uptake for pure salt hydrates and how this can be significantly reduced with the use of composites. We discuss implications of this finding for reactor design.

We also validate neutron imaging for investigation at the reactor scale. At the reactor scale at slow enough flow rates, the salt hydrate absorbs all incoming water vapor into the reactor up until the salt's equilibrium vapor pressure [72]. This vapor mass transport

limited regime exhibits a trademark reaction front with constant outlet temperature that moves from inlet to outlet as salt is hydrated [72, 104, 195]. At higher flow rates, kinetic limitations dominate widening or eliminating this moving front, which results in relatively uniform hydration across the length of the bed, but at a slowly decreasing rate and outlet temperature [195, 91], which has implications for supplying target reactor power. To observe this flow regime transition and show how neutron imaging can be applied to reactor scale imaging, we conduct preliminary through flow reactor experiments at two different flow rates for the relatively stable $SrBr_2$ composite [96].

Overall, the purpose of this letter is to (1) establish a proof-of-concept platform for imaging salt hydrates with neutron imaging for both material and reactor characterization, (2) quantify the impact of particle swelling on water vapor diffusion for pure and composite salt hydrates on the TGA material characterization length scale, and (3) demonstrate how hydration profiles changes with flow rate across the mass transport to kinetic transition at the reactor-scale. This platform will enhance a deeper fundamental understanding of salt hydrate reactions.

5.2 Methods Overview

Neutron imaging was conducted at the Multimodal Advanced Radiography Station (MARS) CG-1D beamline at the High Flux Isotope Reactor (HFIR) at Oak Ridge National Laboratory. This study reports results from neutron imaging strontium bromide in both its pure and 50wt%-50wt% $SrBr_2$-vermiculite form. Pure and vermiculite composite potassium carbonate (K_2CO_3) were also tested using the same diffusion chamber methods below. However, the K_2CO_3 failed to react, except when the inlet humidity is set above its deliquescence point. Therefore, the K_2CO_3 setup is only shown in Fig. 5.1a to demonstrate the ability of the reactor to image 4 flow chambers at once, but is not discussed elsewhere. The experimental platform is shown in Fig. 5.1 to illustrate both the diffusion chambers and reactor setup as well as the flow and moisture controller used to generate both moist and dry air streams to cycle the salt hydrates. Corresponding images of the experimental setup at MARS are shown in Fig. C.1. Details of Experimental Methods and neutron imaging analysis are included in Appendix C.

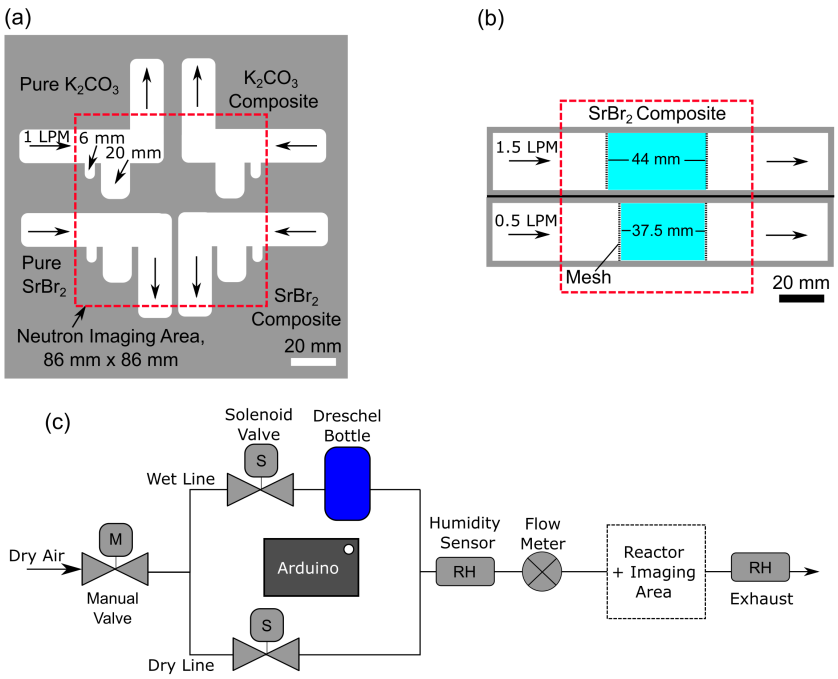


Figure 5.1: Neutron imaging setup for (a) diffusion chambers, (b) through flow reactors, and (c) simplified flow loop setup. Neutron imaging area is 86 x 86 mm represented by the dotted red box.

5.3 Results and Discussion

5.3.1 Operando diffusion chamber hydration

Fig. 5.2 shows the diffusion front advancements during the first hydration step (ORNL/SI-Mov1 for movie of process). For the pure $SrBr_2$ (Fig. 5.2a-d), the salt is initially dehydrated although a few individual particles appear hydrated. As time progresses, the pure salt hydrates sharply from the top down rather than uniformly offering validation to a diffusion front hydration mechanism. After 12 hours, the smaller TGA chamber is fully hydrated, but the large chamber is still only partially hydrated ($\sim$ 25%) at the end of the hydration step at 19.2 hours. Measuring the increase in salt hydrate area in the hydrated salt between the initial and final frames of hydration (Figs. 5.2a and d) reveals the pure $SrBr_2$ swells roughly 55% during hydration. This degree of swelling likely slows down or prevents inter-particle diffusion forcing water vapor to diffuse through the solid hydrated layer reducing hydration rates. In contrast, the composite $SrBr_2$ only swells about 12% (Figs. 5.2e and h) suggesting that the internal porosity of the porous host can handle water uptake with reduced blocking of inter-particle diffusion pathways [100, 79]. This is evidenced by the much quicker diffusion rates of the composite. The smaller TGA chamber is fully hydrated before 6 hours and the

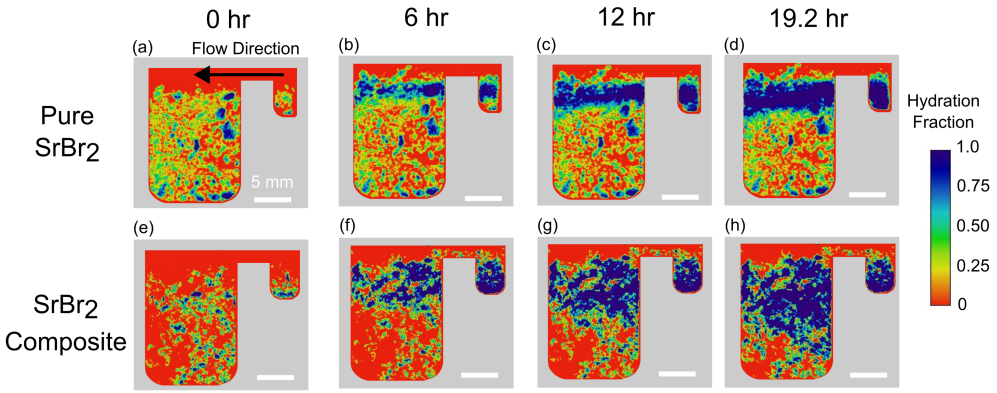


Figure 5.2: Normalized hydration profiles for both pure (a-d) and composite (e-h) $SrBr_2$ diffusion chambers at different time stamps. Scale bars are 5 mm.

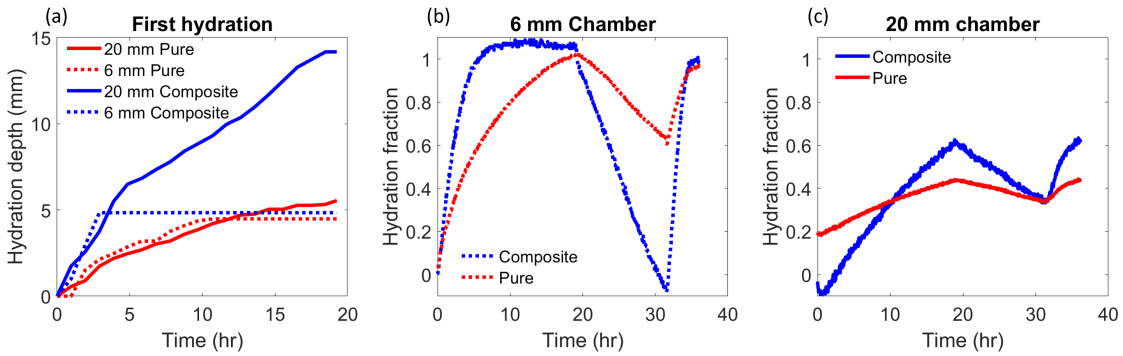


Figure 5.3: (a) Comparison of hydration depth versus time for pure versus composite $SrBr_2$ during first hydration and tracking of cycling on hydration fraction for (b) 6 mm and (c) 20 mm deep chambers.

larger chamber is largely hydrated ($\sim$ 75%) at the end of hydration. Compared to the pure salt, the composite also has a less sharp diffusion front with the right half (first to hydrate) of the large chamber appearing to hydrate faster than the left half (Fig. 5.2h) suggesting a slight impact of a hydration gradient with air flow across the chambers.

When the hydration depth (adjusted from initial top of each salt in its dehydrated state) for the first hydration is compared across the 4 chambers (Fig. 5.3a), the hydration rates change with time. Both the small and large chambers for each salt type (pure vs composite) follow the same initial hydration rates. The smaller TGA chamber composite $SrBr_2$ reaches it maximum hydration depth in 2 hours, which is 5 times faster than the pure salt. While the larger composite chamber has a slight decrease in slope after 4 hours, its hydration rate beyond this point is relatively linear and is more than twice as high as the pure salt in the same time frame. For the large pure $SrBr_2$ chamber, the hydration profile continues to

slow down with time. This coupled with Fig. 5.2a-d provides evidence of an intra-particle diffusion barrier forming that forces water vapor to diffuse through salt particles rather than through the kinetically faster porous network between particles, which has been previously suggested but not observed [79]. This showcases the power of the enhanced spatial resolution of neutron imaging to investigate fundamental mechanisms of salt hydration.

When the smaller 6 mm deep chambers are compared to the larger 20 mm, both the pure and composite 20 mm chambers never reach full hydration even though the same salts are tested as for the smaller chambers (Fig. 5.3c). This has important implications for measuring salt hydrate kinetics. Since the larger chamber has to hydrate a deeper distance its apparent material kinetics, as measured by fraction of salt hydrated, are slower. This calls for the need to report chamber/pan depths for material scale characterization as this study shows the total reaction time is heavily dependent on the depth/thickness of salt hydrate used.

When comparing diffusion depths across hydration cycles, the TGA smaller chamber $SrBr_2$ composite reaches 95% hydration in 4.8 hours for the first cycle (Fig. 5.3b). Then, following dehydration, the second hydration only takes 2.9 hours indicating improved hydration with cycling rather than degradation. While the pure the $SrBr_2$ TGA chamber only dehydrates to 60% hydration fraction, its second hydration time from 60% to 95% hydration is also a much quicker 3.3 hours compared to the 8.9 hours from the first hydration. Previous studies have suggested pure salts hydrate faster after a few cycles as cracks form that increase exposed surface area and shorten intra-particle water vapor diffusion pathways although finer resolution imaging, such as X-ray radiography with 1-2 μm resolution, is needed to confirm this [100].

5.3.2 In Situ Through Flow Reactor

For the reactor experiments, when tracking the hydration fraction progression of the slower flow rate, 0.5 LPM case (Fig. 5.4e-h), initial hydration occurs near the inlet (Fig. 5.4f) and progresses towards the outlet (Figs. 5.4g,h). (See ORNL/SI-Mov2 for movie). This progression of a moving hydration front with time is the trade-mark of operating in the vapor mass transport regime although the slight increases in hydration levels near the outlet with time suggests kinetic contributions are also at play (Fig. C.4c,d) [72, 195, 91]. When the flow rate is tripled to 1.5 LPM (Fig. 5.4a-d), a different hydration fraction profile is formed with the most obvious being the faster rate of hydration reaching full completion by the 5 hours image (Fig. 5.4c). The hydration fraction spatial profiles are also more uniform suggesting operation deeper into the kinetics limited regime [195, 91]. To probe these differences further, Fig. C.2a compares bed average hydration fractions and instantaneous measured reaction

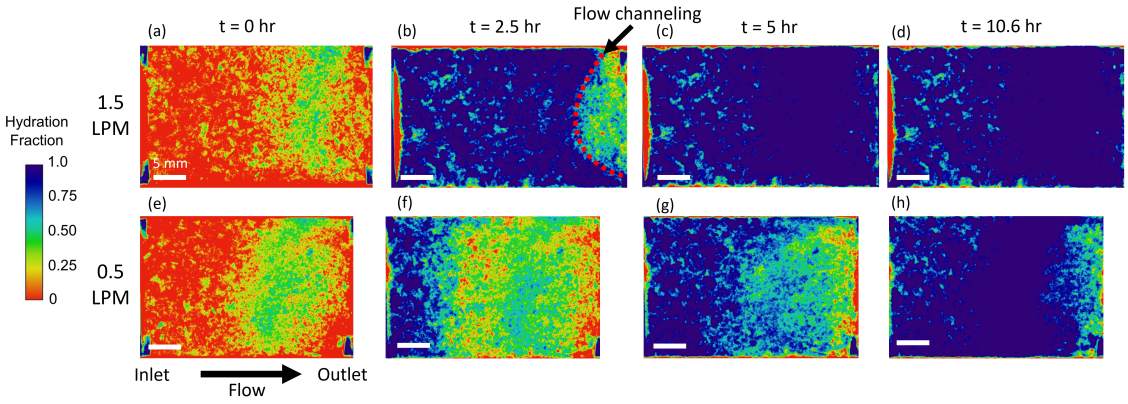


Figure 5.4: Normalized hydration profiles for flow rates of 1.5 LPM (a-d) and 0.5 LPM (e-h) for $SrBr_2$ through flow reactors at different time stamps. Scale bars are 5 mm.

rates for the two flow rates. Both reactors begin at an initial hydration fraction of about 15% and go above 100% (Fig. C.2a), which again is an artefact of the right half (closer to outlet) of the reactor likely still being partially hydrated/more densely packed than the left half which is used for calibration. Again, the 1.5 LPM reactor is shown to hydrate faster (Fig. C.2a), but when the reaction rate profiles are compared (Fig. C.2b), the 1.5 LPM case has a high initial peak that quickly drops off with time. In the kinetics limited regime, the reaction rate slows down as less salt is left to react [195]. In contrast, for the slower 0.5 LPM, while there still is a decline in reaction rate with time, this change is much more gradual. Operation solely in the mass transport limited regime results in a constant reaction rate profile with time, so the slow decline suggests the 0.5 LPM reactor is operating mainly in this regime although the gradual decline indicates some mixed kinetic contributions. This is further shown when comparing the outlet relative humidity versus time plots (Fig. C.3) where the initial outlet relative humidity is much lower than the inlet with the higher flow rate returning to the inlet humidity of 45% much quicker.

In addition, the reactor results reveal evidence of flow channeling (Fig. 5.4b), where the salt near the edges of the reactor hydrate faster than the center, which is thought to be due to a combination of differences in salt porosity and radial flow profiles at the edge [103]. Flow channeling has been observed for other thermochemical materials (zeolite cylindrical reactor), although this provides evidence flow channeling can occur for composite salt hydrates in a square tube [103]. While the reactor results are proof-of-concept in nature, the benefit of the improved spatial resolution of neutron imaging allows hydration dynamics at inlets and edges of different reactor designs, such as effectiveness of a mass diffuser in evenly hydrating the salt [83], can be investigated in meaningful length scales.

5.4 Conclusions

Overall, the purpose of this letter is to validate *operando* neutron imaging as a platform to probe the fundamental mechanisms of salt hydrate hydration and dehydration with much improved spatial resolution (42 μm) compared to prior techniques. On the smaller materials characterization scale, we show direct evidence of the formation of a diffusion front forming within the first few millimeters of material that appears to slow the hydration of pure $SrBr_2$ dictated by particles swelling by 55% during hydration. In contrast, the $SrBr_2$ composite has a much more modest 12% swelling with the porous support network believed to allow for continued inter-particle diffusion during hydration. Diffusion chamber height is found to strongly dictate the apparent reaction rate, so standards for reporting thermo-gravimetric analysis pan height are called for. Preliminary through flow reactor experiments of the $SrBr_2$ composite show direct evidence of the transition from a moving wave front from mass transport effects to a more uniform hydration profile with increasing flow rate in the kinetics limited regime. This work showcases the power of improved spatial resolution *operando* techniques to help improve salt hydrates for thermochemical energy storage.

CHAPTER 6

Conclusion

This dissertation has two main research thrusts. The first was the development of additively manufactured oxide particle strength reinforced alloys. A phase-field study was developed to understand the impact of nucleation on microstructure evolution, and synchrotron *in-situ* imaging was conducted to investigate melt pool processability of a commercially produced (Kanthal APM and Kanthal A1) reinforced versus un-reinforced alloy. The second thrust aimed at developing salt hydrate thermochemical reactors for high power density applications. The Ragone framework was extended to this system to understand tradeoffs in power and accessible energy. Modeling and experimental results reveal the transition between mass transfer and kinetics limited regimes. Neutron imaging was conducted to understand the fundamental hydration and degradation mechanisms of pure versus composite salt hydrates. This provides a new platform for salt hydrate *operando* studies. Combined this thesis helps advance the state of the art for the next generation of materials to enable more efficient power plants and thermal energy storage for a greener future.

6.1 Thesis Summary

6.1.1 Microstructure of Nanoparticle-Reinforced Metal Alloys

Due to the large thermal gradients and cooling rates involved, most techniques and studies can only observe microstructures after solidification. The 2D phase-field simulations of Chapter 2 allow the role of nanoparticles serving as heterogeneous nucleation and grain boundary pinning sites to be directly investigated throughout solidification. Compared to the classic analytical Smith-Zener relationship for grain size prediction, which is based on the geometric chance a randomly placed nanoparticle will lay on a grain boundary ignoring any effects of how the alloy solidifies [42], this study develops a modified Smith-Zener equation that explicitly incorporates nucleation rate and grain boundary pinning during solidification. Across the 7 orders of magnitude of nucleation rate/site (J^*) densities considered

($1.95\times10^6 - 1.95\times10^{12}$ nuclei/m^2), grain size (d_z) decreases between 3-5 times depending on area fraction with a dependence $d_z \sim 1/J^{*0.15}$. Smith-Zener predictions also show grain size is inversely proportional to nanoparticle concentration (quantified by area fraction), Φ_{np}, by $d_z \sim 1/\Phi_{np}^{0.25}$ for the random distribution and by $d_z \sim 1/\Phi_{np}^{0.33}$ for the clustered distribution showing a diminishing return on grain size reduction at higher area fractions. At low area fractions, $\sim$ 0.01, clustered distributions have 15-45% larger grain size than the random distribution. Grain size is shown to be directly predicted by the fraction of nanoparticles on grain boundary triple points (in 2D) with grain size plateauing when pinning fraction plateaus.

In Chapter 3, synchrotron imaging is used to understand how the processability changes between two commercially produced FeCrAl alloys, Kanthal A1 with no oxide particles and Kanthal APM with oxide particles, for laser based additive manufacturing. By comparing melt pool maps, the transition between lack-of-fusion to keyholing regimes were identified with an optimal starting condition for the setup for both alloys of 300 W and 800 mm/s. With no significant melt pool differences between the two alloys, this suggests particle free melt pool processing maps can be used as a starting point for particle reinforced alloys when at low enough particle concentrations, which are still significant enough to improve creep and corrosion properties [29, 30]. Decent agreement between the Rosenthal processability model and experiment was observed at lower laser power and higher laser speeds suggesting potential extension for similar FeCrAl compositions.

6.1.2 Integrated Heat and Mass Transfer for Thermochemical Energy Storage

In Chapter 4, a combined multiphysics model and experimental study of through flow salt hydrate reactors was conducted using pure K_2CO_3 and composite $SrBr_2$ as representative salts. Effective hydration kinetics are compared across the material and reactor scale adding to the limited knowledge of length scaling effects for salt hydrates. The Ragone framework, which has been extensively applied for characterizing the performance of electrochemical and more recently for thermal energy storage systems, is extended in this work to salt hydrate thermochemical reactors. This allows tradeoffs between power and accessible energy for different reactor designs and materials to be more easily compared. The parametric simulations suggest that as discharge times decrease to that of interest for daily load shifting (4-10 hours) the reactors transition from the mass transport to the kinetics limited regime. When the Damkohler number, which is the ratio of characteristic reaction rate to transport rate, is above 2 the reactor is dominated by mass transport limitations and when it is below

0.5 kinetic limitations dominate. When the Damkohler number is between 2 and 0.5 limitations arise due to both transport and kinetics. The Damkohler number can be analytically calculated based on salt properties and kinetics and reactor design to both predict power output and help to easily identify strategies to improve discharge rates. Effective strategies to improve power output are to increase air inlet velocity, decrease reactor length, and/or increase inlet relative humidity with reduced effects when operating deep in the kinetics limited regime. The experimental results suggest that reactor scale effective kinetics were roughly an order of magnitude slower than material scale kinetics likely due to changes in local salt temperature and morphology between the scales. The Ragone plots from this study suggest that the high power demands of daily cycling can be met when reactors operate close to their material scale kinetic limit although reactor scale kinetics discharge too slowly. Pumping power requirements and energy required to humidify the air to drive the reaction can significantly reduce or even cause a negative net power output. For the highest flow rate tested of 6 LPM the $SrBr_2$ composite reactor reached 164 Wh/kg of energy capacity, which is more than 90% of the theoretical energy capacity. A peak power of 11 W/kg was reached which slowly declined to time averaged 9 W/kg by the end. With this 20 hour discharge only a quarter of energy capacity can be reached in order to meet the 4 hour Department of Energy load shifting target [85], suggesting further optimization of reactor scale and temperature dependent salt hydrate kinetics is needed.

Chapter 5 shows neutron imaging experiments at Oak Ridge National Laboratory of both pure and composite $SrBr_2$ hydration on the material scale and the composite on the reactor scale. The study served as a proof-of-concept for neutron imaging as a platform to understand the fundamentals of salt hydrate degradation. Compared to previous techniques, such as nuclear magnetic resonance, magnetic resonance imaging, or thermal infrared imaging, which have spatial resolutions on the order of millimeters, neutron imaging improves this to tens of microns, and with a temporal resolution of 35 seconds. On the material scale, pure $SrBr_2$ neutron imaging reveals direct evidence of salt swelling and a diffusion barrier forming within a few millimeters of depth. The composite $SrBr_2$ remained stable with much reduced swelling (12% for the composite versus 55% for the pure salt) throughout a hydration and dehydration cycle. This is likely due to the porous support structure of the vermiculite matrix. With previous *operando* techniques, this entire diffusion front and swelling may not even be a single pixel, showcasing the resolution of neutron imaging. The preliminary $SrBr_2$ composite through flow experiments allowed tracking of spatio-temporal maps of hydration states showing direct evidence of the transition from mass transport (steady power output) effects to deeper into the kinetics limited (variable power output) regime detailed in Chapter 4. Flow channeling, where the salt hydrates faster along the reactor walls than in the center,

was also shown, providing a deeper understanding of fluid flow in reactors.

6.2 Thesis Impact and Contributions

Unique contributions from the nanocomposite studies include a phase-field simulation informed modified Smith-Zener equation that explicitly accounts for the impact of nucleation rate on solidified grain size. This coupled with the calculated dependence of grain size with pinning fraction show that nanoparticles should be selected for the ability to both effectively induce nucleation and pin grain boundaries to obtain the grain size reduction and related nanocomposite strength benefit. The phase-field model is also open source [109], which can be used as a tool for other modellers. For the *in-situ* synchrotron imaging experiments processing maps for two of the most popular corrosion resistant FeCrAl alloys, particle-free Kanthal A1 and reinforced Kanthal APM, were generated for the first time. These maps will help provide a starting point for future additive manufacturing efforts for these two alloys.

For the salt hydrate investigations, unique contributions include the establishment of the Ragone framework for salt hydrate thermochemical reactors. While the Ragone framework has been applied to the phase change community [5], bringing this framework to the salt hydrate community for the first time will help researchers understand tradeoffs in energy and power to more easily assess reactors for different end applications, such as peak thermal load shifting. Also, this framework will enable easier comparison between different reactor designs and operating conditions as well as for salt hydrate materials throughout the entire discharge process. The modified packed bed flow Damkohler number can determine when operation occurs in the mass transport versus kinetics limited regimes and predict specific power output. This will allow researchers to a priori predict how changes in reactor design/operation may or may not impact power output before conducting additional experiments. The experimental study provides valuable comparison between material to reactor performance, which is rarely reported, revealing a decrease in effective kinetics as the length scale increases. This suggests researchers need to account for temperature and morphological changes across length scales when predicting hydration rates. The *operando* neutron imaging study of the salt hydrates served as a proof-of-concept for a new imaging platform to study the fundamentals of salt hydration and degradation on both the material and reactor scale. Spatial resolution improvements by up to a factor of 100 has been achieved compared to previous *operando* techniques, which allows direct observation of phenomena previously inaccessible, with the study's observation of a water diffusion barrier forming for a pure salt hydrate an example. The 86 mm x 86 mm field of view also allows for 2D spatio-temporal maps of reactors to be imaged revealing dynamics of fluid flow and hydration, such

as flow channeling. The neutron imaging platform can be used to investigate many different thermochemical materials that involve uptake/release of water, hydrogen, ammonia, or broadly any compound with H-atoms; different form factors of reactors (flow over and flow through packed beds were tested in our work) can be tested and can be extended to probe temperature-dependent charging and discharging behavior.

6.3 Limitations and Future Work

6.3.1 Microstructure of Nanoparticle-Reinforced Metal Alloys

Limitations of Chapter 2 are that it is 2D and simulated a simplified 5 μm x 5 μm subdomain representing selective laser melting process. While a few preliminary 3D simulations (2.5 μm x 2.5 μm x 0.3125 μm subdomain) were conducted, revealing a transition from particles pinning at grain boundary triple points in 2D to just at grain boundaries in 3D, further and larger domain investigation is still needed. With typical melt pools on the order of 100 μm deep with an even larger heat affected zone, the smaller subdomains cannot simulate effects, such as dynamic clustering and molten metal flow, that emerge over these larger length scales. Ignoring the more complicated temperature gradients due to multi-layer laser scans, dynamic clustering of particles during solidification, and the lack of multiple laser scans in a more realistic system would likely have a significant impact on the resulting solidified grain size.

With the importance of nucleation rate and particle distribution established from the existing phase-field paper (Chapter 2), a more advanced model could be implemented to capture the effects of a more realistic simulation of a selective laser melting process with a larger simulation domain that incorporates dynamic clustering, heat transfer, and molten metal flow. By incorporating the competing effects of Marangoni convection and van der Waals forces, the range of laser powers and speeds that will result in uniform distribution of nanoparticles can be identified. The updated domain would likely need to be a few hundred micron sided cube to incorporate full melt pool effects although resolving $\sim$ 50 nanometer particles may be computationally prohibitive. Since phase-field order parameters within the bulk of the grain are constant, an adaptive mesh could be used with coarse resolution in the bulk and finer resolution around grain boundaries and nanoparticles. Additionally, to further reduce computational times of the 3D study, either a smaller parametric phase-field study could be conducted or a less computationally intensive technique such as cellular automata could be used although proper rules need to be implemented to correctly account for pinning dynamics [46].

Limitations of Chapter 3 are that only the processability of single track laser scans were conducted. Additive manufacturing builds up parts layer by layer, so any multi-layer effects are ignored. No material properties, such as creep or strength, were tested, so the true impact of the reinforcing particles cannot be verified. Also, only low concentration ($\sim$ 0.1 wt%) of particles were tested, so the impact of higher concentrations on melt pools is not investigated.

While the synchrotron processing maps for the Kanthal alloys of Chapter 3 provide a good starting point for further selective laser melting optimization, the mechanical and corrosion resistance improvement of additively manufactured reinforced Kanthal APM still needs to be established. Oxide particles are most effective in a uniform distribution, which allows for consistent nucleation leading to a homogeneous and more refined microstructure compared to a clustered distribution where nucleation sites are quickly covered [27]. Since a uniform distribution is not guaranteed after solidification, additively manufactured coupons under the optimal laser power and speed identified (300 W and 800 mm/s) should undergo corrosion and creep tests at target elevated temperatures. The two alloys can be compared to each other and to their commercially produced counterparts to determine if the oxide particles still improve alloy properties. While the nanoparticles have been shown to have a larger impact on melt pools as volume fraction increases [59], there remains a need to understand at what combined particle size and concentration changes in melt pool need to be accounted. Further synchrotron testing with a range of nanoparticle concentrations (e.g. 0.5-5 wt%) could be conducted.

6.3.2 Integrated Heat and Mass Transfer for Thermochemical Energy Storage

Beginning first with limitations of the model in Chapter 4, while the current salt hydrate multiphysics model was useful to establish transitions in operating regimes and power output, the model could be improved to incorporate additional effects. These include heat loss to the environment, observed flow channeling, and the ability to decouple hydration contributions between the salt hydrate and the reactive composite host. Since $SrBr_2$ composite kinetics and equilibrium vapor pressure were only fit at one temperature, temperature dependent/Arrhenius contributions were ignored for the model adding uncertainty. Also, the material kinetics were based on a flow over rather than a flow through reactor where differences in packing fraction, swelling, and local temperature could impact the measured kinetic constants. The model was also simplified and assumed a plug flow distribution and no heat loss. Results from Chapter 5 showed evidence of the edges of the reactor hydrating faster

than the center, which can result in inactive salt areas near the edges that can reduce overall output power [103]. The Damkohler number could also be improved by accounting for bed average effects rather than just inlet conditions to allow power predictions to be fully analytical based solely on salt properties and reactor design and operation rather than having to run initial simulations. This will help iterate reactor design more rapidly.

For the experimental reactor, limitations include that the significant heat losses measured for the reactors made it harder to isolate the impact of changes in flow rate on power output as both mass and heat transfer were changing. Additional reactor designs could also be tested. An example would be radial flow reactors where water vapor is introduced along the edges of the reactor rather than just at a single inlet, which can reduce parasitic pressure drops [191]. The measured material scale kinetics over-predicted the model best fit reactor scale kinetics; a differential element reactor (a few millimeters long to operate in the kinetics limited regime) could be filled with salt to test material kinetics at different length scales explicitly. A heated inlet and/or different packing fraction/morphology of salt hydrates could be varied to understand what impact these have on discharge times. These tests can compare how/if salt hydrate kinetics change from the traditional flow over material scale measurements to a flow through configuration more representative of reactor conditions, which may differ in exposed surface area and temperature.

Additional experiments could be conducted with the existing through flow reactor. These include operating at a higher flow rate to experimentally verify that the 6 LPM flow rate is already close to the fully kinetics limited discharge time for the $SrBr_2$ composite. A heated inlet setup ($T_{\text{inlet}} = 30 - 50$ °C) could be implemented with preliminary results showing this approach can dramatically reduce dehydration times from the current several days. The impact of a heated inlet with different inlet humidities can also be investigated with power outputs compared on a Ragone plot to experimentally determine how to achieve daily cycling. While $SrBr_2$ composite was used as a model salt the reactor can also be used to investigate other salts. For all additional tests, improved insulation should be used to reduce heat loss to eliminate this variable from analysis.

For high power applications, such as daily load shifting, operation into the kinetics regime where output power decreases with reaction extent is likely. This coupled with the fact that building heating demands change throughout the day, suggest dynamic control of the reactor with variable flow rates may be required. Power output can be estimated by $\dot{Q} = \dot{m}_{\text{air}} C_{\text{p,air}} (T_{\text{out}} - T_{\text{in}})$, so a proportional integral derivative (PID) controller could deployed to adjust air flow rate to maintain a constant temperature rise ($T_{\text{out}} - T_{\text{in}}$) or a constant output power ($\dot{Q}$) [187]. Increasing air flow rate has a diminishing impact on increasing instantaneous reactor power the further into the kinetics limited regime as well as at the end

of discharge, so the viability of this strategy should be investigated.

The parasitics of the pumping power and energy required to meet inlet relative humidity are shown to be significant in theory, but future work calls for both factors to be experimentally quantified when assessing the potential of a salt hydrate reactor. Since both parasitics depend on inlet velocity, an analysis of realistic air flow velocities for salt hydrate reactors integrated with heating, ventilation, and air conditioning (HVAC) systems are needed. A differential pressure transducer could be used to verify and quantify the pressure drop and corresponding additional pumping power required to run the experiment. Further work is needed to determine realistic moisture supply fractions during typical building heating for different climates, and the feasibility of a humidity recuperation system for an open system sourcing outside and recycled air. Humidification parasitics were shown to be reduced for salts (in the mass transport regime) with lower temperature dependent equilibrium water vapor pressure curves across the temperature range of interest since a higher fraction of moisture generated can be hydrated by the salt. Further investigation into different salts with these ideal working windows is warranted.

The results in Chapter 5 serve their purpose as a proof-of-concept to establish *operando* neutron imaging as a platform to image the cycling of salt hydrates on both the material and reactor scale with improved spatial resolution. However, limitations from this first proof-of-concept are listed below. Limitations include the lack of repeated cycles due to time constraints. For the diffusion chambers, while some cycling was conducted only the smaller $SrBr_2$ composite chamber had a full cycle plus a second hydration. The other chambers only had incomplete cycles with partial hydration fractions. Since salt degradation has been observed to occur over several full hydration/dehydration cycles this information is missing [100]. On the reactor scale, a major limitation is the reactors were not fully dehydrated at experiment start. This required several hours of valuable beamtime to be used to dehydrate the reactors for imaging. This also caused issues in trying to calibrate the hydration fraction measurements as the portions of the reactor measured below 0% hydration fraction and above 100% hydration fraction at different points in time. To maximize transmission the Al reactors were not insulated, so significant heat loss to the environment is expected, which impacts equilibrium vapor pressures and temperature dependent reaction kinetics.

Future work for the neutron imaging platform could involve imaging different salt hydrates or under different form factors, such as in compressed salt tablets. While results for pure and composite K_2CO_3 are not shown in this dissertation, calibration cell imaging for both salts suggest sufficient hydration/dehydration contrast to be imaged if the salts can be properly synthesized and conditioned for reliable cycling. Different reactor designs such as radial flow or a honeycomb geometry could also be be imaged to determine uniformity

of hydration [171]. Approaches to improve spatial resolution should also be pursued. X-ray based micro-computed tomography offers 1-2 μm resolution compared to 42 μm for neutron imaging. While X-rays may have reduced contrast between hydrated and dehydrated phases as compared to neutron imaging, this improved resolution can be used to probe salt cracks, which neutron imaging cannot resolve, and reveal composite morphologies in great detail, which can impact water vapor diffusion pathways and kinetics.

APPENDIX A

Appendix for Chapter 2: A Phase-Field Study on the Effects of Nucleation Rate and Nanoparticle Distributions on Solidification and Grain Growth

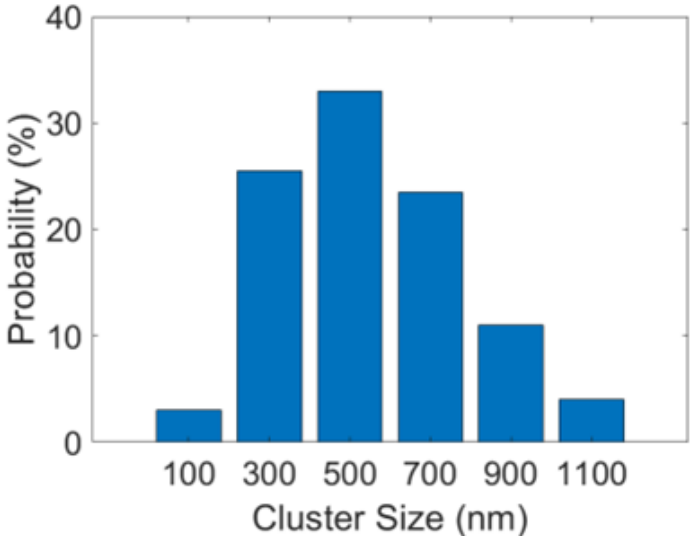


Figure A.1: Cluster size radius distributions used in generating clustered cases. Each cluster is made up of individual 25 nm radius particles. Data is from selective laser melting of nano-Tic reinforced Inconel 718 [6]

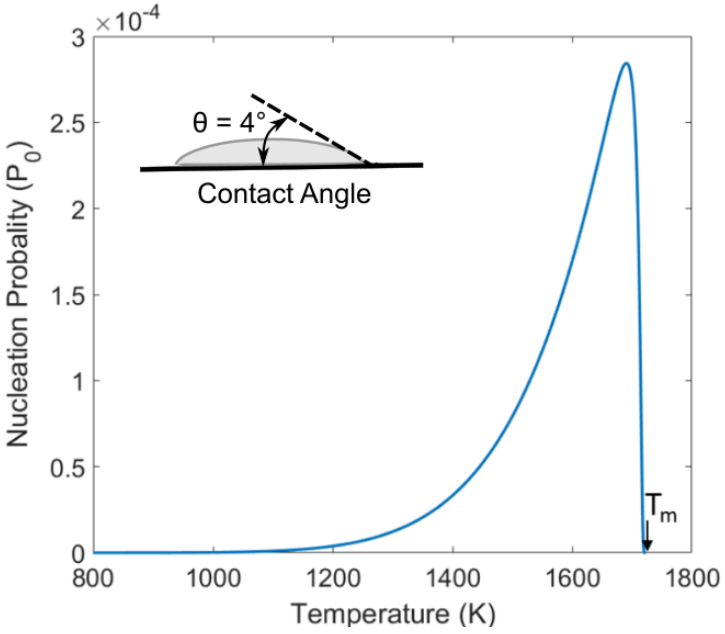


Figure A.2: Nucleation Probability, P_0, versus Temperature at N_0. T_m is the melting point of Stainless Steel 316L from M. Yang et. al. [7]. $N_0 = 1$ corresponds to 1.95×10^9 nuclei/m^2. Probability calculated for contact angle of $\theta = 4°C$.

Table A.1: Grain Size and Pinning Fraction results for 3D simulations of random and Φ_np = 0.01 with r_p = 25 nm in a 2.5 μm × 2.5 μm × 0.3125 μm thin film domain.

Simulation	Average Grain Size (μ m)	Pinning Fraction
5×10^{12} nuclei/m^3	0.705	0.22
5×10^{13} nuclei/m^3	0.543	0.37
5×10^{14} nuclei/m^3	0.340	0.41

A.1 Note 1: Explanation of PRISMS-PF Phase-field Grain Remapping

During the simulation if two grains of the same order parameter come close to touching, the remapping algorithm switches one of the order parameters to avoid artificial coalescence to maintain a realistic microstructure. With grain remapping two grains may collide and merge before they can be reassigned, so simulations are considered acceptable if less than 1% of grains artificially merged. The highest number of grains generated for a simulation is over 400, but $N = 16$ grain orientations is found sufficient to simulate realistic microstructures, which reduces computation time and memory use [196]. This is less than half the required orientations of other similar nanoparticle grain growth simulations [34, 197].

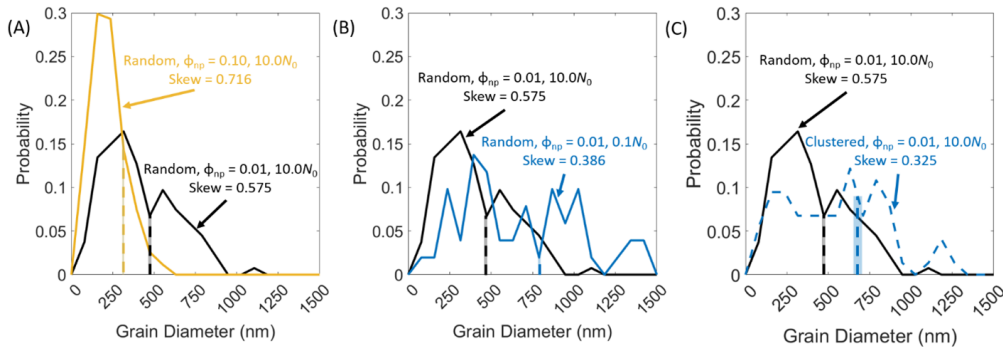


Figure A.3: Comparison of final grain size distribution to reference case of random with area fraction, $\Phi_{np} = 0.01$, and nucleation site density, $10N_0$. Impact of (a) area fraction: random, $\Phi_{np} = 0.10$ and $10N_0$, (b) nucleation rate: random, $\Phi_{np} = 0.01$ and $0.1N_0$, (c) clustering: clustered, $\Phi_{np} = 0.01$ and $10N_0$. Dotted vertical lines indicate the average grain size for each case with shaded regions indicating standard deviation. $N_0 = 1$ corresponds to 1.95×10^9 nuclei/m^2.

A.2 Note 2: Explanation of MATLAB Grain Analysis Program

For grain size analysis, a custom MATLAB grain image analysis tool is used to count the number of distinct grains, individual grain areas, and fraction of nanoparticles on grain boundaries. Since the locations of each nanoparticle are known, a rectangular subdomain, four times the individual particle radius, containing the nanoparticle is inspected. Since each grain at a grain boundary has a distinct color, the number of colors present in the image is checked. Filtering out the color of the nanoparticles, if additional two colors are present that indicates the presence of a grain boundary, and the particle counts towards the on grain boundary pinning fraction. Three additional colors indicate the particle is at a triple point of three grain boundaries. For the 3D simulations, grain size and pinning fractions were determined by averaging the results from 3 planes of the simulation. A plane from the top, middle, and bottom of the domain were analyzed. While choice of a screening subdomain can influence the exact pinning fraction and grain number count of the MATLAB program, select simulations were manually counted to help reduce error in the selection criteria.

A.3 Note 3: Grain Size Distribution

To further quantify the final microstructures, Fig. A.3 shows the impact of area fraction, nucleation site density, and clustering on grain size distributions. Skewness represents the

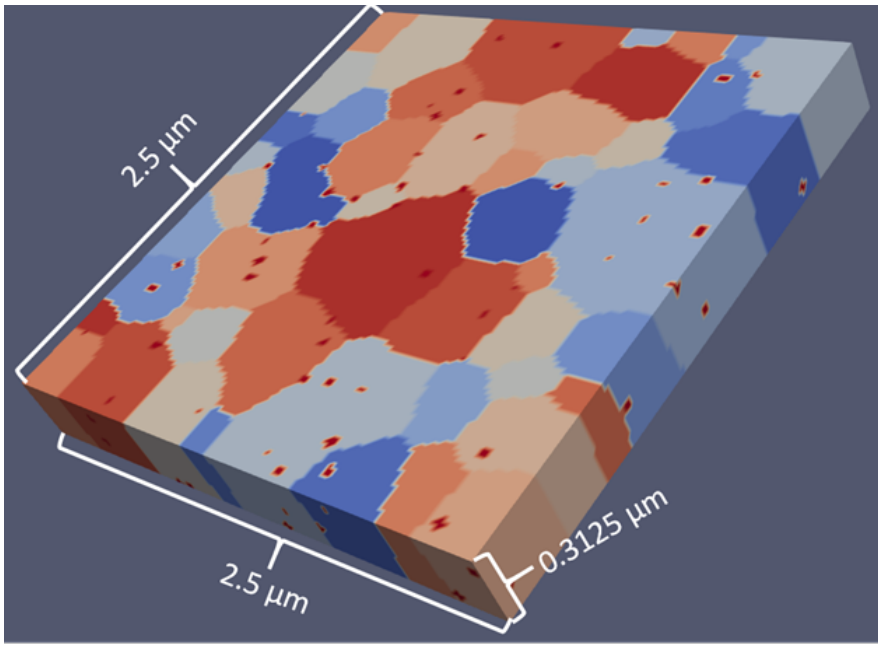


Figure A.4: Final Grain Microstructure of 3D Domain after 20,000 μs for random, Φ_{np} = 0.017 and a site density of 5×10^{14} nuclei/m^3.

extent of deviation from a normal distribution; therefore, a normal distribution will have a skewness of 0 [198]. For an ideal, homogenous microstructure, most grains will be close to the average size with a relatively larger fraction of grains smaller than the average to avoid a few larger grains from dominating the microstructure. This would result in a positively skewed distribution with skewness of 0.5–1.0 [46, 140]. A random distribution of nanoparticles with $\Phi_{np} = 0.01$ and $10N_0$ sites, with an average grain size of 487 nm, standard deviation of 11 nm and a skewness of 0.575, is selected as a reference case for Fig. A.3a–c. When the nucleation site density is held fixed ($10N_0$) and the area fraction increases to 0.1, the skewness increases to 0.716 and standard deviation decreases, indicating a higher fraction of grains are smaller than the average compared to reference case. When the area fraction is fixed ($\Phi_{np} = 0.01$) and the nucleation site density is decreased to $0.1N_0$ (Fig. A.3b), the distribution and standard deviation widen (skewness = 0.386) with a higher likelihood of having larger grains (> 1000 μm) than the reference case. This indicates the nucleation rate, controlled by site density, impacts grain distribution. When nucleation rate ($10N_0$) and area fraction (Φ_{np} =0.01) are fixed and the distribution type changes from random to clustered, the size distribution and standard deviation again widen with a skewness value of 0.325 (Fig. A.3c). As Fig. 2.3e shows, this wider grain size distribution is marked by small grains near concentrations of nanoparticle clusters and large grains far away from clusters. For all the cases shown in Fig. A.3, the largest grain size only approaches twice the average grain size.

While cutoffs can vary, abnormally large grains, which can induce detrimental mechanical properties, are typically at least 5–10x the average grain size [22, 110, 3, 2]. All simulations in our study are in the normal grain growth regime (even for $\Phi_{\mathrm{np}} = 0.01$, $10^{-3}N_0$), likely because of the assumption of perfect pinning by nanoparticles [140].

APPENDIX B

Appendix for Chapter 4: Modeling and Experimental Demonstrations Reveal Ragone Framework for Salt Hydrate Thermochemical Energy Storage

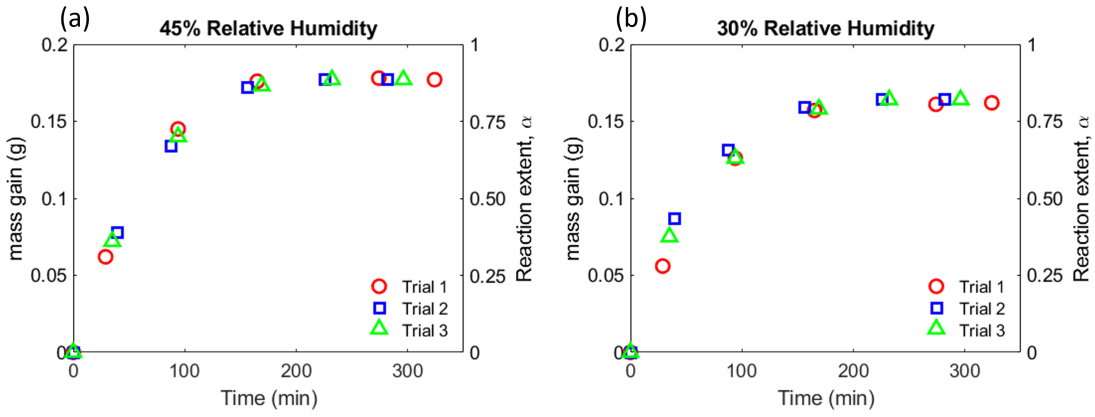


Figure B.1: Measured water uptake for $SrBr_2$ composite weigh boat material-scale experiments (1 g initial) at (a) 45% RH and (b) 30% RH.

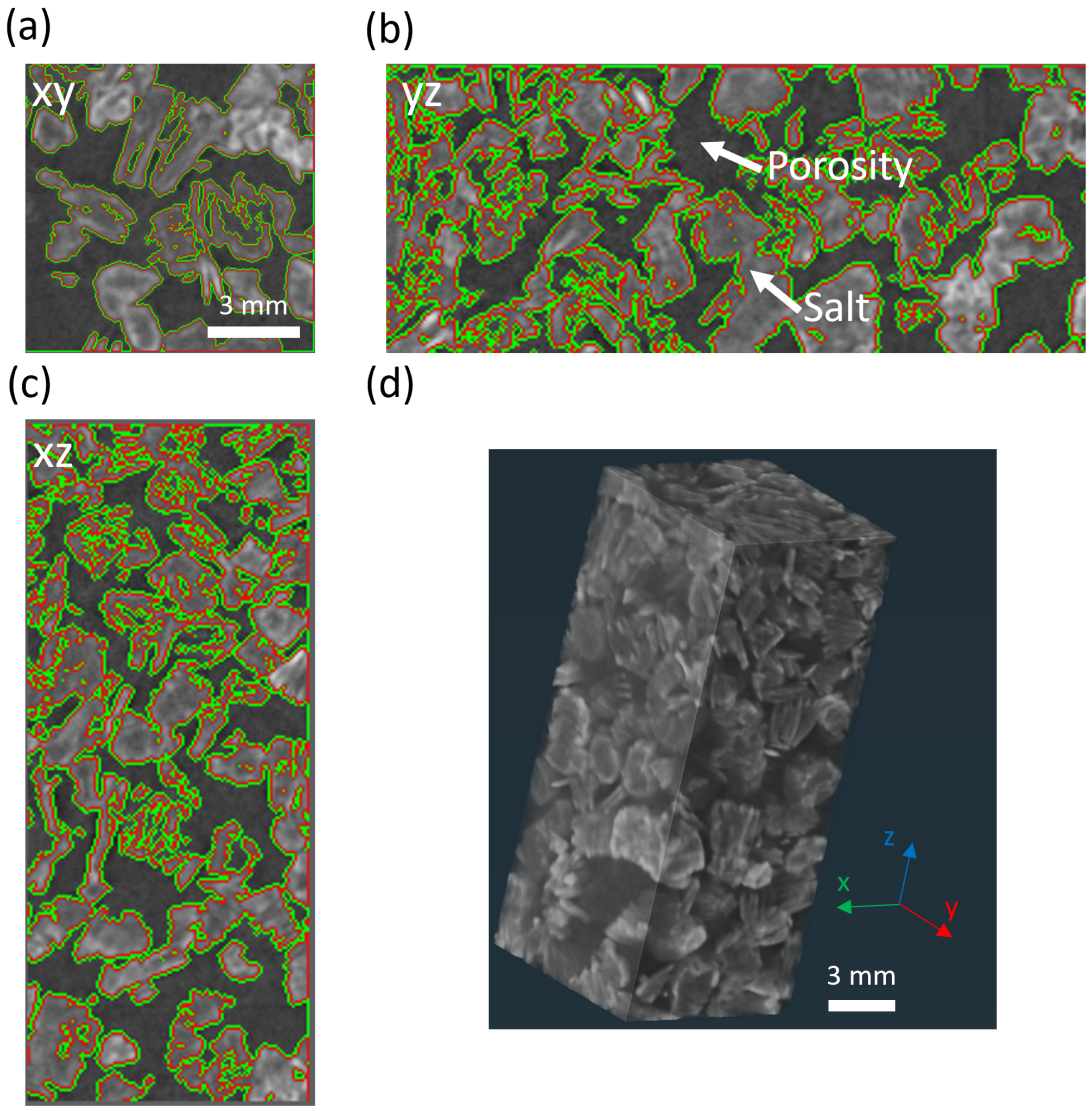


Figure B.2: Neutron computed tomography scans of dehydrated $SrBr_2$ composite. (a-c) 2D slices of scans. (d) 3D rendering.

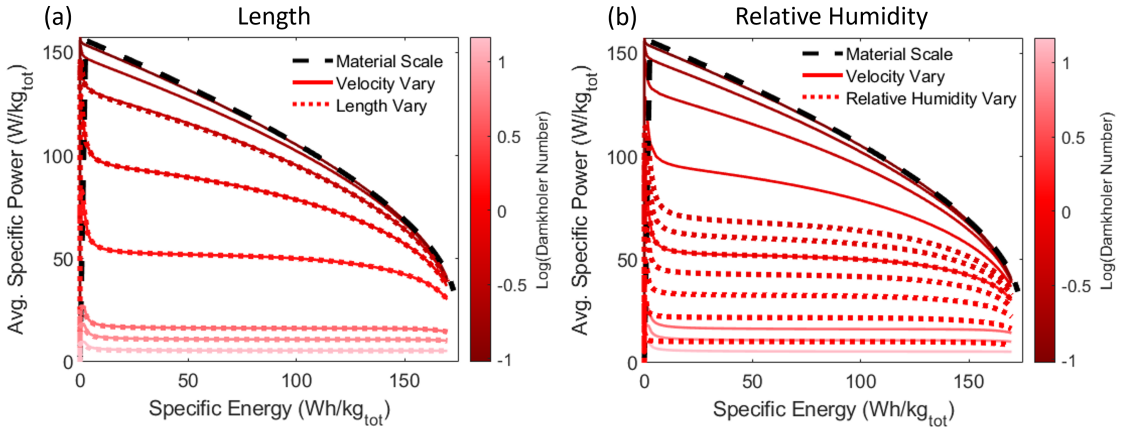


Figure B.3: Ragone plot with corresponding Da comparisons to Main Text $SrBr_2$ composite model variable velocity ($\vec{u}$) study. (a) variable reactor length, L = 1.2, 0.6, 0.4, 0.125, 0.0625, 0.03125 m, (b) variable inlet relative humidity, RH_{in} = 60%, 52.5%, 45%, 37.5%, 30%, 22.5%, 15%. Baseline values are $\varepsilon = 0.6$, $RH_{\text{in}} = 45\%$, $\vec{u} = 0.125$ m/s, L = 0.125 m, $T_{\text{in}} = 20$ °C, $K^* = 1.0$.

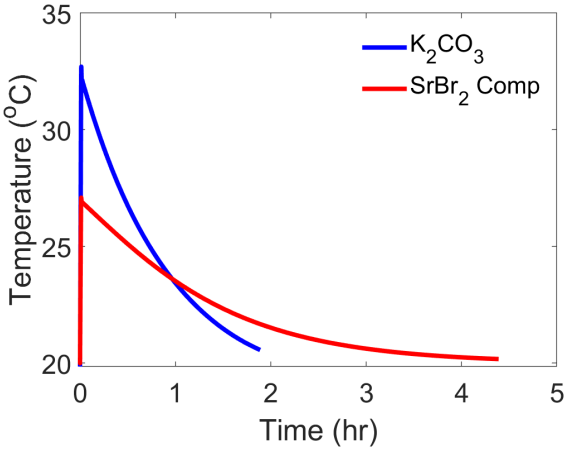


Figure B.4: Comparison of outlet temperature versus time for model results at equivalent Damkohler number ($Da = 0.38$) with $\vec{u} = 2$ m/s for K_2CO_3 and $\vec{u} = 0.5$ m/s for $SrBr_2$ composite. Cases are for $\varepsilon = 0.6$, 45% RH, $K^* = 1.0$, $L = 0.125$ m, $T_{\text{in}} = 20°C$, and $\Delta H_{\text{rx,SrBr2}} = 3.35$ MJ/kg$_{\text{H2O}}$.

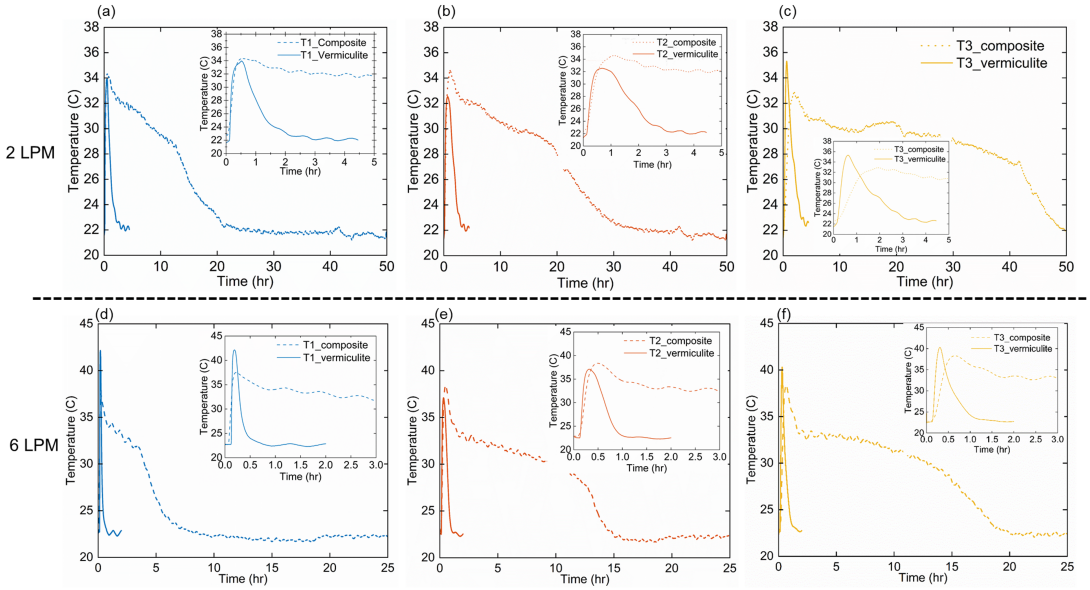


Figure B.5: $SrBr_2$ composite vs vermiculite experimental temperature profiles at 2, 4, and 6 LPM at different thermocouple probe locations.

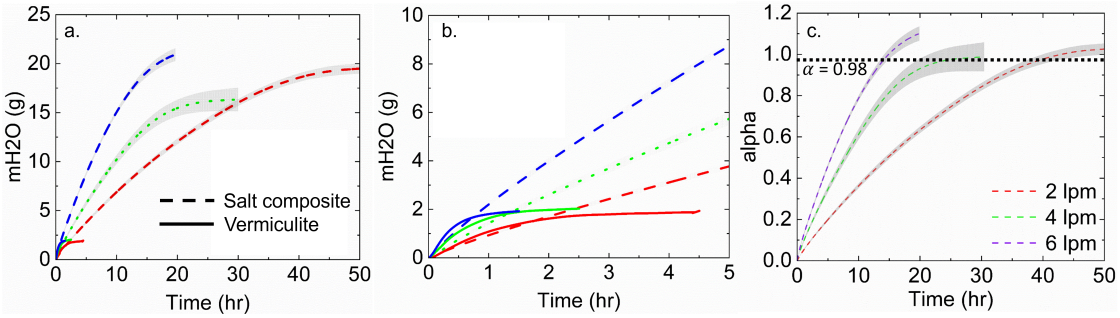


Figure B.6: Comparison of water uptake for $SrBr_2$ composite and vermiculite reactors. (a) water uptake at different flow rates, (b) zoomed in view of water uptake at different flow rates, (c) reaction extent with respect to time at 2, 4, and 6 LPM.

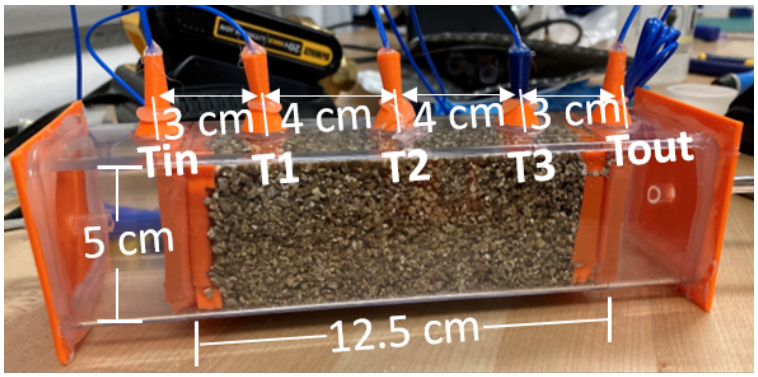


Figure B.7: $SrBr_2$ composite experimental reactor without insulation with locations of different thermocouple probes labeled.

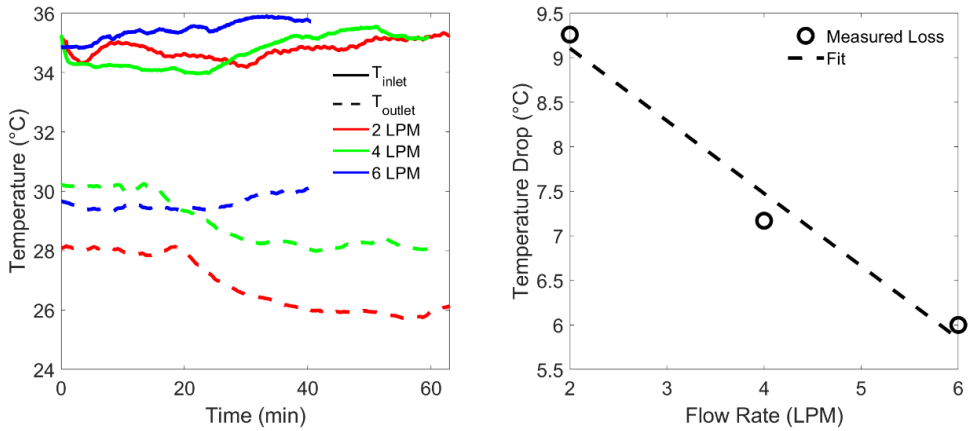


Figure B.8: Heated inlet test heat loss test of insulated dehydrated $SrBr_2$ composite reactor at flow rates of 2, 4, and 6 LPM. (a) inlet and outlet temperature, and (b) the calculated temperature drop from the 35°C inlet.

Table B.1: Dry air and water vapor properties used for both model and experimental reactor analysis [8, 9]

Dry air and water vapor	Air specific heat, $C_{\mathrm{p,f}}$	1007 J/(kgK)
	Air density, ρ_{f}	1.161 kg/m^3
	Air molar mass, M_{f}	0.029 kg/mol
	Water vapor molar mass, M_{f}	0.018 kg/mol
	Air viscosity, μ_{f}	1.846×10^{-5} kg/(ms)
	Air thermal conductivity, k_{f}	0.026 W/(mK)
	Air-vapor diffusivity, D_0	2.6×10^{-5} m^2/s
	Saturation water vapor mass loading fraction, ξ_{f}	0.015 $\mathrm{kg_{H2O}/kg_{air}}$

B.1 Model governing equations

Governing equations for the COMSOL model for water vapor and salt mass, momentum, and energy conservation and species transport are standard for salt hydrate reactors in a porous media, and are largely taken from [90] unless specified otherwise. Other aspects of modeling, such as reaction kinetics and Ragone plot calculations, are in the main text. Relevant salt and air properties are listed in Table 4.1 and Table B.1.

B.1.1 Mass conservation

Fluid: In the fluid phase, mass conservation is given by

$$\varepsilon\rho_{\mathrm{f}}\frac{\partial\xi_{\mathrm{v}}}{\partial t} + \rho_{\mathrm{f}}(\vec{u}\cdot\nabla)\xi_{\mathrm{v}} = \dot{r}^{'''} \tag{B.1}$$

where $\dot{r}^{'''}$ is a volumetric sink term for the water vapor due to hydration reactions for the salt.

B.1.2 Momentum conservation

Over the range of flow rates modeled in this study, the particle-scale Reynolds Number, Re_{p} ($Re_{\mathrm{p}} = \frac{\rho_{\mathrm{f}}\vec{u}d_{\mathrm{p}}}{\mu_{\mathrm{f}}}$ [181]), varies from 0.4-63. Therefore, while the fluid flow is laminar, considering inertial drag in addition to viscous drag is important, so we apply Darcy's Law with Forchheimer's term modification (Eq. B.2).

$$\nabla p = -\frac{\mu_{\mathrm{f}}}{\kappa}\vec{u} - \frac{c_{\mathrm{F}}}{\sqrt{\kappa}}\rho_{\mathrm{f}}|\vec{u}|\ \vec{u} \tag{B.2}$$

where $\vec{u}$ is the Darcy or the superficial velocity of air, κ is the bed permeability, and ∇p is the pressure gradient in the bed. We assume permeability is given by the Kozeny-Carman equation (Eq. B.3).

$$\kappa = \frac{d_{\mathrm{p}}^2 \varepsilon^2}{180(1-\varepsilon)^2} \tag{B.3}$$

The drag coefficient, C_{f}, is given by Eq. B.4 [199]

$$C_{\mathrm{f}} = 0.55\left(1 - 5.5\frac{d_{\mathrm{p}}}{D_{\mathrm{e}}}\right) \tag{B.4}$$

and D_{e}, the equivalent diameter of the bed, is given by Eq. B.5

$$D_{\mathrm{e}} = \frac{2wh}{w+h} \tag{B.5}$$

where h is the bed height and w is the bed width.

B.1.2.1 Energy conservation

At the temperature range studied ($20 - 40°\mathrm{C}$), thermal radiation is negligible [200]. Due to the small particle size and scaling analysis (Section B.2), we assume local thermal equilibrium between the solid and gas phase ($T_{\mathrm{s}} = T_{\mathrm{f}} = T$) [200]. The heat equation (Eq. B.6) is thus given by

$$(\rho C)_{\mathrm{eff}}\frac{\partial T}{\partial t} + (\rho C)_{\mathrm{f}}(\vec{u}\cdot\nabla)T = k_{\mathrm{eff}}\nabla^2 T + q_{\mathrm{s}}^{'''} \tag{B.6}$$

where $q_{\mathrm{s}}^{'''}$ is the volumetric heat generation term. The volume average heat capacity $(\rho C)_{\mathrm{eff}}$ is is given by Eq. B.7

$$(\rho C)_{\mathrm{eff}} = (1-\varepsilon)(\rho C)_{\mathrm{s}} + \varepsilon(\rho C)_{\mathrm{f}} \tag{B.7}$$

Similarly, the effective thermal conductivity, k_{eff} is given by Eq. B.8

$$(k)_{\mathrm{eff}} = (1-\varepsilon)k_{\mathrm{s}} + (\varepsilon)k_{\mathrm{f}}. \tag{B.8}$$

B.1.2.2 Species transport

The species conservation equation tracks changes in the mole fraction of water vapor in the mixture of dry air and water vapor present in the fluid phase and is given by Eq. B.9

$$\frac{\partial(c\varepsilon)}{\partial t} - \nabla\cdot(D_{\mathrm{eff}}\nabla c) + \nabla\cdot(\vec{u}c) = \frac{\dot{r}^{'''}}{M_{\mathrm{v}}} \tag{B.9}$$

where c is the concentration of water vapor in the air in mol/m^3. D_{eff} is the effective diffusivity of water vapor in porous medium (Eq. B.10)

$$D_{\text{eff}} = \frac{\varepsilon}{\tau} D_0 \tag{B.10}$$

where D_0 is standard air diffusivity at 20°C. Since the pore network is well connected, the tortuosity, τ, is approximated using the Millington and Quirk Model [201] (Eq. B.11)

$$\tau = \varepsilon^{-1/3}. \tag{B.11}$$

B.2 Local thermal equilibrium assumption validation

To validate our assumption of local thermal equilibrium we calculated the expected temperature difference ΔT between the solid (T_{s}) and fluid phase (T_{s}) assuming local thermal non-equilibrium. Our results show that $\Delta T \ll 1$ K, even for the most extreme case modeled, which is the $\vec{u} = 2$ m/s case. We use the model ($d_{\text{p}} = 500$ μm) and property values of Fig. 4.3 and Table 4.1 for K_2CO_3 since we expect a higher ΔT than for the $SrBr_2$ composite since K_2CO_3 has a much higher density. In the solid phase the non-equilibrium heat equation becomes Eq. B.12 and is adapted form Nield and Bejan [202].

$$(1-\varepsilon)(\rho C)_{\text{s}} \frac{\partial T_{\text{s}}}{\partial t} + \nabla \cdot q_{\text{s}} = q_{\text{sf}}(T_{\text{f}} - T_{\text{s}}) + q_{\text{s}}^{'''} \tag{B.12}$$

Re-arranging to solve for ΔT becomes Eq. B.13

$$T_{\text{f}} - T_{\text{s}} = \Delta T = ((1-\varepsilon)(\rho C)_{\text{s}} \frac{\partial T_{\text{s}}}{\partial t} + \nabla \cdot q_{\text{s}} - q_{\text{s}}^{'''})/q_{\text{sf}} \tag{B.13}$$

where $\frac{\partial T_{\text{s}}}{\partial t}$ is the temperature rise partial derivative. We take $\frac{\partial T_{\text{s}}}{\partial t} = (40\ ^\circ\text{C} - 20\ ^\circ\text{C})/(5 \times 60\ \text{s}) = 0.067^\circ$C/s based on typical outlet bed temperature rise times. 40°C represents the maximum temperature observed in the model although for $\vec{u} = 2$ m/s this is an exaggeration, which will overestimate ΔT. q_{s} is the solid conductive heat flux and is given by Eq. B.14.

$$q_{\text{s}} = (1-\varepsilon) k_{\text{s}} \nabla T_{\text{s}} \tag{B.14}$$

q_{sf} is the interstitial convective heat transfer coefficient between the solid and fluid phases given by Eq. B.15.

$$q_{\text{sf}} = a_{\text{sf}} h_{\text{sf}} \tag{B.15}$$

a_{sf} is the specific surface area given by Eq. B.16.

$$a_{\mathrm{sf}} = \frac{6(1-\varepsilon)}{d_{\mathrm{p}}} \tag{B.16}$$

h_{sf} is the interstitial heat transfer coefficient and is given by Eq. B.17.

$$\frac{1}{h_{\mathrm{sf}}} = \frac{d_{\mathrm{p}}}{k_{\mathrm{f}} Nu} + \frac{d_{\mathrm{p}}}{\beta k_{\mathrm{s}}} \tag{B.17}$$

Here β equals 10 for the assumed spherical shape of the particles. To determine the influence of convective to conductive heat transfer between the fluid and solid phase, Nu is the Nusselt Number with the assumed correlation of Eq. B.18.

$$Nu = 2.0 + 1.1 Pr^{1/3} Re_{\mathrm{p}}^{0.6} \tag{B.18}$$

Pr is the Prandtl Number of air (Eq. B.19).

$$Pr = \frac{\mu_{\mathrm{f}} C_{\mathrm{p,f}}}{k_{\mathrm{f}}} \tag{B.19}$$

Re_{p} is the particle Reynold's Number restated from the main text and given by Eq. B.20.

$$Re_{\mathrm{p}} = \frac{d_{\mathrm{p}} \rho_{\mathrm{f}} |\vec{u}_{\mathrm{p}}|}{\mu_{\mathrm{f}}} \tag{B.20}$$

The velocities listed in the main text are Darcy/fluid velocities ($\vec{u} = \vec{u}_{\mathrm{d}}$). We adjust the pore/interstitial velocity, $\vec{u}_{\mathrm{p}}$, by dividing by porosity by Eq. B.21.

$$\vec{u}_{\mathrm{p}} = \frac{\vec{u}_{\mathrm{d}}}{\varepsilon} \tag{B.21}$$

.

Based on these equations, we find that the expected $\Delta T \sim 0.02$ K < 0.1 K $\ll 1$ K. Thus our assumption of local thermal equilibrium for the model is valid.

B.3 Materials-scale gravimmetric measurements

At the small, materials-scale, gravimmetric measurements are performed to fit kinetic parameters, and additionally extract equilibrium vapor pressure at room temperature. To achieve this, weigh boats are filled with 1 ± 0.02 g of dehydrated $SrBr_2$ composite particles that are spread thin to within $\sim 2-3$mm to minimize diffusive-transport limitations. The weigh boats are placed in an enclosed plastic container. The humidistat (Section 4.2.4)

flowed nearly 4 LPM of humid air, which should be high enough to minimize convective mass transport limitations. Experiments are performed with both 30% or 45% RH air flowing into this container. During hydration the sample is periodically removed from the chamber and measured on a scale (Ohaus SPX223 ± 1 mg) to track mass change over time (Fig. B.1). Each measurement took 30 seconds, which may slightly impact the results although the salts were only out of container for about 1% of the total reaction time. Once the hydration is complete, the samples are dehydrated at 0% RH, and this cycle is repeated three times for each humidity. Based on the expected mass increase from stoichiometry, and adjusting for the measured water uptake capacity of pure vermiculite, which is 10 wt% that of the $SrBr_2$ composite (Fig. B.5), we assume the 50wt%-50wt% composite can uptake a maximum of 55 wt% of water compared to pure $SrBr_2$. This is used to calculate the fractional extent of hydration, α, with the measured mass of water uptake. By numerically solving to minimize the least square error between measured hydration fraction and the kinetic rate equation (Eq. 4.2) across the 30% and 45% RH data, we find $C_0 exp\left(-\frac{E_a}{RT}\right) = 3.2 \times 10^{-4}$ 1/s and $p_{eq} = 255$ Pa at room temperature ($R^2 > 0.999$), which are used as inputs in Eq. 4.2 and Eq. 4.4 respectively for the model.

B.4 Neutron computed tomography and porosity determination

We conducted neutron imaging tomography (NCT) of the dehydrated $SrBr_2$ composite to determine the porosity for the multi-physics model and to visualize the internal structure of the salt. Experiments were performed at the Multimodal Advanced Radiography Station (MARS), beamline CG-1D, at the High Flux Isotope Reactor at Oak Ridge National Laboratory. Moderated neutrons with wavelengths ranging from 0.8 to ~ 6 Å (with a peak around 2.6 Å) are collimated using a pinhole aperture and a collimation system for neutron imaging measurements. The field-of-view was 8.6 cm x 8.6 cm with effective pixel size of 42 μm. A 100 μm 6LiF/ZnS scintillator was used to convert transmitted neutrons into light signal and recorded as a 2D image. A 15 mm diameter air-tight Al tube (0.5 mm thick walls) was filled with the dehydrated $SrBr_2$ composite and placed on a rotating stage in front of the imaging setup. To create the 3D NCT scan, the tube was rotated from 0° to 360° with a step size of 0.61 degrees. At each step, a still 2D image was taken with an exposure time of 30 seconds. Although the scan took multiple hours, since the vial was sealed the salt should have had minimal hydration. Amira was used to reconstruct the 3D image by stitching together the 2D images [203]. To determine the porosity, first a rectangular prism

volume approximately (9.7 mm x 9.7 mm x 23.1 mm/ 220 x 220 x 550 pixels) was cropped to exclude the edges of the container to determine bulk porosity. Then, the seeded watershed segmentation algorithm was used to determine the porosity of the sample [204]. Based on 2D slices of the image, discrete in-focus vermiculite particles and regions of porosity each served as seeds based on an initial threshold screening. The watershed tool grew these seeds up to the edges of the particles. The threshold cut-off was tuned and verified from several 2D slices to ensure an accurate estimate of solid volume fraction. The bulk porosity was calculated to be $51.8 \pm 5\%$. This is rounded, and a 50% porosity is used when comparing model to experiment. Since imaging pixel size is 42 μm, it was difficult to visualize individual folds of the expanded vermiculite composite. Watershed segmentation was repeated 3 times with slightly different initial thresholds with $\pm$ 5% representing an estimate of the observed bounds of porosity uncertainty.

Fig. B.2a,b,c show the network consists of an interconnected porous network. The vermiculite particles are a few mms in diameter and exhibit a ribbon shape (Fig. B.2d). Larger pore channels can be on the millimeter scale. Overall, the NCT scans show the promise of this technique to visualize the structure of the porous media. A higher resolution technique, such as X-ray tomography would need to be deployed to resolve finer features [205], such as individual vermiculite ribbons although neutron imaging was sufficient to determine a porosity.

B.5 Instantaneous water uptake measurements

The instantaneous water uptake (Fig. B.6) of both the composite and the vermiculite only experiments were calculated based on the relative humidity values at the inlet and the outlet at any given instant. Next, the mass of the reactor was measured before and after each experiment to determine the total mass of water uptake. Reaction extent (Fig. B.6c) is then calculated by taking the ratio of instantaneous mass of water uptake (m_{H2O}) to that of the total mass of water uptake. In some cases the reaction extent goes beyond 1, which may be due to the fact that the in our experiments we assume $SrBr_2 \cdot 1H_2O$ gets converted to $SrBr_2 \cdot 6H_2O$. However, some of the composite might be in its pure anhydrous form ($SrBr_2$) prior to the start of the reaction.

B.6 Uncertainty analysis

Uncertainty propagation analysis was used to calculate the overall uncertainty in the value of measured parameters. For a general case of an experimental result, r, computed from J mea-

sured variables, $X_{1,...,J}$, the data reduction equation can be written as: $r = r(X_1, X_2, ..., X_J)$. The uncertainty in the experimental result is given by Eq. B.22

$$U_r^2 = \left(\frac{\partial r}{\partial X_1}\right)^2 U_{X_1}^2 + \left(\frac{\partial r}{\partial X_2}\right)^2 U_{X_2}^2 + \cdots + \left(\frac{\partial r}{\partial X_J}\right)^2 U_{X_J}^2 \tag{B.22}$$

For example, the uncertainty in specific energy, $(E) = mC_p(T_{in} - T_{out})dt$, is given by Eq. B.23

$$\frac{U_E}{E} = \sqrt{\left(\frac{U_m}{m}\right)^2 + \left(\frac{U(T_{in})}{T_{in}}\right)^2 + \left(\frac{U(T_{out})}{T_{out}}\right)^2} \tag{B.23}$$

The same process is followed for other parameters with the maximum uncertainty values listed in Table B.2.

Table B.2: Maximum uncertainty for $SrBr_2$ composite experimental reactor parameters

Parameter	**Maximum Uncertainty**
Mass	10 mg
Flow rate	0.1 LPM
Temperature	0.5°C
Specific energy	6 Wh/kg
Specific power	0.38 W/kg

B.7 Heat-loss estimation

To estimate the maximum possible loss in the reactor we conducted experiments in a reactor filled with fully dehydrated $SrBr_2$ composite, and with dry air at 2 LPM, 4 LPM, and 6 LPM. To mimic the the reaction conditions we supplied dry air at the inlet, $T_{in,da} = 35$°C, which is the peak temperature that was measured in the experiments with humid air for any of the flow rates tested, and measured the outlet temperature of the dry air (Fig. B.8). The reason for this drop in temperature occurs because of heat losses in the reactor, which is used to obtain an overall heat loss coefficient consistent with the reactor surface area, by assuming that the wall temperature, $T_{w,da} = 0.5(T_{in,da} + T_{out,da})$, is the average of the inlet and the outlet dry air temperatures, $T_{in,da}$ and $T_{out,da}$ respectively. The net rate of heat lost by the air is in Eq. B.24, from which, we can obtain a loss coefficient, U_l, as in Eq. B.25.

$$\dot{Q}_{loss,da} = \dot{m}c_p(T_{in,da} - T_{out,\,da}) \tag{B.24}$$

The heat lost by the air can be assumed to be the heat lost to the ambient through the reactor walls:

$$U_{\mathrm{l}} = \frac{\dot{Q}_{loss,da}}{A_s(T_{\mathrm{w,da}} - T_{\mathrm{amb}})}) \tag{B.25}$$

In Eq. B.25, $T_{\mathrm{amb}} = 22°\mathrm{C}$ is the ambient temperature and A_s is the surface area over heat losses occur to the ambient from the region of the reactor where the packed-bed will be present. Therefore, $A_s = 2LW + 2LH$, where $L,\ W,\ H = 14$ cm, 5 cm, and 5 cm respectively (Fig. B.7). By assuming that this loss coefficient calculated will be nearly the same during the actual hydration measurements with the $SrBr_2$ composite, the rate of heat loss can be estimated as in Eq. B.26

$$\dot{Q}_{\mathrm{loss,ac}} = U_{\mathrm{l}} A_s (T_{\mathrm{w,ac}} - T_{\mathrm{amb}}) \tag{B.26}$$

where $T_{\mathrm{w,ac}}$ is the time- and space-averaged reactor wall temperature obtained as an average of the time-averaged inlet and outlet air temperature measured for every flow rate tested.

Table B.3 shows the rate of heat loss obtained per unit mass of total material in the reactor for every flow rate tested and also computes what fraction this constitutes of the maximum specific power that is discharged to the air.

Table B.3: Heat loss estimates at different flow rates from heated $T_{\mathrm{in,da}} = 35°\mathrm{C}$ inlet $SrBr_2$ composite experiments

Flow rate (LPM)	$\dot{Q}_{\mathrm{loss,ac}}$ (W)	$\dot{q}_{\mathrm{loss,ac}}$ (W/kg)	Percentage of Specific power (%)
2	0.114	1.14	57.25
4	0.142	1.42	17.81
6	0.256	2.56	23.31

APPENDIX C

Appendix for Chapter 5: Spatial Distributions of Hydration Cycling in Salt Hydrates using Neutron Imaging

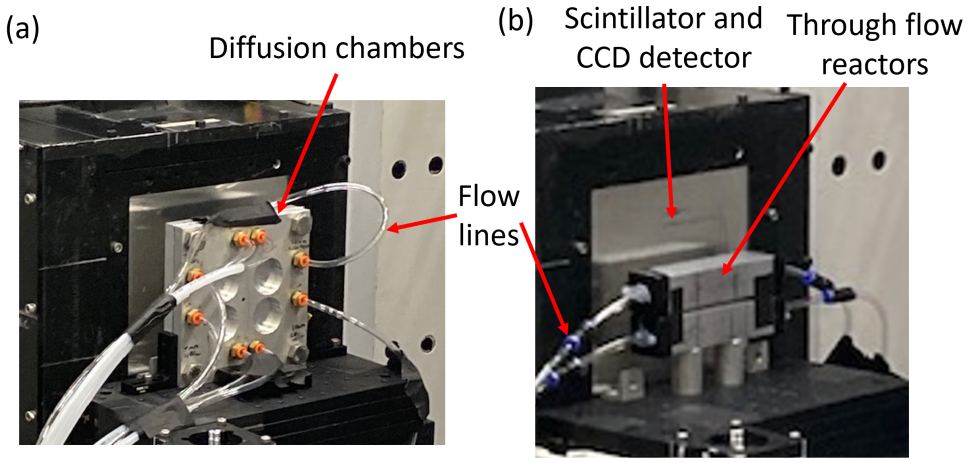


Figure C.1: Images of experimental setup of salt hydrate imaging at Multimodal Advanced Radiography Station (MARS) — CG-1D — HFIR. (a) Diffusion chambers and (b) Through flow reactors.

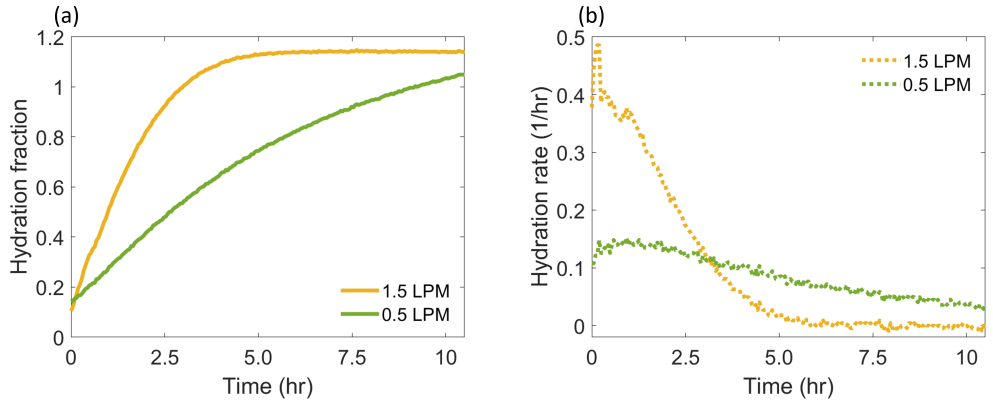


Figure C.2: Through flow $SrBr_2$ composite reactor results. (a) Hydration Fraction vs time and (b) Reaction rate versus time.

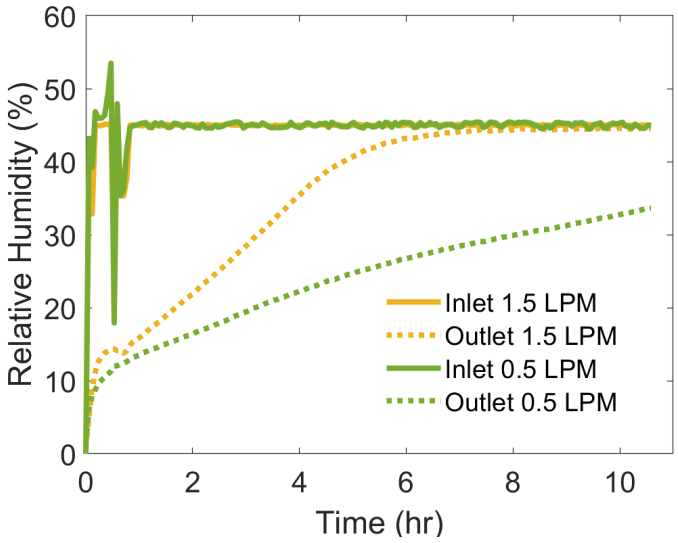


Figure C.3: Relative humidity versus time for both top (1.5 LPM) and bottom (0.5 LPM) through flow reactors.

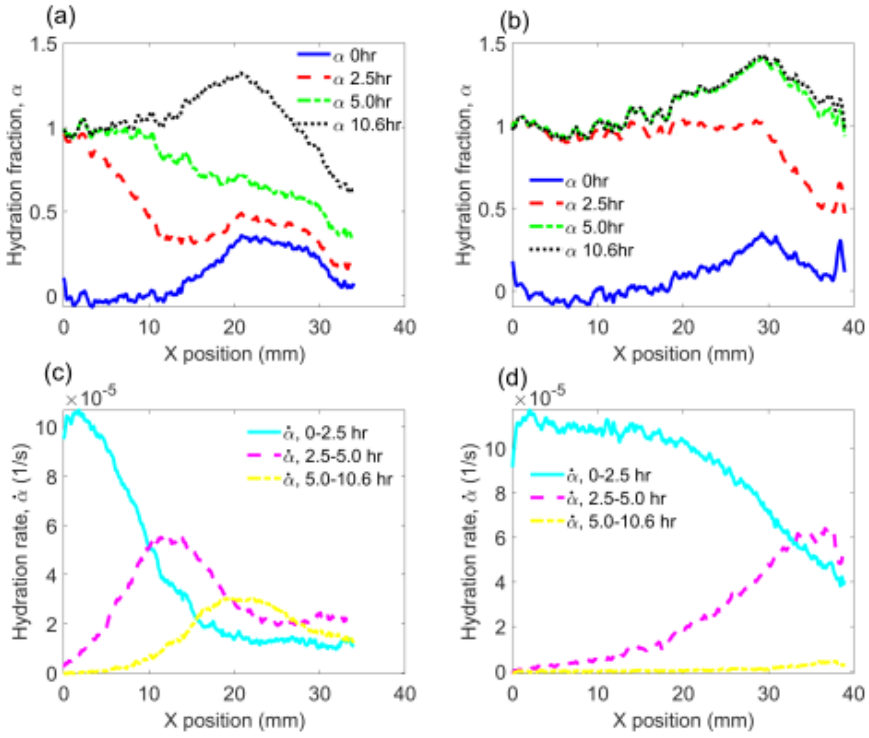


Figure C.4: Spatial distribution of hydration fraction and rate for reactors. (a) and (c) for 0.5 LPM and (b) and (d) for 1.5 LPM.

C.1 Experimental Methods

C.1.1 Sample Preparation

$SrBr_2{\cdot}6H_2O$ (99%, Thermo Scientific Chemicals, Pittsburgh, PA) and expanded vermiculite (2-3 mm, Millipore-Sigma, Burlington, MA) are used for the composite materials. The wet impregnation method is used to synthesize the 50wt%-50wt% $SrBr_2$-vermiculite composite where a salt solution is initially mixed with vermiculite [95, 79]. This mixture is dried out in a muffle furnace at 120°C for 8 hours with a ±5°C/min ramp rate with mass measurements used to confirm complete dehydration. Both the pure and composite salts were dehydrated at 0% RH in a homemade environmental chamber and transported in air tight vials to Oak Ridge National Laboratory to avoid rehydration. The expected (de)hydration reaction for the experiment is $SrBr_2{\cdot}1H_2O + 5H_2O(v) \longleftrightarrow SrBr_2{\cdot}6H_2O$ although the vermiculite is expected to contribute $< 5\%$ to the total hydration [99].

C.1.2 Neutron Imaging Set-up

Fig. 5.1a,c shows the reactor setup for the diffusion chamber experiments. To control air flow rate and relative humidity entering the salt chambers, an Arduino controlled PID humidistat consisting of a wet (dreschel bubbler) and dry line with proportional solenoid valves (Enfield, PFV-W12E05-P050C-0200) is used with full details explained in prior work [195, 186]. To ensure a quick ($<$ 3 minute and stable response) baseline PID values of $K_\mathrm{p} = 0.6, K_\mathrm{i} = 0.75\mathrm{s}^{-1}, K_\mathrm{d} = 0.0005\mathrm{s}$ are used in conjunction with the humidity sensor (Adafruit, SHT45, ±1% RH) with a sampling rate of every 2 seconds. The upstream pressure is adjusted to ensure a steady flow rate (Sensiron, SFM4300-20-P, ±2%) reaches each salt hydrate line. Since $SrBr_2$ and K_2CO_3 are hydrated at different humidity two separate humidistat lines are used to control salt specific humidity (not shown in the simplified Fig. 5.1c). Since flow lines are controlled electronically flow and humidity values can be updated without having to interrupt imaging. All outlet lines are run to a 2 micron particle filter to avoid releasing any trace amounts of irradiated salt in the air flow.

To maximize transparency of the reactor, diffusion channels were machined into a 6.35 mm (1/4") thick Al plate, which based on the MARS iNEUT tool ([108]) should be about 85% transparent (actual Al transparency in the filled chambers is higher due to milling). The smaller chambers are 6 mm tall by 5 mm wide, with these dimensions roughly representing a typical TGA pan [79]. Next to the TGA chambers are larger 20 mm deep by 15 mm wide chambers, to allow effects of a deeper diffusion depth to be investigated. The composite chamber channels are 10.2 mm thick and the pure salt chambers are 7.0 mm thick, which are

selected for optimal transmission imaging based on salt composition, stoichiometric water uptake and related transmission contrast, and estimated density from the MARS iNEUT tool ([108]). Each chamber is filled with salt, and then a thin ($\sim$ 1 mm) Al plate is placed over each chamber and Al taped to avoid diffusion flowing over air gaps in each chamber. A 0.8 mm thick teflon gasket, water jet cut to fit around the diffusion chambers, is placed on the back-plate. The 6.35 mm thick Al top-plate is screwed on top to create an air tight seal. The thickness of the top-plate is reduced in front of the diffusion chambers to maximize transmission.

For the through flow reactor setup, 12.7 mm x 12.7 mm Al square tubes (0.35 mm thick walls) are filled with $SrBr_2$ composite salt (Fig. 5.1b). Teflon meshes and 3D printed PLA mesh holders are used to hold salt the salt in place during imaging. Due to slight differences in packing, the top chamber has an active salt hydrate length of 44 mm and the bottom has 37.5 mm active length. Each reactor is controlled with a separate humidistat line.

C.1.3 Experimental Procedure

For the diffusion chamber experiments, since it took roughly an hour to begin experiments between loading the salts and connecting the flow setup, an initial dehydration step to avoid any inadvertent hydration is run until neutron images stop changing and the outlet humidity reads <1%. Both $SrBr_2$ lines are hydrated at 45% RH, which is chosen to be close to but below the deliquescence relative humidity to maximize reaction rate while avoiding the salts forming a solution [83]. To induce dehydration the humidity is set to 0% RH. Half-cycle lengths are determined by ensuring the smaller (6 mm) composite chamber fully reacts. This allows one full hydration-dehydration cycle plus a second hydration to be observed. Air flow direction is from the small to large chambers with the 1 LPM hydration flow rate selected to avoid less than 2% drop in humidity to ensure steady humidity at the top of each salt chamber (Fig. 5.1a). Humidity values are measured both before and after the reactor chambers to ensure this assumption remains valid. Flow rates vary between 1-2 LPM during dehydration to speed up this step since the hydration step is of more interest to study.

For the through flow reactors, the $SrBr_2$ composite partially hydrated during loading, so dehydration was run until the measured outlet humidity was less than 3% for both chambers. However, as will be shown in the results, the downstream half of the reactors still may have been partially hydrated at the start of the experiment. Both reactors are run for a single hydration half-cycle at 45% RH. Based on observations from our prior work, the top reactor was hydrated at a flow rate of 1.5 LPM, three times higher than the bottom reactor's flow rate of 0.5 LPM in order to show the transition between mass transport to kinetics limited

regime [195, 91].

C.1.4 Hydration Fraction Normalization

To convert raw neutron imaging light intensities into estimated hydration fractions to understand how the reactions progress, we calibrate using known dehydrated and hydrated portions of the salts for each setup. We assume a linear dependence of transmission on hydration state between these bounds [107]. For the diffusion chambers, there is high confidence the smaller TGA chambers is fully dehydrated and fully hydrated at the beginning and end of the first hydration respectively, so these transmission values are used to calibrate the diffusion chambers. For the through flow reactors, since there is less confidence the down stream (right half in Fig. 5.1b) is fully dehydrated at the start of the hydration cycle, the transmission intensity is averaged in the left half of the reactor. The dehydrated/hydrated transmissions are normalized to the 1.5 LPM reactor since outlet humidity values indicate this flow rate is fully reacted by the end of the experiment. Some hydration fraction measurements go above 1 and below 0. This is because calibrations measured in one portion of the salt are used to determine hydration fractions in other regions where packing fraction/particle density could be different.

C.1.5 Image Analysis

To conduct analysis from raw images, the normalization Jupyter notebook at analysis.ornl.gov adjusts the raw images against the dark field and open beam images to correct for any artefacts from fluctuations in raw beam intensity [206]. To measure hydration fractions, the normalized image stack are imported into ImageJ Fiji [207]. By setting the calibration scale to the known dehydrated and hydrated states and binning pixels into 2x2 squares to reduce noise, ImageJ is able to determine and visualize average hydration states for each frame for the selected regions of interest. To determine diffusion depth for the chamber experiments, image thresholding is used where a drop-off in transmission intensity indicates the threshold of the moving hydration front. Due to the slight non-uniformity in hydration profiles, there is some manual value judgement for determining the exact location of the diffusion front.

BIBLIOGRAPHY

[1] Haynes 214 datasheet. https://www.haynesintl.com/en/datasheet/haynes-214-alloy/#tensile-properties. Accessed: 2024-03-22.

[2] C. S. Smith. Grains, phases, and interphases: an interpretation of microstructure. *Trans. Metall. Soc. AIME*, 175:15–51, 1948.

[3] D. J. Srolovitz, M. P. Anderson, G. S. Grest, and P. S. Sahni. Computer simulation of grain growth-iii. influence of a particle dispersion. *Acta Metallurgica*, 32:1429–1438, 1984.

[4] M. Gaeini, S. A. Shaik, and C. C.M. Rindt. Characterization of potassium carbonate salt hydrate for thermochemical energy storage in buildings. *Energy and Buildings*, 196:178–193, 8 2019.

[5] Jason Woods, Allison Mahvi, Anurag Goyal, Eric Kozubal, Adewale Odukomaiya, and Roderick Jackson. Rate capability and ragone plots for phase change thermal energy storage. *Nature Energy*, 6:295–302, 2021.

[6] Dongdong Gu, Hongmei Zhang, Donghua Dai, Mujian Xia, Chen Hong, and Reinhart Poprawe. Laser additive manufacturing of nano-tic reinforced ni-based nanocomposites with tailored microstructure and performance. *Composites Part B: Engineering*, 163:585–597, 4 2019.

[7] Min Yang, Lu Wang, and Wentao Yan. Phase-field modeling of grain evolutions in additive manufacturing from nucleation, growth, to coarsening. *npj Computational Materials*, 2021.

[8] Frank P. Incropera and David P. DeWitt. *Fundamentals of heat and mass transfer*. Wiley, 1996.

[9] A. A. Hawwash, Hamdy Hassan, and Khalid El feky. Impact of reactor design on the thermal energy storage of thermochemical materials. *Applied Thermal Engineering*, 168:114776, 3 2020.

[10] International Energy Agency. Net zero by 2050 - a roadmap for the global energy sector, 2021.

[11] Diana Ürge Vorsatz, Luisa F. Cabeza, Susana Serrano, Camila Barreneche, and Ksenia Petrichenko. Heating and cooling energy trends and drivers in buildings. *Renewable and Sustainable Energy Reviews*, 41:85–98, 2015.

[12] International Energy Agency. Renewables 2022, 2022.

[13] Mark Mehos, Craig Turchi, Judith Vidal, Michael Wagner, Zhiwen Ma, Clifford Ho, William Kolb, Charles Andraka, and Alan Kruizenga. Concentrating solar power gen3 demonstration roadmap, 2017.

[14] Aditya Sundar, Aaron Feinauer, Bryan Kinzer, Joerg Petrasch, Liang Qi, and Rohini Bala Chandran. Thermodynamic, kinetic and mechanical modeling to evaluate co2-induced corrosion via oxidation and carburization in fe, ni alloys. *Corrosion Science*, 229:111850, 5 2024.

[15] Bandar AlMangour, Min Seok Baek, Dariusz Grzesiak, and Kee Ahn Lee. Strengthening of stainless steel by titanium carbide addition and grain refinement during selective laser melting. *Materials Science and Engineering A*, 712:812–818, 1 2018.

[16] R. L. Klueh, J. P. Shingledecker, R. W. Swindeman, and D. T. Hoelzer. Oxide dispersion-strengthened steels: A comparison of some commercial and experimental alloys. *Journal of Nuclear Materials*, 341:103–114, 5 2005.

[17] Adewale Odukomaiya, Jason Woods, Nelson James, Sumanjeet Kaur, Kyle R Gluesenkamp, Navin Kumar, Sven Mumme, Roderick Jackson, and Ravi Prasher. Addressing energy storage needs at lower cost via on-site thermal energy storage in buildings. *Energy Environ. Sci*, 14:5315, 2021.

[18] Asegun Henry, Ravi Prasher, and Arun Majumdar. Five thermal energy grand challenges for decarbonization. *Nature Energy*, 5:635–637, 9 2020.

[19] Jiuxin Ning, Xiaodong Wang, Yajing Sun, Chenggang Zheng, Shengwu Zhang, Xi Zhao, Changyong Liu, and Wentao Yan. Experimental and numerical investigation of additively manufactured novel compact plate-fin heat exchanger. *International Journal of Heat and Mass Transfer*, 190, 7 2022.

[20] Ana Vafadar, Ferdinando Guzzomi, Alexander Rassau, and Kevin Hayward. Advances in metal additive manufacturing: A review of common processes, industrial applications, and current challenges. *Applied Sciences (Switzerland)*, 11:1–33, 2 2021.

[21] Joel C. Vasco. *Additive manufacturing for the automotive industry*, pages 505–530. Elsevier, 1 2021.

[22] W. H. Yu, S. L. Sing, C. K. Chua, C. N. Kuo, and X. L. Tian. Particle-reinforced metal matrix nanocomposites fabricated by selective laser melting: A state of the art review. *Progress in Materials Science*, 104:330–379, 7 2019.

[23] Eyob Messele Sefene. State-of-the-art of selective laser melting process: A comprehensive review. *Journal of Manufacturing Systems*, 63:250–274, 4 2022.

[24] B. W. Baker, T. R. McNelley, and L. N. Brewer. Grain size and particle dispersion effects on the tensile behavior of friction stir welded ma956 oxide dispersion strengthened steel from low to elevated temperatures. *Materials Science and Engineering A*, 589:217–227, 1 2014.

[25] Bandar AlMangour, Young Kyun Kim, Dariusz Grzesiak, and Kee Ahn Lee. Novel tib2-reinforced 316l stainless steel nanocomposites with excellent room- and high-temperature yield strength developed by additive manufacturing. *Composites Part B: Engineering*, 156:51–63, 1 2019.

[26] Jeoung Han Kim, Thak Sang Byun, David T. Hoelzer, Seong Woong Kim, and Bong Ho Lee. Temperature dependence of strengthening mechanisms in the nanostructured ferritic alloy 14ywt: Part i-mechanical and microstructural observations. *Materials Science and Engineering A*, 559:101–110, 1 2013.

[27] Bryan Kinzer and Rohini Bala Chandran. A phase-field study on the effects of nucleation rate and nanoparticle distributions on solidification and grain growth. *JOM*, 11 2023.

[28] Timothy M. Smith, Christopher A. Kantzos, Nikolai A. Zarkevich, Bryan J. Harder, Milan Heczko, Paul R. Gradl, Aaron C. Thompson, Michael J. Mills, Timothy P. Gabb, and John W. Lawson. A 3d printable alloy designed for extreme environments. *Nature 2023 617:7961*, 617:513–518, 4 2023.

[29] Kanthal a1 datasheet. https://www.kanthal.com/en/products/material-datasheets/wire/resistance-heating-wire-and-resistance-wire/kanthal-a-1/. Accessed: 2024-02-20.

[30] Kanthal apm datasheet. https://www.kanthal.com/en/products/material-datasheets/tube/kanthal-apm/. Accessed: 2024-02-20.

[31] R. Cueff, H. Buscail, E. Caudron, C. Issartel, and F. Riffard. Oxidation behaviour of kanthal apm and kanthal af at 1173 k: Effect of yttrium alloying addition. *Surface Engineering*, 19:58–64, 2003.

[32] G. B. Schaffer, M. H. Loretto, R. E. Smallman, and J. W. Brooks. The stability of the oxide dispersion in inconel alloy ma6000. *Acta Metallurgica*, 37:2551–2558, 9 1989.

[33] Ting Chiang Lin, Chezheng Cao, Maximilian Sokoluk, Lin Jiang, Xin Wang, Julie M. Schoenung, Enrique J. Lavernia, and Xiaochun Li. Aluminum with dispersed nanoparticles by laser additive manufacturing. *Nature Communications*, 10, 12 2019.

[34] Min Yang, Lu Wang, and Wentao Yan. Phase-field modeling of grain evolution in additive manufacturing with addition of reinforcing particles. *Additive Manufacturing*, 47:102286, 11 2021.

[35] Qiyang Tan, Jingqi Zhang, Ning Mo, Zhiqi Fan, Yu Yin, Michael Bermingham, Yingang Liu, Han Huang, and Ming Xing Zhang. A novel method to 3d-print fine-grained

alsi10mg alloy with isotropic properties via inoculation with lab6 nanoparticles. *Additive Manufacturing*, 32, 3 2020.

[36] Bibek Poudel, Hoa X. Nguyen, Aaron O'Neil, Mohsan Uddin Ahmad, Zhiyuan Qu, Patrick Kwon, and Haseung Chung. Selective laser melting and mechanical properties of oxide dispersion strengthened haynes 214 alloy. *Proceedings of the ASME 2022 17th International Manufacturing Science and Engineering Conference*, 9 2022.

[37] Dongdong Gu, Hongqiao Wang, Fei Chang, Donghua Dai, Pengpeng Yuan, Yves Christian Hagedorn, and Wilhelm Meiners. Selective laser melting additive manufacturing of tic/alsi10mg bulk-form nanocomposites with tailored microstructures and properties. *Physics Procedia*, 56:108–116, 1 2014.

[38] Yangyiwei Yang, Carlos Doñate-Buendía, Timileyin David Oyedeji, Bilal Gökce, and Bai Xiang Xu. Nanoparticle tracing during laser powder bed fusion of oxide dispersion strengthened steels. *Materials*, 14, 7 2021.

[39] John Campbell. Casting alloys. *Complete Casting Handbook*, pages 223–340, 1 2015.

[40] Xi Wang and Xinpu Shen. Research progress of ods fecral alloys–a review of composition design. *Materials*, 16, 9 2023.

[41] Sneha N. Naik and Stephen M. Walley. The hall–petch and inverse hall–petch relations and the hardness of nanocrystalline metals. *Journal of Materials Science*, 55:2661–2681, 3 2020.

[42] P A Manohar, M Ferry, and T Chandra. Five decades of the zener equation. *ISIJ International*, 38:913–924, 1998.

[43] Stephen Dewitt, Shiva Rudraraju, David Montiel, W Beck Andrews, and Katsuyo Thornton. Prisms-pf: A general framework for phase-field modeling with a matrix-free finite element method. *npj Computational Materials*, 6, 2020.

[44] N. Moelans, B. Blanpain, and P. Wollants. Quantitative analysis of grain boundary properties in a generalized phase field model for grain growth in anisotropic systems. *Physical Review B - Condensed Matter and Materials Physics*, 78, 7 2008.

[45] Fengbo Han, Bin Tang, Hongchao Kou, Jinshan Li, and Yong Feng. Cellular automata simulations of grain growth in the presence of second-phase particles. *Modelling and Simulation in Materials Science and Engineering*, 23:065010, 9 2015.

[46] Xuxiao Li and Wenda Tan. Numerical investigation of effects of nucleation mechanisms on grain structure in metal additive manufacturing. *Computational Materials Science*, 153:159–169, 10 2018.

[47] Christian Schwarze, Reza Darvishi Kamachali, and Ingo Steinbach. Phase-field study of zener drag and pinning of cylindrical particles in polycrystalline materials. *Acta Materialia*, 106:59–65, 2016.

[48] N. Moelans, B. Blanpain, and P. Wollants. A phase field model for the simulation of grain growth in materials containing finely dispersed incoherent second-phase particles. *Acta Materialia*, 53:1771–1781, 4 2005.

[49] Yoshihiro Suwa, Yoshiyuki Saito, and Hidehiro Onodera. Phase field simulation of grain growth in three dimensional system containing finely dispersed second-phase particles. *Scripta Materialia*, 55:407–410, 2006.

[50] Tamas Pusztai, Laszlo Ratkai, Attila Szallas, and Laszlo Granasy. Phase-field modeling of solidification in light-metal matrix nanocomposites. *Magnesium Technology*, pages 455–459, 2014.

[51] M. Jegatheesan and Anirban Bhattacharya. A 2d model for prediction of nanoparticle distribution and microstructure evolution during solidification of metal matrix nanocomposites. *Modelling and Simulation in Materials Science and Engineering*, 29, 9 2021.

[52] Takahisa Kinoshita and Munekazu Ohno. Phase-field simulation of abnormal grain growth during carburization in nb-added steel. *Computational Materials Science*, 177:109558, 5 2020.

[53] Jinge Liu and Peng Wen. Metal vaporization and its influence during laser powder bed fusion process. *Materials & Design*, 215:110505, 3 2022.

[54] Jerard V. Gordon, Sneha P. Narra, Ross W. Cunningham, He Liu, Hangman Chen, Robert M. Suter, Jack L. Beuth, and Anthony D. Rollett. Defect structure process maps for laser powder bed fusion additive manufacturing. *Additive Manufacturing*, 36, 12 2020.

[55] Ross Cunningham, Cang Zhao, Niranjan Parab, Christopher Kantzos, Joseph Pauza, Kamel Fezzaa, Tao Sun, and Anthony D Rollett. Keyhole threshold and morphology in laser melting revealed by ultrahigh-speed x-ray imaging. *Science*, 363:849–852, 2019.

[56] Minglei Qu, Qilin Guo, Luis I. Escano, Samuel J. Clark, Kamel Fezzaa, and Lianyi Chen. Mitigating keyhole pore formation by nanoparticles during laser powder bed fusion additive manufacturing. *Additive Manufacturing Letters*, 3:100068, 12 2022.

[57] Brian J. Simonds, Jack Tanner, Alexandra Artusio-Glimpse, Paul A. Williams, Niranjan Parab, Cang Zhao, and Tao Sun. The causal relationship between melt pool geometry and energy absorption measured in real time during laser-based manufacturing. *Applied Materials Today*, 23, 6 2021.

[58] David R. Poirier and Gordon H. Geiger. *Transport phenomena in materials processing*. Springer International Publishing, 1 2016.

[59] Minglei Qu, Qilin Guo, Luis I. Escano, Jiandong Yuan, S. Mohammad H. Hojjatzadeh, Samuel J. Clark, Kamel Fezzaa, Tao Sun, and Lianyi Chen. Controlling melt flow by nanoparticles to eliminate surface wave induced surface fluctuation. *Additive Manufacturing*, page 103081, 8 2022.

[60] Minglei Qu, Qilin Guo, Luis Izet Escano, Ali Nabaa, Kamel Fezzaa, and Lianyi Chen. Nanoparticle-enabled increase of energy efficiency during laser metal additive manufacturing. *Additive Manufacturing*, page 103242, 10 2022.

[61] Santosh Chavan, Ramesh Rudrapati, and Selvaraj Manickam. A comprehensive review on current advances of thermal energy storage and its applications. *Alexandria Engineering Journal*, 61:5455–5463, 7 2022.

[62] Caleb Amy, Hamid Reza Seyf, Myles A. Steiner, Daniel J. Friedman, and Asegun Henry. Thermal energy grid storage using multi-junction photovoltaics. *Energy and Environmental Science*, 12:334–343, 1 2019.

[63] Rondo heat battery. https://rondo.com/how-it-works. Accessed: 2024-02-23.

[64] Hamza Ayaz, Veerakumar Chinnasamy, Junhyeok Yong, and Honghyun Cho. Review of technologies and recent advances in low-temperature sorption thermal storage systems. *Energies*, 14, 10 2021.

[65] Ahmed Hassan, Mohammad Shakeel Laghari, and Yasir Rashid. Micro-encapsulated phase change materials: A review of encapsulation, safety and thermal characteristics. *Sustainability (Switzerland)*, 8, 10 2016.

[66] P. A.J. Donkers, L. C. Sögütoglu, H. P. Huinink, H. R. Fischer, and O. C.G. Adan. A review of salt hydrates for seasonal heat storage in domestic applications. *Applied Energy*, 199:45–68, 8 2017.

[67] Steven Kiyabu, Patrick Girard, and Donald J. Siegel. Discovery of salt hydrates for thermal energy storage. *Journal of the American Chemical Society*, 19:54, 11 2022.

[68] Wei Li, Jiří Jaromír Klemeš, Qiuwang Wang, and Min Zeng. Salt hydrate–based gas-solid thermochemical energy storage: Current progress, challenges, and perspectives. *Renewable and Sustainable Energy Reviews*, 154, 2 2022.

[69] Ruby-Jean Clark, Gohar Gholamibozanjani, Jason Woods, Sumanjeet Kaur, Adewale Odukomaiya, Said Al-Hallaj, and Mohammed Farid. Experimental screening of salt hydrates for thermochemical energy storage for building heating application. *Journal of Energy Storage*, 51:104415, 7 2022.

[70] Steven Kiyabu, Jeffrey S. Lowe, Alauddin Ahmed, and Donald J. Siegel. Computational screening of hydration reactions for thermal energy storage: New materials and design rules. *Chemistry of Materials*, 30:2006–2017, 3 2018.

[71] Yinan Qiu, Yan Yang, Na Yang, Lige Tong, Shaowu Yin, Li Wang, and Yulong Ding. Thermochemical energy storage using silica gel: Thermal storage performance and nonisothermal kinetic analysis. *Solar Energy Materials and Solar Cells*, 251:112153, 3 2023.

[72] Y. C. Lin, Y. B. Fan, S. Chen, X. J. Zhang, A. Frazzica, and L. Jiang. Wave analysis method for air humidity assisted sorption thermal battery: A new perspective. *Energy Conversion and Management*, 277:116638, 2 2023.

[73] Kyriaki G. Sakellariou, George Karagiannakis, Yolanda A. Criado, and Athanasios G. Konstandopoulos. Calcium oxide based materials for thermochemical heat storage in concentrated solar power plants. *Solar Energy*, 122:215–230, 12 2015.

[74] Rohini Bala Chandran and Jane H. Davidson. Model of transport and chemical kinetics in a solar thermochemical reactor to split carbon dioxide. *Chemical Engineering Science*, 146:302–315, 6 2016.

[75] Marie Duquesne, Jean Toutain, Alain Sempey, Stéphane Ginestet, and Elena Palomo Del Barrio. Modeling of a nonlinear thermochemical energy storage by adsorption on zeolites. *Applied Thermal Engineering*, 71:469–480, 10 2014.

[76] Natalia Mazur, Melian A.R. Blijlevens, Rick Ruliaman, Hartmut Fischer, Pim Donkers, Hugo Meekes, Elias Vlieg, Olaf Adan, and Henk Huinink. Revisiting salt hydrate selection for domestic heat storage applications. *Renewable Energy*, page 119331, 12 2023.

[77] Armand Fopah-Lele and Jean Gaston Tamba. A review on the use of srbr2·6h2o as a potential material for low temperature energy storage systems and building applications. *Solar Energy Materials and Solar Cells*, 164:175–187, 5 2017.

[78] An T. Pham, Bryan Kinzer, Ritvik Jain, Rohini Bala Chandran, and Michael T. Craig. Assessing the Value of Coupling Thermal Energy Storage with Heat Pumps for Residential Space Heating in U.S. Cities. Working paper, University of Michigan, 2024.

[79] Robin Fisher, Yulong Ding, and Adriano Sciacovelli. Hydration kinetics of k2co3, mgcl2 and vermiculite-based composites in view of low-temperature thermochemical energy storage. *Journal of Energy Storage*, 38, 6 2021.

[80] Luca Scapino, Herbert A. Zondag, Johan Van Bael, Jan Diriken, and Camilo C.M. Rindt. Sorption heat storage for long-term low-temperature applications: A review on the advancements at material and prototype scale. *Applied Energy*, 190:920–948, 2017.

[81] Kokouvi Edem N'Tsoukpoe and Frédéric Kuznik. A reality check on long-term thermochemical heat storage for household applications. *Renewable and Sustainable Energy Reviews*, 139, 4 2021.

[82] Alexandr Shkatulov, Rick Joosten, Hartmut Fischer, and Henk Huinink. Core-shell encapsulation of salt hydrates into mesoporous silica shells for thermochemical energy storage. *ACS Applied Energy Materials*, 3:6860–6869, 7 2020.

[83] Benoit Michel, Nathalie Mazet, and Pierre Neveu. Experimental investigation of an innovative thermochemical process operating with a hydrate salt and moist air for

thermal storage of solar energy: Global performance. *Applied Energy*, 129:177–186, 9 2014.

[84] Paul Albertus, Joseph S. Manser, and Scott Litzelman. Long-duration electricity storage applications, economics, and technologies. *Joule*, 4:21–32, 1 2020.

[85] De-foa-0002787: Buildings energy efficiency frontiers and innovation technologies (benefit), 2023.

[86] Moira L. Nicolson, Michael J. Fell, and Gesche M. Huebner. Consumer demand for time of use electricity tariffs: A systematized review of the empirical evidence. *Renewable and Sustainable Energy Reviews*, 97:276–289, 12 2018.

[87] Benoit Michel, Nathalie Mazet, and Pierre Neveu. Experimental investigation of an open thermochemical process operating with a hydrate salt for thermal storage of solar energy: Local reactive bed evolution. *Applied Energy*, 180:234–244, 10 2016.

[88] V. M. Van Essen, H. A. Zondag, J. Cot Gores, L. P.J. Bleijendaal, M. Bakker, R. Schuitema, W. G.J. Van Helden, Z. He, and C. C.M. Rindt. Characterization of mgso4 hydrate for thermochemical seasonal heat storage. *Journal of Solar Energy Engineering, Transactions of the ASME*, 131:0410141–0410147, 11 2009.

[89] H A Zondag, V M Van Essen, L P J Bleijendaal, B W J Kikkert, and M Bakker. Application of mgcl2 6h 2 o for thermochemical seasonal solar heat storage. *5th International Renewable Energy Storage Conference*, 2010.

[90] A Rubino, R De Boer, Antonio Rubino, and Robert De Boer. Seasonal storage of solar heat reactor modeling. *10th IIR Gustav Lorentzen Conference on Natural Refigerants*, 2012.

[91] Tim Raemaekers, Pim Donkers, and Henk Huinink. Investigation into the hydration behavior of k2co3 packed beds: An nmr study. *Transport in Porous Media 2023*, pages 1–19, 7 2023.

[92] Joey Aarts, Stan de Jong, Martina Cotti, Pim Donkers, Hartmut Fischer, Olaf Adan, and Henk Huinink. Diffusion limited hydration kinetics of millimeter sized salt hydrate particles for thermochemical heat storage. *Journal of Energy Storage*, 47, 3 2022.

[93] H. Scott Fogler. *Elements of Chemical Reaction Engineering*. Pearson Education, Limited, 2020.

[94] D V Ragone. Review of battery systems for electrically powered vehicles. Technical report, Society of Automotive Engineers, 5 1968.

[95] A. Cammarata, V. Verda, A. Sciacovelli, and Y. Ding. Hybrid strontium bromide-natural graphite composites for low to medium temperature thermochemical energy storage: Formulation, fabrication and performance investigation. *Energy Conversion and Management*, 166:233–240, 6 2018.

[96] Bo Ding, Chao Xu, Zhirong Liao, and Feng Ye. Study on long-term thermochemical thermal storage performance based on srbr2-expanded vermiculite composite materials. *Journal of Energy Storage*, 42:103081, 10 2021.

[97] Vincenza Brancato, Larisa G. Gordeeva, Alessio Sapienza, Valeria Palomba, Salvatore Vasta, Alexandra D. Grekova, Andrea Frazzica, and Yuri I. Aristov. Experimental characterization of the licl/vermiculite composite for sorption heat storage applications. *International Journal of Refrigeration*, 105:92–100, 9 2019.

[98] P. A.J. Donkers, L. Pel, and O. C.G. Adan. Experimental studies for the cyclability of salt hydrates for thermochemical heat storage. *Journal of Energy Storage*, 5:25–32, 6 2016.

[99] R. J. Sutton, E. Jewell, J. Elvins, J. R. Searle, and P. Jones. Characterising the discharge cycle of cacl2 and lino3 hydrated salts within a vermiculite composite scaffold for thermochemical storage. *Energy and Buildings*, 162:109–120, 3 2018.

[100] M. A.J.M. Beving, A. J.H. Frijns, C. C.M. Rindt, and D. M.J. Smeulders. Effect of cycle-induced crack formation on the hydration behaviour of k2co3 particles: Experiments and modelling. *Thermochimica Acta*, 692:178752, 10 2020.

[101] Ting Yan and Hong Zhang. A critical review of salt hydrates as thermochemical sorption heat storage materials: Thermophysical properties and reaction kinetics. *Solar Energy*, 242:157–183, 8 2022.

[102] Pim A.J. Donkers, Leo Pel, and Olaf C.G. Adan. Dehydration/hydration of granular beds for thermal storage applications: A combined nmr and temperature study. *International Journal of Heat and Mass Transfer*, 105:826–830, 2 2017.

[103] M. Gaeini, R. Wind, P. A.J. Donkers, H. A. Zondag, and C. C.M. Rindt. Development of a validated 2d model for flow, moisture and heat transport in a packed bed reactor using mri experiment and a lab-scale reactor setup. *International Journal of Heat and Mass Transfer*, 113:1116–1129, 10 2017.

[104] Yannan Zhang, Haohui Dong, Ruzhu Wang, and Penghui Feng. Air humidity assisted sorption thermal battery governed by reaction wave model. *Energy Storage Materials*, 27:9–16, 5 2020.

[105] Ziyang Nie, Patrick McCormack, Hassina Z. Bilheux, Jean C. Bilheux, J. Pierce Robinson, Jagjit Nanda, and Gary M. Koenig. Probing lithiation and delithiation of thick sintered lithium-ion battery electrodes with neutron imaging. *Journal of Power Sources*, 419:127–136, 4 2019.

[106] Perizat Berdiyeva, Anastasiia Karabanova, Malgorzata G. Makowska, Rune E. Johnsen, Didier Blanchard, Bjørn C. Hauback, and Stefano Deledda. In-situ neutron imaging study of nh3 absorption and desorption in srcl2 within a heat storage prototype reactor. *Journal of Energy Storage*, 29, 6 2020.

[107] Perizat Berdiyeva, Anastasiia Karabanova, Didier Blanchard, Bjørn C. Hauback, and Stefano Deledda. Sr(nh3)8cl2-expanded natural graphite composite for thermochemical heat storage applications studied by in-situ neutron imaging. *Journal of Energy Storage*, 34, 2 2021.

[108] Yuxuan Zhang, Jean C. Bilheux, Hassina Z. Bilheux, and Jiao Y.Y. Lin. An interactive web-based tool to guide the preparation of neutron imaging experiments at oak ridge national laboratory. *Journal of Physics Communications*, 3, 10 2019.

[109] zener-pinning-prisms-pf. https://github.com/BryanKinzer/zener-pinning-PRISMS-PF. Accessed: 2024-02-20.

[110] Naoko Oono, Q. X. Tang, and Shigeharu Ukai. Oxide particle refinement in ni-based ods alloy. *Materials Science and Engineering A*, 649:250–253, 1 2016.

[111] Qingxin Tang, Takeshi Hoshino, Shigeharu Ukai, Bin Leng, Shigenari Hayashi, and Yongming Wang. Refinement of oxide particles by addition of hf in ni-0.5 mass *Materials Transactions*, 51:2019–2024, 2010.

[112] D. T. Hoelzer, J. Bentley, M. A. Sokolov, M. K. Miller, G. R. Odette, and M. J. Alinger. Influence of particle dispersions on the high-temperature strength of ferritic alloys. *Journal of Nuclear Materials*, 367-370 A:166–172, 2007.

[113] Carmen M. Cepeda-Jiménez and María T. Pérez-Prado. Processing of nanoparticulate metal matrix composites. *Comprehensive Composite Materials II*, pages 313–330, 1 2017.

[114] Jeoung Han Kim, Thak Sang Byun, David T. Hoelzer, Chan Hee Park, Jong Taek Yeom, and Jae Keun Hong. Temperature dependence of strengthening mechanisms in the nanostructured ferritic alloy 14ywt: Part ii-mechanistic models and predictions. *Materials Science and Engineering A*, 559:111–118, 1 2013.

[115] J. P. Kruth, L. Froyen, J. Van Vaerenbergh, P. Mercelis, M. Rombouts, and B. Lauwers. Selective laser melting of iron-based powder. *Journal of Materials Processing Technology*, 149:616–622, 6 2004.

[116] Martin Balog, Peter Krizik, Oto Bajana, Tao Hu, Hanry Yang, Julie M. Schoenung, and Enrique J. Lavernia. Influence of grain boundaries with dispersed nanoscale al2o3 particles on the strength of al for a wide range of homologous temperatures. *Journal of Alloys and Compounds*, 772:472–481, 1 2019.

[117] J Q Xu, L Y Chen, H Choi, and X C Li. Theoretical study and pathways for nanoparticle capture during solidification of metal melt. *J. Phys.: Condens. Matter*, 24:255304–255314, 2012.

[118] M. F. Ashby and R. M. A. Centamore. The dragging of small oxide particles by migrating grain boundaries in copper. *Acta Metallurgica*, 16:1081–1092, 1968.

[119] Azmir Harun, Elizabeth A. Holm, Mike P. Clode, and Mark A. Miodownik. On computer simulation methods to model zener pinning. *Acta Materialia*, 54:3261–3273, 7 2006.

[120] Jakob Grasserbauer, Irmgard Weißensteiner, Georg Falkinger, Peter J. Uggowitzer, and Stefan Pogatscher. Influence of fe and mn on the microstructure formation in 5xxx alloys—part ii: Evolution of grain size and texture. *Materials*, 14, 6 2021.

[121] M. P. Anderson, G. S. Grest, R. D. Doherty, Kang Li, and D. J. Srolovitz. Inhibition of grain growth by second phase particles: Three dimensional monte carlo computer simulations. *Scripta Metallurgica*, 23:753–758, 1989.

[122] Liesbeth Vanherpe, Nele Moelans, Bart Blanpain, and Stefan Vandewalle. Pinning effect of spheroid second-phase particles on grain growth studied by three-dimensional phase-field simulations. *Computational Materials Science*, 49:340–350, 8 2010.

[123] D. J. Srolovitz, G. S. Grest, M. P. Anderson, and A. D. Rollett. Computer simulation of recrystallization—ii. heterogeneous nucleation and growth. *Acta Metallurgica*, 36:2115–2128, 8 1988.

[124] I Sinha and R K Mandal. Avrami exponent under transient and heterogeneous nucleation transformation conditions. *Journal of Non-Crystalline Solids*, 357:919–925, 2011.

[125] Eloi Pineda, Trinität Pradell, and Daniel Crespo. Non-random nucleation and the avrami kinetics. *Philosophical Magazine A: Physics of Condensed Matter, Structure, Defects and Mechanical Properties*, 82:107–121, 2002.

[126] S. P. Gentry and K. Thornton. Simulating recrystallization in titanium using the phase field method. *IOP Conference Series: Materials Science and Engineering*, 89, 8 2015.

[127] Mario Castro. Phase-field approach to heterogeneous nucleation. *Physical Review B*, 3:67, 2002.

[128] Tams Pusztai, Gyorgy Tegze, Gyula I. Toth, Lszlo Kornyei, Gurvinder Bansel, Zhungyun Fan, and Lszlo Grnsy. Phase-field approach to polycrystalline solidification including heterogeneous and homogeneous nucleation. *Journal of Physics Condensed Matter*, 20, 10 2008.

[129] Y. Idell, L. E. Levine, A. J. Allen, F. Zhang, C. E. Campbell, G. B. Olson, J. Gong, D. R. Snyder, and H. Z. Deutchman. Unexpected δ-phase formation in additive-manufactured ni-based superalloy. *JOM*, 68:950–959, 3 2016.

[130] E. E. Underwood. Stereology, or the quantitative evaluation of microstructures. *Journal of Microscopy*, 89:161–180, 4 1969.

[131] Nele Moelans, Bart Blanpain, and Patrick Wollants. An introduction to phase-field modeling of microstructure evolution. *Calphad: Computer Coupling of Phase Diagrams and Thermochemistry*, 32:268–294, 6 2008.

[132] Sina Shahandeh and Matthias Militzer. Grain boundary curvature and grain growth kinetics with particle pinning. *Philosophical Magazine*, 93:3231–3247, 8 2013.

[133] David A. Porter, Kenneth E. Easterling, and Mohamed Y. Sherif. Phase transformations in metals and alloys, third edition. *Phase Transformations in Metals and Alloys, Third Edition*, pages 1–521, 1 2009.

[134] D Turnbull. Formation of crystal nuclei in liquidmetals. *Journal of Applied Physics*, 21:1022–1028, 1950.

[135] Joy Banerjee, Seong H. Kim, and Carlo G. Pantano. Elemental areal density calculation and oxygen speciation for flat glass surfaces using x-ray photoelectron spectroscopy. *Journal of Non-Crystalline Solids*, 450:185–193, 10 2016.

[136] Luisa Ickes, André Welti, Corinna Hoose, and Ulrike Lohmanna. Classical nucleation theory of homogeneous freezing of water: thermodynamic and kinetic parameters. *Physical Chemistry Chemical Physics*, 17:5514–5537, 2 2015.

[137] J. P. Simmons, C. Shen, and Y. Wang. Phase field modeling of simultaneous nucleation and growth by explicitly incorporating nucleation events. *Scripta Materialia*, 43:935–942, 10 2000.

[138] W. Wu, D. Montiel, J. E. Guyer, P. W. Voorhees, J. A. Warren, D. Wheeler, L. Granasy, T. Pusztai, and O. G. Heinonen. Phase field benchmark problems for nucleation. *Computational Materials Science*, 193:110371, 6 2021.

[139] Jie Ding, D Neffati, Q Li, R Su, Jin Li, S Xue, Z Shang, Y Zhang, H Wang, Y Kulkarni, and X Zhang. Thick grain boundary induced strengthening in nanocrystalline ni alloy. *Nanoscale*, 11:23449–23458, 2019.

[140] Markus Apel, Bernd Böttger, Jenny Rudnizki, Philippe Schaffnit, and Ingo Steinbach. Grain growth simulations including particle pinning using the multiphase-field concept. *ISIJ International*, 49:1024–1029, 7 2009.

[141] R D Doherty, K Li, K Kashyup, A D Rollett, and M P Anderson. Computer modelling of particle limited grain growth and its experimental verification. *Los Alamos Meeting*, 1989.

[142] Kai Song and Mark Aindow. Grain growth and particle pinning in a model ni-based superalloy. *Materials Science and Engineering: A*, 479:365–372, 4 2008.

[143] M. Soucail, R. Messina, A. Cosnuau, and L. P. Kubin. Monte carlo simulation of zener pinning in two dimensions. *Materials Science and Engineering A*, 271:1–7, 11 1999.

[144] N. Moelans, B. Blanpain, and P. Wollants. Pinning effect of second-phase particles on grain growth in polycrystalline films studied by 3-d phase field simulations. *Acta Materialia*, 55:2173–2182, 4 2007.

[145] Anubhav Jain, Shyue Ping Ong, Geoffroy Hautier, Wei Chen, William Davidson Richards, Stephen Dacek, Shreyas Cholia, Dan Gunter, David Skinner, Gerbrand Ceder, and Kristin A. Persson. Commentary: The materials project: A materials genome approach to accelerating materials innovation. *APL Materials*, 1:011002, 7 2013.

[146] R. D. Doherty, D. J. Srolovitz, A. D. Rollett, and M. P. Anderson. On the volume fraction dependence of particle limited grain growth. *Scripta Metallurgica*, 21:675–679, 5 1987.

[147] G. Couturier, R. Doherty, C. Maurice, and R. Fortunier. 3d finite element simulation of the inhibition of normal grain growth by particles. *Acta Materialia*, 53:977–989, 2 2005.

[148] Henning Aufgebauer, Julia Kundin, Heike Emmerich, Maral Azizi, Christian Reimann, Jochen Friedrich, Thomas Jauß, Tina Sorgenfrei, and Arne Cröll. Phase-field simulations of particle capture during the directional solidification of silicon. *Journal of Crystal Growth*, 446:12–26, 7 2016.

[149] K. Ozgur Gunduz, Alberto Visibile, Mohammad Sattari, Irina Fedorova, Saud Saleem, Krystyna Stiller, Mats Halvarsson, and Jan Froitzheim. The effect of additive manufacturing on the initial high temperature oxidation properties of re-containing fecral alloys. *Corrosion Science*, 188:109553, 8 2021.

[150] Cang Zhao, Kamel Fezzaa, Ross W. Cunningham, Haidan Wen, Francesco De Carlo, Lianyi Chen, Anthony D. Rollett, and Tao Sun. Real-time monitoring of laser powder bed fusion process using high-speed x-ray imaging and diffraction. *Scientific Reports*, 7, 12 2017.

[151] B A Pint, A J Garratt-Reed, and L W Hobbs. The reactive element effect in commercial ods fecrai alloys. *Materials at High Temperatures*, 13:3–16, 1995.

[152] Amir Mostafaei, Cang Zhao, Yining He, Seyed Reza Ghiaasiaan, Bo Shi, Shuai Shao, Nima Shamsaei, Ziheng Wu, Nadia Kouraytem, Tao Sun, Joseph Pauza, Jerard V. Gordon, Bryan Webler, Niranjan D. Parab, Mohammadreza Asherloo, Qilin Guo, Lianyi Chen, and Anthony D. Rollett. Defects and anomalies in powder bed fusion metal additive manufacturing. *Current Opinion in Solid State and Materials Science*, 26, 4 2022.

[153] J-O Andersson, Thomas Helander, Lars Hoglund, Pingfang Shi, and Bo Sundman. Thermo-calc and dictra, computational tools for materials science. *Calphad*, 26:273–312, 2002.

[154] Ilan Gur, Karma Sawyer, and Ravi Prasher. Searching for a better thermal battery. *Science*, 335:1454–1455, 3 2012.

[155] Andrew Martin, Drew Lilley, Ravi Prasher, and Sumanjeet Kaur. Particle size optimization of thermochemical salt hydrates for high energy density thermal storage. *Energy and Environmental Materials*, 2023.

[156] Hui Yang, Chengcheng Wang, Lige Tong, Shaowu Yin, Li Wang, and Yulong Ding. Salt hydrate adsorption material-based thermochemical energy storage for space heating application: A review. *Energies*, 16, 3 2023.

[157] Taisen Yan, Tingxian Li, Jiaxing Xu, Jingwei Chao, Ruzhu Wang, Yuri I. Aristov, Larisa G. Gordeeva, Pradip Dutta, and S. Srinivasa Murthy. Ultrahigh-energy-density sorption thermal battery enabled by graphene aerogel-based composite sorbents for thermal energy harvesting from air. *ACS Energy Letters*, 6:1795–1802, 5 2021.

[158] EIA. 2020 RECS. Technical report, EIA, 2020.

[159] Matthias Schmidt and Marc Linder. A novel thermochemical long term storage concept: Balance of renewable electricity and heat demand in buildings. *Frontiers in Energy Research*, 8, 7 2020.

[160] Kirsten Linnow, Michael Niermann, Dennis Bonatz, Konrad Posern, and Michael Steiger. Experimental studies of the mechanism and kinetics of hydration reactions. *Energy Procedia*, 48:394–404, 2014.

[161] Simon Randau, Dominik A. Weber, Olaf Kötz, Raimund Koerver, Philipp Braun, André Weber, Ellen Ivers-Tiffée, Torben Adermann, Jörn Kulisch, Wolfgang G. Zeier, Felix H. Richter, and Jürgen Janek. Benchmarking the performance of all-solid-state lithium batteries. *Nature Energy*, 5:259–270, 3 2020.

[162] Thomas Christen. Ragone plots and discharge efficiency-power relations of electric and thermal energy storage devices. *Journal of Energy Storage*, 27, 2 2020.

[163] Weikai Zhao, Guocai Yu, Shuang Li, Zhengxian Liu, and Linzhi Wu. Rate capability and ragone plots for thermal management multifunctional structure designing. *International Journal of Mechanical Sciences*, 252, 8 2023.

[164] Nelson James, Allison Mahvi, and Jason Woods. Optimizing phase change composite thermal energy storage using the thermal ragone framework. *Journal of Energy Storage*, 56, 12 2022.

[165] Kazuaki Yazawa, Patrick J. Shamberger, and Timothy S. Fisher. Ragone relations for thermal energy storage technologies. *Frontiers in Mechanical Engineering*, 5, 2019.

[166] Michael Shanks, Charles M. Shoalmire, Michael Deckard, Karan N. Gohil, Henry Lewis, Darin Lin, Patrick J. Shamberger, and Neera Jain. Design of spatial variability in thermal energy storage modules for enhanced power density. *Applied Energy*, 314, 5 2022.

[167] Erik J Barbosa, George W Woodruff, and Akanksha K Menon. Salt hydrate thermochemical energy storage in buildings: Analyzing storage density and thermal power output. *ASME 2023 17th International Conference on Energy Sustainability*, 2023.

[168] Joey Aarts, Hartmut Fischer, Olaf Adan, and Henk Huinink. Impact of cycling on the performance of mm-sized salt hydrate particles. *Journal of Energy Storage*, 76:109806, 1 2024.

[169] Henk Huinink, Stan de Jong, and Vera Houben. Hydration fronts in packed particle beds of salt hydrates: Implications for heat storage. *Journal of Energy Storage*, 71:108158, 11 2023.

[170] M. Lebrun and B. Spinner. Models of heat and mass transfers in solid—gas reactors used as chemical heat pumps. *Chemical Engineering Science*, 45:1743–1753, 1 1990.

[171] K. Kant, A. Shukla, David M.J. Smeulders, and C. C.M. Rindt. Performance analysis of a k2co3-based thermochemical energy storage system using a honeycomb structured heat exchanger. *Journal of Energy Storage*, 38, 6 2021.

[172] Alexandre Malley-Ernewein and Sylvie Lorente. Analysis of thermochemical energy storage in an elemental configuration. *Scientific Reports 2019 9:1*, 9:1–9, 11 2019.

[173] M. Gaeini, H. A. Zondag, and C. C.M. Rindt. Effect of kinetics on the thermal performance of a sorption heat storage reactor. *Applied Thermal Engineering*, 102:520–531, 6 2016.

[174] Hongzhi Liu, Wantong Wang, and Yaning Zhang. Performance gap between thermochemical energy storage systems based on salt hydrates and materials. *Journal of Cleaner Production*, 313, 9 2021.

[175] Benoit Michel, Nathalie Mazet, Sylvain Mauran, Driss Stitou, and Jing Xu. Thermochemical process for seasonal storage of solar energy: Characterization and modeling of a high density reactive bed. *Energy*, 47:553–563, 11 2012.

[176] Stan de Jong. Modelling salt hydration in packed beds for thermochemical heat storage purposes. Technical report, Eindhoven University of Technology, 2022.

[177] F. Koksal, O. Gencel, W. Brostow, and H. E. Hagg Lobland. Effect of high temperature on mechanical and physical properties of lightweight cement based refractory including expanded vermiculite. *Materials Research Innovations*, 16:7–13, 2012.

[178] Comsol. Comsol multiphysics v. 5.6 www.comsol.com. comsol ab, stockholm, sweden., 2023.

[179] A. Gubkov, N. Fermor, and N. Smirnov. Vapor pressure of mono-poly systems. Technical report, Zh. Prikl. Khim., 1964.

[180] Leyla-Cann Sogutoglu, Michael Steiger, Jelle Houben, Daan Biemans, Hartmut R Fischer, Pim Donkers, Henk Huinink, and Olaf C G Adan. Understanding the hydration process of salts: The impact of a nucleation barrier. *Crystal Growth & Design*, 19:2279–2288, 2019.

[181] Massoud Kaviany. *Principles of Heat Transfer in Porous Media*. Springer, 2 edition, 9 1995.

[182] Daniel J. Keene, Jane H. Davidson, and Wojciech Lipiński. A model of transient heat and mass transfer in a heterogeneous medium of ceria undergoing nonstoichiometric reduction. *Journal of Heat Transfer*, 135, 5 2013.

[183] Zhendong Ye, Hongzhi Liu, Wantong Wang, Han Liu, Jing Lv, and Fan Yang. Reaction/sorption kinetics of salt hydrates for thermal energy storage. *Journal of Energy Storage*, 56, 12 2022.

[184] N. Mazet, M. Amouroux, and B. Spinner. Analysis and experimental study of the transformation of a non-isothermal solid/gas reacting medium. *Chemical Engineering Communications*, 99:155–174, 1991.

[185] Yunus Cengel and Michael Boles. *Thermodynamics: An Engineering Approach*. McGraw Hill, 2023.

[186] Lars B. Veldscholte, Rens J. Horst, and Sissi de Beer. Design, construction, and testing of an accurate low-cost humidistat for laboratory-scale applications. *The European Physical Journal E 2021 44:4*, 44:1–8, 4 2021.

[187] Zhaoli Zhang, Jiayu Liu, Nan Zhang, Xiaoling Cao, Yanping Yuan, Muhammad Sultan, and Shady Attia. Dynamic discharging performance of a latent heat thermal energy storage system based on a pid controller. *Journal of Energy Storage*, 71, 11 2023.

[188] Jana Stengler, Julius Weiss, and Marc Linder. Analysis of a lab-scale heat transformation demonstrator based on a gas–solid reaction. *Energies*, 12, 6 2019.

[189] Thomas Reddy. *Linden's Handbook of Batteries, Fourth Edition*. McGraw-Hill Education, 2011.

[190] Drew Lilley, Jonathan Lau, Chris Dames, Sumanjeet Kaur, and Ravi Prasher. Impact of size and thermal gradient on supercooling of phase change materials for thermal energy storage. *Applied Energy*, 290, 5 2021.

[191] Ankush Shankar Pujari, Rudrodip Majumdar, and Sandip K. Saha. Thermochemical energy storage using radial flow annular reactor for attaining lower pressure drop. *Proceedings of the 8th World Congress on Momentum, Heat and Mass Transfer*, 3 2023.

[192] Joey Aarts, Natalia Mazur, Hartmut R. Fischer, Olaf C.G. Adan, and Henk P. Huinink. Elucidating the dehydration pathways of k2co3·1.5h2o. *Crystal Growth and Design*, 3 2023.

[193] Ziwei Chen, Yanan Zhang, Yong Zhang, Yuehong Su, and Saffa Riffat. A study on vermiculite-based salt mixture composite materials for low-grade thermochemical adsorption heat storage. *Energy*, 278, 9 2023.

[194] Leyla-Cann So, Michael Steiger, Jelle Houben, Daan Biemans, Hartmut R Fischer, Pim Donkers, Henk Huinink, and Olaf C G Adan. Understanding the hydration process of salts: The impact of a nucleation barrier. *Crystal Growth & Design*, 19:2279–2288, 2019.

[195] Bryan Kinzer, Durga Ghosh, Declan Crowley, Arijit Jatkar, and Rohini Bala Chandran. Modeling and Experimental Demonstrations Reveal Ragone Framework for Salt Hydrate Thermochemical Energy Storage. Working paper, University of Michigan, 2024.

[196] Cody J. Permann, Michael R. Tonks, Bradley Fromm, and Derek R. Gaston. Order parameter re-mapping algorithm for 3d phase field model of grain growth using fem. *Computational Materials Science*, 115:18–25, 4 2016.

[197] D. Fan and L. Q. Chen. Computer simulation of grain growth using a continuum field model. *Acta Materialia*, 45:611–622, 1997.

[198] Paul von Hippel. Skewness. *International Encyclopedia of Statistical Science*, pages 1340–1342, 2011.

[199] G S Beavers, E M Sparrow, and D E Rodenz. Influence of bed size on the flow characteristics and porosity of randomly packed beds of spheres. *Journal of Applied Mechanics*, 40:655–660, 1973.

[200] R Olives and S Mauran. A highly conductive porous medium for solid-gas reactions: Effect of the dispersed phase on the thermal tortuosity. *Transport in Porous Media*, 43:377–394, 2001.

[201] R J Millington and J P Quirk. Permeability of porous solids. *Trans. Faraday Soc.*, 57:1200–1207, 1961.

[202] Donald Nield and Adrian Bejan. *Convection in Porous Media*. Springer, 4 edition, 2013.

[203] Detlev Stalling, Malte Westerhoff, and Hans-Christian Hege. amira: A highly interactive system for visual data analysis. In *The Visualization Handbook*, 2005.

[204] Anton Kornilov, Ilia Safonov, and Ivan Yakimchuk. A review of watershed implementations for segmentation of volumetric images. *Journal of Imaging 2022, Vol. 8, Page 127*, 8:127, 4 2022.

[205] Paul Chao, George R. Lindemann, Allen H. Hunter, and Ashwin J. Shahani. Pseudo-4d view of the growth and form of locked eutectic colonies. *Acta Materialia*, 240, 11 2022.

[206] Jean C. Bilheux, Hassina Z. Bilheux, Yuxuan Zhang, Rich Crompton, Matthew J. Bedynek, Chen Zhang, Peter Parker, Garrett Granroth, Jiao Lin, Ian Lumsden, Simon Sebold, and Tobias Neuwirth. Neutron imaging software tools at the oak ridge national laboratory. *Journal of Physics: Conference Series*, 2605, 2023.

[207] Johannes Schindelin, Ignacio Arganda-Carreras, Erwin Frise, Verena Kaynig, Mark Longair, Tobias Pietzsch, Stephan Preibisch, Curtis Rueden, Stephan Saalfeld, Benjamin Schmid, Jean Yves Tinevez, Daniel James White, Volker Hartenstein, Kevin Eliceiri, Pavel Tomancak, and Albert Cardona. Fiji: An open-source platform for biological-image analysis. *Nature Methods*, 9:676–682, 7 2012.